

Mechanical Properties Characterization of 3D Printed Reservoir Sandstone Analogues

by

Juan Sebastian Gomez

A thesis submitted in partial fulfilment of the requirements for the degree of

Master of Science

in

GEOTECHNICAL ENGINEERING

Department of Civil and Environmental Engineering  
University of Alberta

© Juan Sebastian Gomez, 2017

## Abstract

This research work is focused on the characterization of the mechanical properties of 3D printed sandstone analogues produced using silica sand and binder jetting additive manufacturing technology. With control of grain size, grain size distribution, grain angularity, density distribution, discontinuity networks and type of cementing material, additive manufacturing technology offers a novel means to generate nearly equivalent specimens with controllable hydromechanical properties. The 3D printed rocks can serve as valuable proxies for test specimens in experimental studies of rock strength, deformation and failure modes while serving to minimize the influence of inter-sample variability and sample disturbance within the experiments.

Consequently, for the purpose of replicating the mechanical behavior of natural reservoir materials, uniaxial compression tests, Brazilian indirect tensions tests, direct tension tests and consolidated drained triaxial tests were conducted on 3D printed sandstone analogues. The specimens were built with a systematic variation of the main printing configurations: binder saturation, layer orientation and layer thickness. By these means, a comprehensive evaluation of the influence of the additive manufacturing process' printing features on the stress-strain behavior, peak strength, elastic properties, failure modes and strength parameters of this type of material was accomplished. Further comparison of these results with the properties of three representative sandstones found in nature and a descriptive statistical analysis (mean values, ranges, standard deviations and coefficient of variations) assisted in determining the suitability of the resultant range of properties and the repeatability and consistency of the results. This study demonstrated that 3D printing technology generates defensible and repeatable sandstone replicas with a deformation behavior analogous to the properties of natural reservoir rocks.

Nonetheless, additional work on alternative techniques to increase peak strength, Young's modulus and bulk compressibility must be performed to meet the range of values corresponding to natural reservoir rocks. For instance, a decrease of 64% on the average peak strength was found when comparing the results for the 3D printed sandstone analogues with the average values of Berea Sandstone. Furthermore, the bulk

compressibility of the sandstone proxies is around 6 to 7 times lower the compressibility of uniform natural reservoir rocks as Berea Sandstone.

*To Nathalia, my whole life and the main motive I had to start this journey.*

*To my parents and my sister for their sincere and supportive love.*

## **Acknowledgements**

There are not enough words to express my deep gratitude and respect for my research supervisor, Dr Rick Chalaturnyk. He has inspired and helped me throughout this journey and has thought me how to become an independent researcher. Today, with a bittersweet flavour in my heart I can say that I finally answered the question... So, what? Nonetheless, I will never forget to ask me the same thing in whatever the future has prepared for me in the upcoming years.

My sincere thanks must also go to Dr Gonzalo Zambrano, in first place for trusting, without your help it would have been more difficult to arrive at this wonderful group. Also, thank you for your advisory, because your door was never closed to any doubt or advice. You are a real *parcero*!

There is no way to express how much it meant to me to have been a member of GeoREF, the extensive experience of the staff, the innumerable advises and productive discussions and even the countless times I had to assemble and disassemble the triaxial cell were so meaningful to me and contributed to my learning process as an M.Sc. student.

Special thanks to Hope, our administrative assistant, for the photos, the travel advisory and many other recommendations, you are awesome. Also to the Department of Civil Engineering, specially to Dr. Nicholas Bier for his valuable contributions to the definitive version of this document.

Finally, I gratefully acknowledge the financial support of the Energi Simulation Industrial Research Consortia in Reservoir Geomechanics for Unconventional Resources.

## Table of Contents

Abstract.....	ii
Acknowledgements.....	v
Table of Contents.....	vi
Table of Tables .....	ix
Table of Figures .....	x
1. Introduction.....	1
1.1. Statement of the Problem.....	1
1.2. Objectives of the Research Project.....	3
1.2.1. General Objective .....	3
1.2.2. Methodology.....	3
1.3. Thesis outline .....	4
1.4. Scope .....	5
2. Additive Manufacturing Technology applied to Geomechanics .....	6
2.1. State of the Art: Additive Manufacturing Technology .....	6
2.2. 3D Printing Technology using Silica Sand and Furan Binder.....	10
2.2.1. ExOne 3D Printer System.....	10
2.2.2. Silica Sand .....	12
2.2.3. Furan Binder .....	13
2.2.4. Acidic Activator.....	14
2.3. High-Temperature Curing Process .....	15
2.4. General Printing Procedure.....	16
2.4.1. Step-by-step Printing Procedure .....	17
2.4.2. Specimens' Curing Process.....	19
2.5. Closing remarks on the application of AM technology in Geosciences .....	19

3. Description of Laboratory Testing Program.....	20
3.1. Introduction.....	20
3.2. Main 3D Printing Parameters.....	21
3.2.1. Binder Saturation .....	21
3.2.2. Layer Orientation .....	22
3.2.3. Layer Thickness .....	23
3.3. Matrix of Experimental Campaign .....	24
3.4. Descriptive Statistical Analysis of the UCS Specimens .....	26
3.5. Unconfined Compression Test Procedure .....	30
3.6. Brazilian Test Procedure.....	31
3.6. Direct Tension Tests Procedure.....	32
3.7. Consolidated Drained Triaxial Tests Procedure .....	34
3.7.1. Consolidated Drained Triaxial Testing Campaign .....	37
4. Results from Uniaxial Compression Testing Program .....	39
4.1. Introduction.....	39
4.2. Effect of Binder Saturation on the Mechanical Properties of the 3D printed sandstone analogues.....	39
4.3. Effect of Layer Orientation on the Mechanical Properties of the 3D printed sandstone analogues.....	43
4.4. Effect of Layer Thickness on the Mechanical Properties of the 3D printed sandstone analogues.....	48
4.5. Effect of High-Temperature Curing Process on the Mechanical Properties of the 3D printed sandstone analogues.....	51
4.6. Closing remarks about influence of Printing configurations on the mechanical properties of 3D printed sandstone analogues .....	51
5. Results from Tension Testing Program .....	53

5.1. Introduction.....	53
5.2. Brazilian Tension Test Results .....	54
5.3. Direct Tension Test Results .....	58
5.4. Relationship between Brazilian Tensile Strength and Direct Tensile Strength.....	62
6. Results from Consolidated Drained Triaxial Testing Program.....	64
6.1. Introduction.....	64
6.2. Compressibility and Volumetric Behavior Experiments .....	64
6.3. Effect of Confining Pressure on 3D Printed Sandstone’s Mechanical behavior ...	72
6.3.1. Peak Strength .....	73
6.3.2. Axial Strain at Failure and Post-Peak Behavior: .....	74
6.3.3. Strength Parameters and Mohr-Coulomb Failure Criterion.....	75
6.3.4. Volumetric Strain.....	76
6.3.5. Failure Mode of the Specimens .....	77
6.4. Hoek & Brown Failure Criterion for 3D Printed Sandstones .....	78
6.5. Parallel between the properties of 3D Printed Sandstones with natural reservoir sandstones .....	80
6.6. Future Research Work .....	81
7. Conclusions and Recommendations .....	82
7.1. Mechanical Properties Summary Table .....	82
7.2. Summary .....	83
7.3. Recommendations .....	85
References.....	87
Appendix A: Uniaxial Compression Tests Data.....	96

## Table of Tables

Table 2.1. Major Chemical composition of Furan Binder .....	14
Table 3.1. Matrix of Experimental Testing Campaign for Mechanical Characterization of 3D Printed Specimens.....	24
Table 3.2. 3D printed UCS analogues average dimensions.....	27
Table 3.3. Descriptive Statistical Analysis of the dimensional consistency of 3D Printed UCS specimens .....	28
Table 4.4. Summary of UCS Testing results for 3DP specimens built using various levels of Binder Saturations .....	40
Table 4.5. Summary of UCS testing results for 3DP specimens built using various layer orientations.....	44
Table 4.6. Summary of UCS Testing results for 3DP specimens built using various Layer Thicknesses.....	49
Table 5.1. Brazilian Test Results on 3D Printed Sandstone Analogues .....	57
Table 5.2. Summary of Direct Tension Test Results on 3D Printed Sandstone Analogues .....	59
Table 6.1. Bulk Compressibility Data for Different Natural Sandstones (After Fatt, 1958 and Zimmerman, 1992).....	69
Table 6.2. Summary of results from CD Triaxial Testing on 3DP Sandstone Analogues	73
Table 7.1. Summary Table of Mechanical Properties of 3DP Sandstone Analogues.....	82

## Table of Figures

Figure 2.1. 3D Printer System specifications (Modified from ExOne Manual, 2014).....	11
Figure 2.2. Particle Size Distribution of Silica Sand .....	13
Figure 2.3. Influence of Curing temperature on the peak UCS strength of the reservoir sandstone analogues (after Primkulov et al., 2017) .....	16
Figure 3.1. Representation of layer orientation of 3D printed specimens .....	23
Figure 3.2. UCS and Brazilian Test 3D Printed Specimens .....	25
Figure 3.3. 3D printed direct tension specimen with dimensional specifications .....	26
Figure 3.4. Shape deformation on specimens printed with inclined building planes. ....	29
Figure 3.5. Experimental Setup and Data Logging configuration for UCS Tests on 3DP Specimens .....	30
Figure 3.6. Experimental Setup and Data Logging configuration for Brazilian Tests on 3DP Specimens .....	32
Figure 3.7. Direct Tension Testing setup and Data Logging configuration for 3D Printed specimens.....	33
Figure 3.8. Consolidated drained triaxial test equipment .....	35
Figure 3.9. Configuration of the Internal LVDT's for the Triaxial Testing Campaign ....	36
Figure 3.10. Triaxial testing setup and data logging configuration for 3D printed specimens.....	37
Figure 4.1. Representative stress-strain relationship for the variation of binder saturation .....	41
Figure 4.2. Representative Stress-Strain Relationship for the variation of Layer Orientation .....	44
Figure 4.3. The consistency of the UC Strength results of the 3D Printed Sandstone Analogues. (b). Variation of the Tangent Young's Modulus with the Building Layer Orientation .....	46
Figure 4.4. Influence of Binder Spreading Direction on the Failure Mode of the 3DP specimens.....	48
Figure 4.5. Representative Stress-Strain Relationship for the variation of Layer Thicknesses.....	50

Figure 5.1. Tensile stress vs. diametric strain for 3DP sandstone analogues .....	55
Figure 5.2. Generalized Failure Mode for Brazilian Testing on 3D Printed specimens...	56
Figure 5.3. Crack initiation from circular pore boundary in tension and compression (after Cai et al. 2010).....	58
Figure 5.4. Axial tensile stress vs. axial strain for 3DP specimens printed at 0° layer orientation .....	60
Figure 5.5. Axial tensile stress vs. axial strain for 3DP specimens printed at 90° layer orientation .....	60
Figure 5.6. Failure mode of 90°-oriented analogues under Direct Tension.....	62
Figure 6.1. Relationship of volumetric strain to effective confining pressure for 3DP sandstone analogues.....	65
Figure 6.2. Bulk compressibility vs. effective confining stress' relationship for 3DP sandstone analogues.....	67
Figure 6.3. Bulk Compressibility curves from Natural Sandstones and 3DP Sandstone analogues.....	68
Figure 6.4. Bulk Modulus (K) vs. Effective Confining Stress relationship for 3DP Sandstone Analogues .....	70
Figure 6.5. Deviator Stress vs. Axial Strain Relationship for 3DP Analogues .....	72
Figure 6.6. Deviator Stress vs. Strain Relationship for 3D Printed Specimens under different confining pressures.....	73
Figure 6.7. Mohr Circles for the drained triaxial tests conducted on 3DP analogues .....	76
Figure 6.8. Volumetric behavior of 3D printed analogues under triaxial conditions .....	77
Figure 6.9. Failure Modes of 3D Printed Specimens under Triaxial Conditions .....	78
Figure 6.10. Hoek & Brown Failure Criterion for 3D Printed Reservoir Sandstones .....	79
Figure 6.11. Comparison between the properties of 3D Printed analogues and Berea Sandstone .....	80

# **1. Introduction**

## **1.1. Statement of the Problem**

The rapid development of the additive manufacturing (AM) industry, typically referred to as 3D printing, has resulted in the commercial availability of a wide range of 3D printer models (Tymrak et al. 2014, Lee et al. 2007 and Rankin et al. 2014). Moreover, the reduced costs of 3D printers, open-source software, and free access to digital model repositories are opening new avenues for many fields of research. Among these, geoscience is poised to use 3D printing (3DP) to bridge the gap between computational and experimental analyses (Ishutov et al. 2017).

Although initial attempts show potential for the use of 3DP in rock deformation experiments, limitations, particularly with respect to material properties are well recognized. The inherent properties of materials commonly used in 3DP (i.e. plastics, metal powders and gypsum powders) do not essentially resemble those of natural reservoir rocks or rock grains. For instance, some studies conducted in 3DP models reveal considerably low compressive strength compared to those encountered in natural rocks (Jiang & Zhao 2015).

Moreover, some printing parameters as delay times (Farzadi et al., 2015), printing layer orientation (Vlasea et al., 2015), binding material saturation and printing layer thickness (Vaezi & Chua, 2011), phase composition and macroporosity (Schumacher et al., 2010) and 3D printing materials “mixture” (Q. Jiang et al., 2016), control the results obtained on fundamental mechanical properties. Some of the most important properties involved include: Young’s modulus, Poisson’s ratio, cohesion and friction angle, specimens’ strength relative to the maximum loading direction; as well as flow properties as porosity structure. Consequently, there is an urgent need to understand the influence of each one of these features on the intrinsic properties of 3DP analogues.

Binder jetting additive manufacturing technology has enabled the use of silica sand as a 3DP material. This has allowed 3D rock analogues to be produced such that a significant reduction of specimen-to-specimen heterogeneity and conversely, exact control over the explicit inclusion of heterogeneities, such as fractures, within a specimen, have been achieved. By knowing and controlling inter-sample variability in terms of porosity, fracture networks, grain size distribution, and density distribution, 3D printing of geomaterials provides a valuable tool to validate numerical models, develop scaling laws and constitutive relationships, quantify the degree of influence of pore geometry, fracture network characteristics, and structural heterogeneity on macroscopic properties. Alternatively, 3D printing enables the systematic inclusion of specific features throughout a series of experiments under the same conditions. Such heterogeneities might include micro cracks, joint surface roughness proxies or variations in grain size. While rock deformation experiments have largely focused on developing insights into the mechanical behaviours of homogeneous materials in the subsurface, 3D printing provides a path to learn more about the impact of heterogeneities on bulk deformation behaviours and strain localization.

The reservoir geomechanics research group, [RG]<sup>2</sup> at the University of Alberta, has been pursuing fundamental work on the structure of 3DP reservoir “rocks” that involve investigating the pore structures that can be produced, constitutive properties of the bonding at the grain contacts and extensive geomechanical properties characterization studies. As a component of this comprehensive research initiative, the research in this thesis is mainly oriented to 1) determine the feasibility of the application of silica sand reservoir analogues to the study of fundamental geomechanical phenomena by examining its mechanical properties, 2) examine the probable improvements on stress-strain behavior and failure modes generated by the use of a rock-like material in the manufacturing of the specimens and 3) quantify the influence of the printing parameters on the strength and deformation behavior and 4) compare the results with the properties of well-recognized natural reservoir rocks.

## **1.2. Objectives of the Research Project**

The hypothesis for this research is that binder jetting additive manufacturing using sand can produce or “print” rocks that mimic the mechanical properties of natural geologic media. Successful testing of this hypothesis will potentially allow reservoir geomechanical tests to be conducted using 3DP rocks that can surmount problems with sample-to-sample heterogeneity, where homogeneity is important, and explore sample heterogeneity as a design parameter.

To test the hypothesis, this research was divided into the following general and specific set of objectives.

### *1.2.1. General Objective*

Characterize fundamental geomechanical properties of 3D printed reservoir sandstone analogues and quantify the impact of the printing parameters on their peak strength, stiffness, stress-strain behaviour and failure mode.

### *1.2.2. Methodology*

- Design and conduct a comprehensive testing campaign composed of uniaxial compression tests, Brazilian tests, direct tension tests and drained triaxial tests and investigate the main mechanical parameters that describe the behavior of a rock material, such as compressive strength, tensile strength, elastic parameters and drained strength parameters.
- Provide sufficient insight on the impact of the main printing parameters: binder saturation, layer orientation and layer thickness on the sandstone analogue’s mechanical behavior.
- Explore the repeatability of the mechanical properties of the 3D printed analogues and establish the extent to which sample-to-sample variability can be eliminated for the diverse types of laboratory tests.

- Analyze and compare the mechanical properties of the sandstone analogues with the existing literature values for some widely studied natural reservoir sandstone formations.

### **1.3. Thesis outline**

This research project is divided into seven chapters. A general description of the contents included in each section is given as follows:

- Chapter 1 - Statement of the problem, objectives of the research project, thesis outline and scope and methodology.
- Chapter 2 - Additive manufacturing technology applied to geomechanics: Literature review of 3D printing techniques applied to geomechanics, specifics about 3D Printing technology using silica sand and furan binder, high-temperature curing process and general printing procedure
- Chapter 3 - Description of laboratory testing program: Description of main 3D printing parameters, a matrix of experimental campaign, statistical analysis of the dimensional accuracy of 3DP analogues, UCS testing procedure, Brazilian test procedure, direct tension test procedure and drained triaxial test procedure.
- Chapter 4 - Results from uniaxial compression testing program: Effect of binder saturation, the effect of layer orientation and effect of layer thickness on the mechanical behavior of 3DP sandstone analogues. Effect of high-temperature curing process on the ultimate strength of the specimens.
- Chapter 5 - Results from tension testing program: Brazilian test results, direct tension test results.
- Chapter 6 - Results from the consolidated drained triaxial testing program: compressibility and volumetric behavior of 3DP sandstone analogues, the influence of confining stress on the mechanical behavior of 3DP sandstone analogues.
- Chapter 7 - Conclusions and recommendations for further research work.
- Chapter 8 - Literature References

#### **1.4. Scope**

This research is focused on the study of the mechanical behaviour of the 3D Printed sandstone analogues under the specific boundary conditions proposed by the geomechanical testing proposed in the previous section. Relationship of the results presented in this document with hydraulic or petrophysical properties is included in parallel research works developed by this research group.

Analysis and conclusions are based upon the results obtained from laboratory tests conducted on 3DP specimens fabricated in the Geo-PRINT facility of the Reservoir Geomechanics Research Group [RG]<sup>2</sup> and conducted in the Geo-REF experimental facilities at the University of Alberta. The mechanical properties of the 3DP material are then compared with those of well-recognized natural reservoir rocks.

This study is focused on standard laboratory conditions chosen with the unique intention of testing the sandstone analogues under extensive and comprehensive boundary conditions. No specific testing was intended to replicate field conditions (i.e. stress path, hydrostatic stress).

## **2. Additive Manufacturing Technology applied to Geomechanics**

### **2.1. State of the Art: Additive Manufacturing Technology**

Additive Manufacturing (AM) technology, popularly known as 3D Printing technology, is a process invented at MIT (Sachs et al. 1993). It was originally referred to as rapid prototyping (RP) technology, a term which is used in many industrial fields, to describe a process by which a system or part can be created from a computational model in a rapid manner, before being publicized or commercialized (Lee et al. 2007). The basic principle of the AM technology is that a virtual model created using Computer-Aided Design (CAD) software or reverse engineering techniques (i.e. object laser scanner), is then converted into a stereolithography (STL) file and materialized by a 3D printing machine.

AM technology has several different techniques for building real parts, including material jetting, binder jetting, material extrusion, among others. Some of the main advantages of this manufacturing process are that, in contrast to other techniques, it requires just basic dimensional details about the element and a basic understanding of how the 3D printing machine works. The method by which pieces are built using AM technology is based on a layer-by-layer process: a thin cross-section of the part, extracted from the original CAD file, is materialized into a layer and added up into the printing area (i.e. a layer of printing powder material is deposited onto the building box and its particles are selectively bound together using a binder material). This process is repeated until the entire shape of the piece is completely generated (Gibson et al. 2015).

3D printing technology has been being studied and applied in different research fields like Health Sciences, on which studies are aiming, among other applications, to completely define a “personalized medicine” for each patient (Rybicki et al. 2015), develop progress in Tissue engineering technology (Kang et al, 2016) and improve the performance of 3D printed tissues on mimicking human responses (Miller, A., 2016); materials engineering (Frketic et al. 2017) and aerospace engineering, on which 3D printed parts are actually being used for aircraft’s parts construction (Hall, 2016).

Although the clear majority of 3D printers produce plastic parts, there are 3D printing techniques that allow the printing of metals (Khaing et al. 2001 and Zhou et al. 2015), ceramics (Seitz et al. 2005) and sand (Gibson et al. 2015 and Gomez et al., 2017). Reduced costs of 3D printers, open-source software, and free access to digital model repositories are opening new avenues for many fields of research. Among these, geosciences are poised to use 3D printing to bridge the gap between computational and experimental analyses (Ishutov et al. 2017).

Even though it has been clearly stated there are uncountable applications of 3D printing among different research fields, the feasibility of its applications on Geosciences remains in its initial stages of research. Es-Said et al. (2000), started to explore the world of rapid prototyping techniques by fabricating ABS P400 (Acrylonitrile-Butadiene-Styrene) or simply, elastomers' solid parts, regularly used in the microelectronics industry, which was subsequently used for tensile and bending testing procedures. Although not directly related to geomechanics' research focus, this first approach obtained meaningful conclusions which can, and will be, applied to the study of the mechanical properties of 3D printed rock analogues. The most noteworthy one was that the ultimate tensile strength and the modulus of rupture of each specimen were remarkably dependent on the inclination of the building planes with respect to the substrate (i.e. base platen of the machine). This phenomenon also occurs in natural sedimentary rocks and it is attributed to the change in failure mode from a tensile cracking to a shear failure through the bedding planes. Furthermore, the fracture path generated at failure occurred along the layer interfaces, which can be caused by weak interlayer bonding and/or interlayer porosity. Behavior also observed in this study.

Bellini et al. (2003), studying the same ABS material, demonstrated that any part built using this RP technique does not exhibit isotropic behavior. Because of the layered-manufacturing production method, the resulting parts have in-plane uniform properties, so they are orthotropic. Similar findings were pointed out by Lee et al. (2007); in this case, the research work was focused on the study of the compressional properties of analogous manufactured materials, concluding also that specimens' ultimate compressive strength and failure modes were influenced by building layer direction, eventually generating an anisotropic behaviour of these properties. Vlasea et al. (2015), explained the existence of

this anisotropic behavior based on the process itself: the orientation of the irregular particles and the influence of the final packing rate on the inter-particle contacts (i.e. sharper contact zones improve the inter-granular strength) within the same building plane, favours the strength of the structure throughout the layer, generating a stronger bonding compared to the one existing between planes. Therefore, as the layer orientation varies, the influence of the shear stresses induced by the loading force (which act at 45° from the applied load) will generate differences on the peak strength and fracture path of failed samples.

Further studies, as the one conducted by Nguyen et al. (2011), focused their attention on determining the influence of the loading conditions on the mechanical response of granular synthetic materials. By the fabrication of granular rock analogue material (GRAM1) specimens, made from well sorted TiO<sub>2</sub> powder, compression and tension tests were performed to determine the constitutive response and failure mode of the material. Results are promising when specifically referring to similarities between rocks and 3D printed materials. The manufactured specimens in this study behave in the same hard/stiff manner as rocks, exhibiting a brittle behaviour at low confining stresses and a ductile one at higher ones. Also, macro failure features (i.e. shear fractures and compaction bands) are analogous to those of natural rocks. With respect to rock parameters, the ratio between compressional and tensional strength ( $\sigma_c/\sigma_t$ ) of the synthetic material is around 8, which is in the same order of magnitude of that encountered on natural sandstones (i.e. 10).

Similar experiments were conducted by Jiang et al. (2015) on Polylactic acid (PLA) specimens. The tensile strength of the specimens showed high dependence on the amount of filling material used during building process (i.e. the higher the filling material, the stronger/stiffer the specimen), which is suitable for future investigations on the influence of structure on rock mechanical properties. Specimens printed for UCS testing were generated by the structural arrangement of circular elements. PLA analogues showed perfect elastic characteristics below yield stress; nonetheless, the post-peak behavior is generally perfectly plastic, which might not be suitable to simulate shear failure in rocks. Furthermore, as compressive stress continues to increase, some of the specimens were squeezed until all void spaces in the assembly were closed and there was no generation of

cracks along a plane of weakness, unlike real rocks; some others failed along lines of weak connections.

Further discussion of the prospective applicability of 3D printed manufactured parts in geomechanics and rock engineering was addressed by Jiang et al. (2016). Based on the results obtained from uniaxial compression and direct shear tests conducted on ABS and PLA specimens, this study presents perhaps the most comprehensive conclusions about the potential applications and current limitations of this technology. Referring to the upsides, the use of AM technology will allow researchers to print rock-like specimens in any shape required. This ability allows the morphology of the printed analogues to be decoupled from the material type, which would enable the study of the role of grain configuration on bulk material constitutive behaviour and the examination of the role of particle-material on the constitutive behaviour while maintaining constant morphologies (Hanaor et al., 2016). Also, AM technology allows the inclusion of specific structures (i.e. fractures, holes, cracks, interlayer features, etc.) and even generate sets of analogues with a unique set of properties such as elasticity modulus, Poisson's ratio or peak strength. Additionally, 3DP specimens manufactured with similar materials can help to overcome the influence of heterogeneity and inter-sample variability on the results and will allow generating analogous physical models to validate simulation experiments. Furthermore, 3D printing technology enables the possibility of fabricating pre-engineering designs to address optimization studies and manufacture of geo-moulds, such as resembling natural joints, to simulate the impact of any boundary condition. Regarding the downsides, peak compressive strength of 3DP techniques still needs to be improved to resemble natural rocks, the clear majority of the currently studied specimens have peak strength of around 10-15 MPa, which is significantly lower than values encountered in natural rocks. Moreover, most of the printing machines used these days have just one or two printing nozzles (i.e. manufactured parts are built using maximum two different materials) and the specimens are limited by the size of the printing job box; technological advances to account for rock-mass size and heterogeneity are required to manufacture more realistic materials.

More recently, Head et al. (2016), extended the use of 3D printing techniques to test the impact of microstructural variations on bulk transport properties of rock analogues.

Porosity and permeability of 3DP analogues that resembles rock-microstructures extracted from CT-scanned real rock volumes were calculated from permeameter data and then used to analyze the influence of compaction and mineral dissolution on the analogue's transport properties. The evolution of 3D printing technology will enable the possibility of access remote and delicate samples and test the impact of these variables on their hydraulic properties. Analogously, Suzuki et al. (2017), created a 3D printed rock fracture network created from CT-scanned natural samples and conducted flow (i.e. tracer) tests to determine the hydraulic properties of the system. The most important advantages that AM technology offers in this field are the ability to know the entire configuration of the model, control the fracture parameters and reproduce the same model throughout the study to ensure total repeatability of the results.

## **2.2. 3D Printing Technology using Silica Sand and Furan Binder**

### *2.2.1. ExOne 3D Printer System.*

In this study, the 3D printed sandstone analogues were manufactured using the Ex-One M-Flex™ 3D Printer System (Figure 2.1), acquired and installed in the GeoPRINT facility at the University of Alberta by the Reservoir Geomechanics Research Group (RG<sup>2</sup>), as part of the Energi Simulation Consortia in Reservoir Geomechanics.

This system uses a recoater to selectively deposit thin (with a minimum thickness of 100 µm or as thin as twice the  $D_{90}$  value of the powder's particle size being used) cross-sectional layers of fine silica sand. Before being placed on the recoater, the sand powder is precoated with an acidic activator that will act as a catalyst for the polymerization reaction of the Furan binder into a resin. Furan binder is a substance responsible for building up the specimens by the generation of adhesive forces between sand grains. This process will take place at the grain contacts, within the pore space of the specimens. Heat is then applied to partially cure the binder and prepare the powder bed for a new recoating.

Furan binder is deposited by a print head equipped with 4x256 piezoelectric binder jets with a resolution of 63.5 by 63.5  $\mu\text{m}$ , which pass over the sand powder bed. With each successive pass of both the recoater (i.e. sand layer deposition) and the print head afterwards, a higher percentage of the entire volume of the specimen is bound until a complete shape-object is built (Osinga et al., 2015). Depending on the number of samples being printed and the area of the horizontal layer that is being utilized during the job, the recoating and binding processes could take between 20 and 30 seconds per layer, which is a suitable rate for high-volume specimen's production.

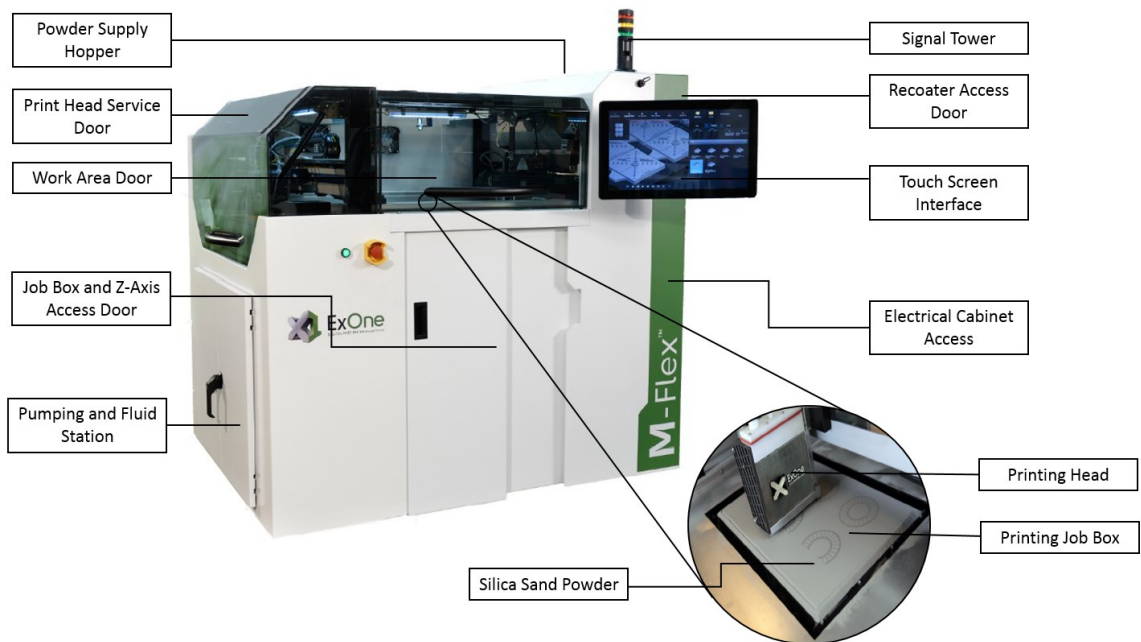


**Figure 2.1. 3D Printer System specifications (Modified from ExOne Manual, 2014)**

The printer system is comprised mainly of a powder supply hopper, a recoater assembly, a pumping and fluid station, a print head and a printing job box. The powder supply hopper, as its name indicates, is a powder reservoir that stores the silica sand that will be dispensed into the recoater when required during the printing process. The recoater is an assembly that deposits a precise layer of powder onto the print bed. The thickness of the layers is defined by the user at the beginning of the printing job and remains constant through the

entire process. The pumping and fluid station functions as a storage space for the binder, cleaner fluid, and waste reservoirs. It also provides fluid access in and out the printing box and accommodates pumping and vacuum systems. The print head is an assembly that selectively deposits binder onto the powder bed; an X-Axis and a Y-Axis move the print head carriage in the X and Y directions respectively. Finally, the job box contains the powder bed and the printed parts. The touch screen interface allows a user-friendly operation of the printer (ExOne M-Flex User Manual, 2014.).

### *2.2.2. Silica Sand*

Silica Sand is one of the widely-known varieties of sand in the world, it is used for many applications as moulds' creation, industrial castings and fabrication of construction aggregates. Silica sand is characterized by containing a high proportion (more than 95%) of silicon oxide ( $\text{SiO}_2$ ) and more significantly, a very low content of impurities as clay, iron oxides and refractory minerals (British Geological Survey, 2009). One of the most prominent advantages of using this material for 3D printing applications is that it does not require changes at the foundry. Moreover, when building the 3D analogues using Furan binder, the resulting parts are considered a “no bake” product, this is to say, silica sand specimens does not require thermal treatment and can be used immediately after being manufactured (ExOne Industry Grade Materials, 2017). Nonetheless, as described later in this thesis, a thermal treatment helps in the crystallization process of the Furan and therefore increases its strength; this is an essential step to accomplish more competent and strong samples, with properties that share more similarities with those of natural rocks.

Another important property to be mentioned of Silica sand is that is characterized by having a narrow grain size distribution. This point is relevant when analyzing the homogeneity of the resultant pore structure of the sandstone analogues and the uniformity and low inter-sample variability of their properties. The sand specification used for manufacturing the specimen's testes in this study was M4000 and the particle size distribution (PSD) curve is shown in Figure 2. The analysis was performed using 120 grams of sand.

From the PSD curve, useful information such as the  $D_{10}$ ,  $D_{60}$  and  $D_{90}$  of the M4000 sand can be computed, which are respectively: 115  $\mu\text{m}$ , 195  $\mu\text{m}$  and 235  $\mu\text{m}$ . Using the previous data, the coefficient of uniformity ( $C_u$ ) of the material can be calculated using Equation 2.1

$$C_u = D_{60}/D_{10} \quad \text{Equation 2.1.}$$

Materials with a  $C_u$  lower or equal to 4, are “poorly graded” or uniform (Swan et al. 2017). Therefore, as the ratio of  $D_{60}/D_{10}$  for the M4000 Silica sand is 1.70, the resulting sandstone analogues can be considered composed of a uniform material.

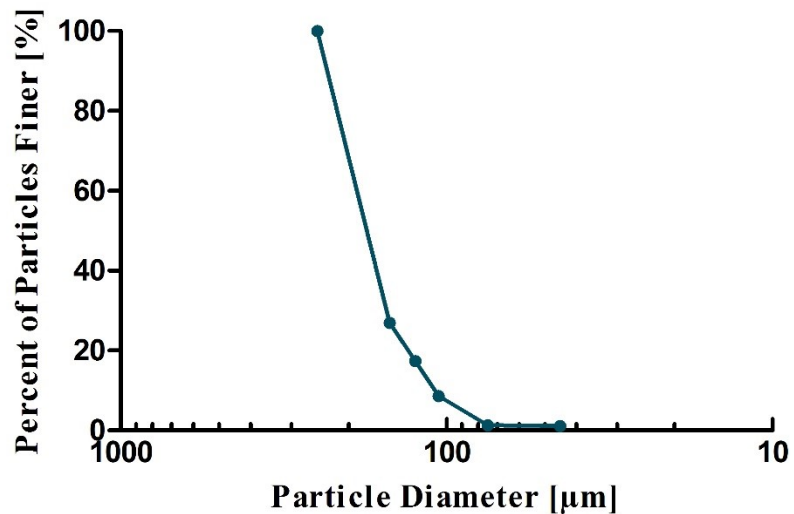


**Figure 2.2. Particle Size Distribution of Silica Sand**

### 2.2.3. Furan Binder

The FB001 binder is a brown fluid manufactured and supplied by ExOne GmbH and specified as the substance/mixture needed to produce casting moulds and cores. FB001 has a pH value between 6 to 8, a boiling point of 170°C and a flash point between 65°C and

80°C. Furan binder is highly reactive with acids and acid-forming substances and is known to generate strong exothermic reactions with those types of substances (ExOne Safety Data Sheet, 2015). For this reason, the sand is coated with an acidic activator mainly composed of p-toluenesulphonic acid prior to printing to allow polymerization of the Furan binder into a resin inside the pore structure of the specimens. The detailed composition of the FB001 binder is listed below in Table 2.1.

The main safety precautions associated with handling the product require personal protective equipment (PPE) for hands, eyes and body (i.e. protective work clothing) and a protective respiratory device that does not allow fumes penetration. Good ventilation/exhaustion must be ensured at the workplace because fumes combined with air can generate explosive mixtures. FB001 must be stored far from acids and ignition sources and kept tightly sealed to avoid aerosols formation.

**Table 2.1. Major Chemical composition of Furan Binder**

Component	Weight Ratio [%]
Furfuryl Alcohol	70- 90
Bisphenol A	5- 15
Resorcinol	1- 10
3-aminopropyltriethoxysilane	0.1- 0.2

#### *2.2.4. Acidic Activator*

The FA001 activator is a brown fluid also manufactured and supplied by ExOne GmbH and specified as the hardening agent/curing agent to produce casting moulds and cores fabricated with furan binder. FA001 is mainly composed of p-toluenesulphonic acid (with a maximum content of 5% of H<sub>2</sub>SO<sub>4</sub>), it has a pH value lower than 1 and a boiling and flash points of approximately 100°C. It also has a density of 1.2- 1.3 g/cm<sup>3</sup> and a vapour

pressure (measured at 20°C) of 2.3 kPa, which makes it volatile. Main safety precautions relate to handling the product require personal protective equipment (PPE) for hands, eyes and body (i.e. protective work clothing) and a protective mask that does not allow odours penetration. Good ventilation/ exhaustion must be ensured in the workplace (ExOne Safety Data Sheet, 2015).

### **2.3. High-Temperature Curing Process**

Primkulov et al. (2017) found that the peak strength of the sandstone analogues can be highly improved by subjecting the specimens to a high-temperature curing period immediately after being printed.

The physics behind the mechanism of a specimens' 'curing process' involves the previously mentioned exothermic reaction generated between the acid activator and the Furan binder, which occurs immediately when they are in contact with each other. This chemical process generates a certain amount of heat that helps the Furan binder to crystallize inside the pore structure of the sandstone analogue. Nonetheless, the amount of binder that is cured depends on the equilibrium between the reaction's generated heat and, at the same time, the Furan evaporation rate to the atmosphere. In addition, at the last stages of curing, one of the products of this reaction, when it is completed at atmosphere temperature, is water. Once generated, this fluid is going to sit inside the pore media of the sample and might generate ring hydrolysis of the monomers (McKillip et al., 1989) as well as the creation of macropores within the resin (Gaefke et al., 2007) that diminish the ultimate strength of the material.

Increasing the surrounding temperature will benefit the polymerization reaction of the Furan resin by catalyzing it (i.e. accelerating the complete curing process of the specimens, before binder gets evaporated from the sample) and avoiding the presence of an undesirable amount of water inside the pores of the analogue, thereby producing stronger analogues.

The high-temperature curing process initiates during the printing job. After each pass of the print head over the job box, with the subsequent sand recoat, a heat emitter functioning at 50% of its power (which corresponds to an average temperature of 40°C) will heat up each layer of the to-be-printed analogues. Furthermore, after the printing job has concluded, the specimens will be placed in a furnace at a temperature of 80°C. This specific temperature was chosen after analyzing the results of UCS tests performed on specimens with no thermal treatment applied (i.e. curing at atmosphere temperature) and specimens treated with temperatures up to 200°C. The influence of the curing temperature on the peak strength of the sandstone analogues is shown in Figure 2.3. It could be seen that for temperatures higher than 115°C, the UCS peak strength of the specimens gets negatively influenced by temperature, also, after remaining more than 100 hours inside the furnace, specimens from all groups exhibit a clear decrease in their average peak UCS strength.

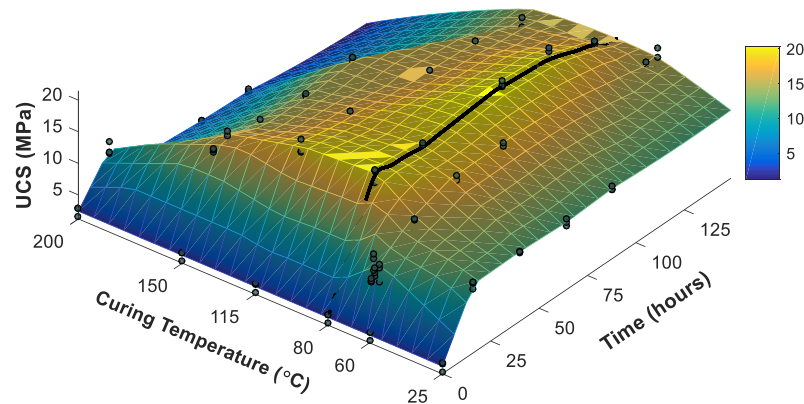


**Figure 2.3. Influence of Curing temperature on the peak UCS strength of the reservoir sandstone analogues (after Primkulov et al., 2017)**

## 2.4. General Printing Procedure

A part (typically a cylindrical specimen/ batch of specimens) is produced for geomechanical testing and/or characterization, using AM technology (3D Printing) with

silica sand and furan binder material. To do so, the printing system, printing materials, auxiliary equipment and the lab, in general, must be prepared for operation, the printing process must be performed following the Task Specific Instructions (TSI) outlined below. Once the process has been completed, the printed objects must be retrieved and prepared for curing stage (RG<sup>2</sup> Task Specific Instruction for 3D Printing, 2016). To better understand how the 3D printed specimens are prepared, a brief overview of the TSI is provided below.

#### *2.4.1. Step-by-step Printing Procedure*

- 1- Ensure to have all the personal protective equipment needed for starting the printing procedure.
- 2- If required, fill out a Hazard Assessment. If it is not, take some time to go over the hazards mentioned in the posted hazard assessment and check to see whether they all apply and if new hazards should be added.
- 3- Inspect the state of the lab. If there is clutter, clean it up.
- 4- Bring in two 50 lbs buckets of clean silica sand. Position them such that they do not present a tripping hazard while working.
- 5- Check the levels of binder, cleaner, and waste on the pumping system before the print job. The waste container should be at least half empty.
- 6- If Binder/Cleaner reservoirs need to be refilled, an organic material spill kit should be readily available during the binder refill. Use hand pump to transfer liquids from one container to another. Wipe the hand pump after use. Use of respiratory protective equipment is necessary.
- 7- If the job box is not in the printer, insert the job box into the printer using the transfer cart.
- 8- Close all printer doors. Start print head on the touch screen. Wait for the wiper station to fill up and for the print head to finish its wiping cycles.

- 9- Print test pattern. The pattern will most likely show some jets missing. This is acceptable. If 3 or more jets in a row are missing, set the print head wiping function again and then Print test pattern. Repeat until results are acceptable.
- 10- Select the printing files (external geometry of the specimens). Add each part to the digital printing box. Ensure the dimensions that the part will have are correct. If not, scale them to the right values. Use the positioning and rotation buttons to place the part in the desired manner. Save final layout.
- 11- Mix a minimum of three batches of sand and activator according to the recipe below. Add each batch to the supply hopper on the M-Flex.
  - Add 3500 grams of sand to the Kitchen Aid bowl. Insert into the mixer, put on dough blade.
  - Turn mixer to lowest setting and raise bowl. Over 8-10 seconds, add 5.7 grams (5 mL) of activator
  - Mix on level 2 for 15-30 seconds (longer mixing time is suggested when humidity is above 40%, in each interval). Mix on Level 4 for 45 seconds to 1.5 min.
  - Turn off mixer, remove the cover, scrape sides and blade, and return cover.
  - Mix on Level 5 for an additional 1.5 min to 3 min (depending on room humidity).
  - Spread sand as uniformly as possible the sand onto the hopper.
- 12- Set 20 to 25 sand recoats to ensure the job box have a very smooth sand base. If the base is not smooth do not continue. Resolve the issue and create a level, smooth base.
- 13- The printer system will now check if everything is ready for printing. Visually confirm whether everything is ready for operation.
- 14- Start the printing process. Attempt to match the printing speed so that the sand has a relatively constant residence time in the printer. It is useful to have a benchmark for when to make and add a new batch of sand.
- 15- Cover the printed parts with some extra sand layers (5-10)
- 16- Let the printed parts set for 10 to 15 minutes, based on printing binder saturation used for the job.

17- Extract the printing box from the printer.

#### *2.4.2. Specimens' Curing Process*

- 1- Extract the freshly-printed specimens from the printing job box and dispose of them onto a metallic pan reserved for this purpose.
- 2- Turn on the furnace and set the system to a constant temperature of 80°C (176 °F).
- 3- Introduce the pan with the samples and let them cure for 24 hours or until the colour changes from light green to a darker tone (olive).

#### **2.5. Closing remarks on the application of AM technology in Geosciences**

Previous attempts at applying AM technology to laboratory testing campaigns in geosciences were performed using samples fabricated with polymers or metal powders. Those studies showed that either the properties (i.e. porosity, crack initiation/coalescence and failure mode) of the resulting samples were different from those of natural rocks or the peak strength or stiffness of the parts was considerably lower than natural rocks.

The use of Silica sand and Furan binder as main components in the manufacturing process of 3D printed sandstone analogues are expected to overcome these limitations and to help to obtain defensible and competent specimens, with comparable properties to those encountered in natural sandstones. In addition, the utilization of a granular material cemented by a different material (as occurs in natural rocks) will allow researchers to study the influence of stress state and stress path on compressibility, peak strength, stiffness and failure mode of the sandstone analogues, as well as analyzing interrelated-phenomena as pore collapse (Menendez et al. 1996), grain-crushing (Zhang et al. 1990) or cement degradation.

### **3. Description of Laboratory Testing Program**

#### **3.1. Introduction**

The technique used by the ExOne 3D Printer system to build the sandstone analogues tested in this study is known as layered manufacturing process (Fereshtenejad et al. 2016). This means that every cylinder used for conducting the tests was built using a layer-by-layer progression. As specified previously, a recoater drops a layer of silica sand at a determined thickness established by the user. Then, a print head drops a specific volume of binder fluid that is going to polymerize and adhere to the surface of the grains, generating the intergranular bonding forces that will finally build the sample up. This process can be considered uniform if just one layer at a time is analyzed but it is important to determine whether layer-by-layer construction of the full specimen has any influence on the final properties of the printed specimen.

While the 3D printed materials' advantages related to manufacturing efficiency have been previously discussed, there is still an urgent need to understand the influence of every specific building parameter, inherent to the 3D printing process itself, on the resultant sandstone analogues. Three different printing features including binder saturation, layer orientation and layer thickness were varied to analyze the geomechanical behavior of the sandstone analogues. Furan saturation and layer thickness are directly related to the amount of binder present on the pore space of the specimen and thus with the strength of the material.

Consistent sandstone analogues with the maximum possible strength are desirable for geomechanical testing purposes. Meanwhile, the orientation angle of the printing layers is an essential parameter to comprehend whether the bonding forces between printing layers are strong enough to not become a weakness plane, a factor that could be dominant on the strength and mode of failure of the samples.

## 3.2. Main 3D Printing Parameters

### 3.2.1. Binder Saturation

Binder saturation is expressed as a fraction and is defined as the percent of void space between the powder's particles that is filled with Furan binder. As the technology used by this specific 3D printer machine utilizes a layered construction process to manufacture the cylindrical specimens (Gao et al., 2015), this “desired” saturation value is achieved by maintaining a constant value for each building plane. The binder's drop spacing, expressed in micrometers, is fixed by considering the thickness of the layer used for the actual printing job.

The computed binder saturation is provided as a mean to quantify how much binder is dispensed into each unit volume of printed material. This parameter depends on the powder packing rate (percentage of void space that exists in the printing material after binder spreading), X-Axis drop spacing ( $X_{sp}$ ), Y-Axis drop spacing ( $Y_{sp}$ ), layer thickness and drop volume (volume of a single drop generated by the print head), and can be calculated using Equation 3.1. Three different binder saturations levels were studied for this part of the project, 10%, 15% and 20%.

$$Saturation [\%] = \frac{100,000 * Drop Volume}{\left(1 - \frac{PowderPackingRate}{100}\right) * X_{sp} * Y_{sp} * Z_{sp}} \quad \text{Equation 3.1.}$$

To ensure that the mechanical behavior was strictly related to changes in this parameter, every sample was printed horizontally (layers are aligned to the direction of the axial load during the UCS test) and tested after being left to cure at room conditions (i.e. temperature and humidity).

The porosity of some UCS specimens was measured by mercury injection tests (MI) (Ardila et al., 2017). It was found that for the samples printed with the base case properties (10% saturation, 250  $\mu\text{m}$  layer thickness), the average porosity was 46.7%, meanwhile for

the specimens printed with 20% binder saturation the interstitial porosity calculated from the tests results was 35.7% (Ardila et al., 2017). Therefore, subtracting the porosity results and assuming an equivalent packing ratio of the sand powder in both cases, around 11% of a 10%-Binder-Saturation specimen will be composed by the volume of Furan binder required to manufacture it, while for a 20%-Binder-Saturation specimen the percentage in volume of binder will be around 22%. The fact that the porosity of the analogues is reduced with the further increase of the binder saturation and, certainly, the presence of a higher amount of cured resin within their pore structure, favors their peak UC strength, as it will be further noticed.

### *3.2.2. Layer Orientation*

Layer orientation corresponds to the inclination angle of the building planes with respect to the direction of the application of the axial load in a conventional compression test. While the printing process is being conducted, the Furan binder fluid is sprayed over each layer, having some seconds to partially react with the acid-activated sand and crystallize until the next layer is deposited. Therefore, each layer has approximately uniform “in-plane” properties but could have different ones throughout the thickness of the specimen.

Because of this condition, the 3D printed sandstone analogues can be classified as a transversely isotropic material, as most sedimentary and metamorphic rocks, and the impact of the building layer orientation along the Z Axis (axis of symmetry) of the samples must be studied to determine whether is influential on their ultimate UCS strength (Fereshtenejad et al. 2015)

To analyze the repercussion of this parameter on the mechanical properties of the 3D printed sandstone analogues, separate groups of specimens were printed with 0°, 25°, 45°, 65° and 90° inclination measured with respect to the axial load application direction or Z Axis. A representative illustration of this concept is exhibited in Figure 3.1. The dashed lines represent the direction of the axial stress, while the light-green lines represent the direction in which planes are going to be oriented during the printing process.

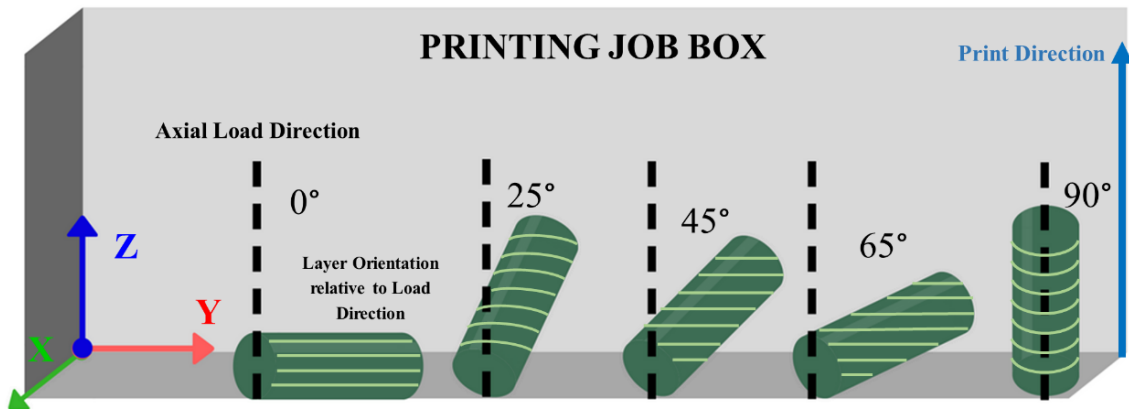


**Figure 3.1. Representation of layer orientation of 3D printed specimens**

### 3.2.3. Layer Thickness

Layer thickness, expressed in micrometres, is defined as the width of each layer of powdered material (i.e. silica sand) deposited onto the printing job box base along the Z axis and corresponds to the Z drop spacing parameter ( $Z_{sp}$ ) in the Saturation equation (Equation 3.1.) presented previously. This parameter is defined by the user on the process settings prior to starting the job and is kept constant for each specific printing process.

To study the influence of the layer thickness on the ultimate strength and stiffness of the 3D printed analogues, there were two cases chosen: 250  $\mu\text{m}$  (Base case) and 400  $\mu\text{m}$ , maintaining a constant saturation of 10% for each one of them and an inclination angle of 0°.

The thickness of the layers also has effects on the duration of the printing process. For the case of a 38.1 mm by 76.2 mm (1.5" by 3") specimen, it takes a total of 153 layers of 400  $\mu\text{m}$  to completely built the part, while using a thickness of 250  $\mu\text{m}$  to manufacture the exact same specimen, implicates 312 layers to finish the printing process; which can be translated into approximately twice the duration. However, as it will be appreciated in upcoming sections, the peak strength of the specimens built with thicker layering is sacrificed.

### 3.3. Matrix of Experimental Campaign

Table 3.1 includes the detailed information about the number of specimens printed for each type of mechanical testing procedure. It is important to mention that the groups of analogues used for UCS tests were not subjected to the high-temperature curing process because the advantages of this process were discovered after the time they were performed.

**Table 3.1. Matrix of Experimental Testing Campaign for Mechanical Characterization of 3D Printed Specimens**

Type of Test	Experimental Design		Calculated Mechanical Properties
Uniaxial Compression Tests (UCS)	Influence of Binder Saturation	5 specimens for each binder saturation level (10%-15%-20%) Total: 15 samples	UC Peak Strength, Young's Modulus (E), Poisson's Ratio ( $\nu$ )
	Influence of Layer Orientation	4 specimens for each layer orientation variation (0°-25°-45°-65°-90°). Total: 21 samples	
	Influence of Layer Thickness	5 specimens for each layer thickness (400 $\mu$ m) Total: 5 samples	
Brazilian Tests (BT)	5 specimens for BT experiments. B. Saturation: 10%, Layer Orientation: 0° Layer Thickness: 250 $\mu$ m		Tensile Strength
Direct Tension Tests (DT)	11 specimens printed horizontally (0°) and 4 specimens printed vertically (90°). B. Saturation: 10%. Total: 15 samples.		Tensile Strength
Consolidated Drained Triaxial Tests (CDTx)	1 specimen for compressibility analysis and 3 specimens to determine drained strength parameters and Mohr-Coulomb envelope. Total: 4 samples. B. Saturation: 20%, Layer thickness: 250 $\mu$ m.		Bulk Compressibility, Drained Strength Parameters ( $c'$ and $\phi'$ ), Young's Modulus (E) and Poisson's Ratio ( $\nu$ )

At that stage of the research project, the findings regarding the improvement in both strength and stiffness of the sandstone analogues for the elevated temperature curing process were not available. For this reason, and looking forward to being able to compare the uniaxial peak strength of the parts with their corresponding tensile strength, Brazilian tests and direct tension tests were also performed on “green” (non-cured) specimens.

The specimens used for UCS testing were cylinders of 38.1 mm diameter by 76.2 mm length (1.5” by 3”). Brazilian test specimens were cylinders of 54 mm diameter by 22 mm length, these proxies were printed horizontally (i.e. 0°-layer orientation), at a binder saturation of 10% and a layer thickness of 250  $\mu\text{m}$ , Figure 3.2. Direct tension specimens were built using a “Dog-Bone” shape with the dimensions specified in Figure 3.3; they were also fabricated using a 10% binder saturation and a layer thickness of 250  $\mu\text{m}$ .

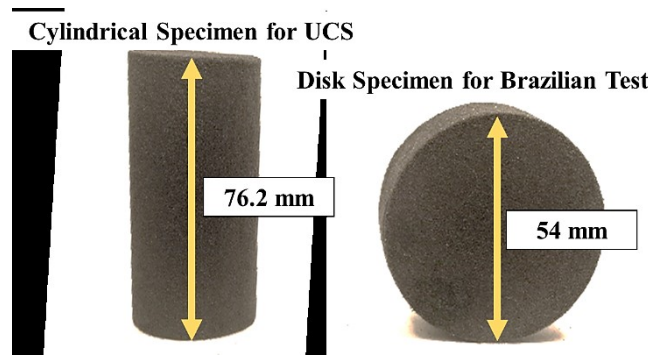


**Figure 3.2. UCS and Brazilian Test 3D Printed Specimens**

For the triaxial testing campaign, thermally-cured specimens of 63.5 mm in diameter by 127 mm in length (2.5” by 5”), built using 20% binder saturation was used. As the duration of each triaxial test is considerably longer than any of the previous ones, this group of analogues were submerged in sealed containers filled with silicone oil (viscosity of 174 cP) to avoid contact with atmospheric humidity. The selection of the pore fluid was performed based on a study conducted by Ardila et al. 2017, on which several UCS tests were performed on samples with different time-exposures to either tap water or silicone oil.

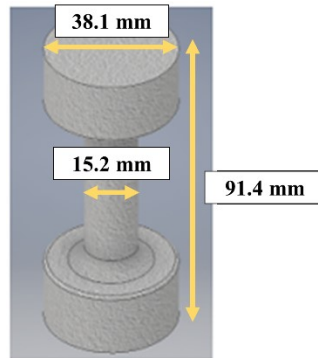


**Figure 3.3. 3D printed direct tension specimen with dimensional specifications**

According to these experiments, the 3DP sandstone analogues submerged in tap water registered an average reduction of about 42% on their UC peak strength (when comparing  $\sigma_p$  to the initial UC strength of an “undisturbed” or freshly-printed specimen). On the other hand, the specimens that were submerged in silicone oil, achieved an average reduction of just 5%, if the previous comparison is considered once again. One possible explanation for the remarkable reduction occasioned by tap water was previously explained in [Section 2.3](#); in addition, silicone oil is known to be an inert fluid, which is an important feature when no-reaction between the pore fluid and the structure of the sample is desired.

#### **3.4. Descriptive Statistical Analysis of the UCS Specimens**

Because of the extensive variation of printing properties used during the building process and the number of specimens used for the tests (36), the population of 38.1 mm diameter by 76.2 mm height (1.5” by 3”) UCS specimens were chosen for the descriptive statistical analysis of the dimensional consistency of the specimens built by AM process.

One of the most important advantages of the 3D printing technology is the ability to print virtually exact replicas of any model. To confirm this aspect from the dimensional point of

view, each cluster of specimens was meticulously measured in both diameter and length and the results are shown in Table 3.2

**Table 3.2. 3D printed UCS analogues average dimensions.**

<b>Number of Samples</b>	<b>Binder Saturation [%]</b>	<b>Layer Orientation [Degrees]</b>	<b>Layer Thickness [<math>\mu\text{m}</math>]</b>	<b>Average Diameter [mm]</b>	<b>Average Length [mm]</b>
5	10	0	250	38.5	76.7
4	10	25	250	38.6	76.9
4	10	45	250	38.3	76.7
4	10	65	250	38.3	76.8
4	10	90	250	38.8	76.9
5	15	0	250	38.5	76.7
5	20	0	250	38.6	77.1
5	10	0	400	38.5	76.6
<b>Final Average Value</b>				<b>38.5±0.07</b>	<b>76.8±0.07</b>

The average diameter of the actual 3D printed UC analogues is 38.5 mm, which is 1.08% higher than the expected theoretical value of 38.1 mm. With respect to the length, the overall average value is 76.8 mm, which is 1.56% higher than the theoretical value of 76.2 mm. These slight variations could be explained by the calibration of the Furan drop volume of the system or to a slight migration of the Furan to unsaturated pore spaces of adjacent zones. This can be corrected by performing a “Drop Volume Test”, which is a rectification of the volume of Furan dropped by the print head, based on an averaged mass of binder dropped by the system after three repeats. For upcoming tests, this calibration was performed before starting each printing process and aided to eliminate these slight dimensional inconsistencies.

The specimen homogeneity was evaluated using a descriptive statistical analysis, which was performed separately for dimensions of the cylindrical specimens. Table 3 displays the results obtained for each distinct group of specimens. As it can be appreciated, both diameter and length of the specimens showed a consistent dimensional behavior, ranges of

data are lower than 1 mm for both magnitudes and the coefficient of variation (CV) and standard deviation of the measurements are considerably low. If these upsides are added to the fact that there is no coring damage (Yan et al., 2017) or sampling-induced disturbance effects (Carroll & Long, 2017) on the 3D printed specimens, this manufacturing process possesses a valuable advantage over conventional sample-extraction methods.

**Table 3.3. Descriptive Statistical Analysis of the dimensional consistency of 3D Printed UCS specimens**

Parameter	UCS Specimens Statistical Analysis					
	Mean [mm]	Range [mm]	Standard Deviation	Confidence Intervals (95%)		Coeff. of Variation CV (%)
<b>Specimen Diameter [mm]</b>	38.51	0.75	0.19	38.5	38.6	0.49
<b>Specimen Length [mm]</b>	76.80	0.77	0.20	76.7	76.9	0.26

The fact that the CV of the specimen’s diameter is almost twice the CV of the specimen’s length might suggest that the 3DP analogue’s height remains more affected and is more accessible to control when compared to their diameter. Nevertheless, the average diameter of the population of cylinders deviates less from the theoretical manufacturing value than their average length. This phenomenon could be related to the balance between gravitational, viscous and surficial energy (i.e. surface tension) of the furan binder inside the silica’s porous structure. The absence of a competent layer contiguous (i.e. at the base) to the specimen during the printing, the orientation of the building planes (25°, 45°, 65° or 90°), or the time required for the complete polymerization reaction of the Furan binder to be completed, resulted in variations on the value of specimens’ diameter and slight deformations with respect to the theoretical cylindrical shape, as shown in Figure 3.4.

This behavior was pointed out by Wang et al., 2004, Cueto-Felgueroso & Juanes, 2009 and Chapwanya & Stockie, 2010: the infiltration of a fluid on a non-saturated porous medium depends on the relationship between the destabilizing gravitational forces and the viscosity

of the fluid. The curing time of the furan binder is reduced by an increase of the process' temperature, therefore, at ambient conditions; the volume of furan deposited on each building layer of the specimens may not be completely cured by the time the next layer is deposited. As the printing process goes on, and so the amount of non-cured binder, a certain amount of liquid binder drops out from the original shape, resulting in undesirable dimensional variations. It is believed that this behavior could be influenced by the higher relative permeability to the binder of the already bounded zones. A smaller amount of energy is required by the fluid to travel along the body of the specimen rather than bleeding vertically towards lower dry zones.

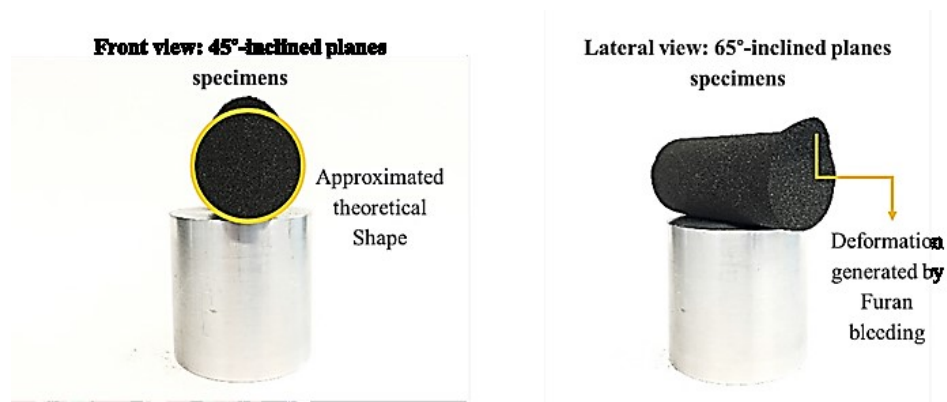


**Figure 3.4. Shape deformation on specimens printed with inclined building planes.**

These issues were solved by installing a heater assembly on the recoater of the printer. As each sand layer was deposited and the corresponding volume of binder subsequently added by the printhead, with the upcoming pass of the recoater, the previous layer will be heated to an approximated temperature of 40°C. These new conditions will favour the time required by the polymerization reaction of Furan to be completed, so there will be no “free” amount of fluid inside the pore space of the specimens to flow and bleed from their theoretical volume. The specimens used for the analysis presented in the upcoming section were printed using this new feature.

### 3.5. Unconfined Compression Test Procedure

The stress-strain relationship and the peak strength of the 3D printed sandstone analogues were determined using the axial force exerted by a 400 kN INSTRON 5988 system under uniaxial stress conditions. For measuring axial and radial displacements during the UC tests, two types of linear variable displacement transducer (LVDT) systems were set up for each sample: two LVDTs (Measurement Specialties 250MHR-1502) for calculating axial displacement mounted on two parallel rigid metallic discs with a range of 12 mm and an accuracy of  $\pm 25.4 \mu\text{m}$  and one LVDT (Measurement Specialties 100MHR-3008) for calculating radial displacement with a range of 6 mm and an accuracy of  $\pm 25.4 \mu\text{m}$ .

Additionally, each specimen was placed on top of a rigid stainless-steel cylinder with the purpose of situating the analogue within the range of movement of the load frame. The exact experimental setup, as well as a representative configuration of the data logging system used for the UC tests, is shown in Figure 3.5.

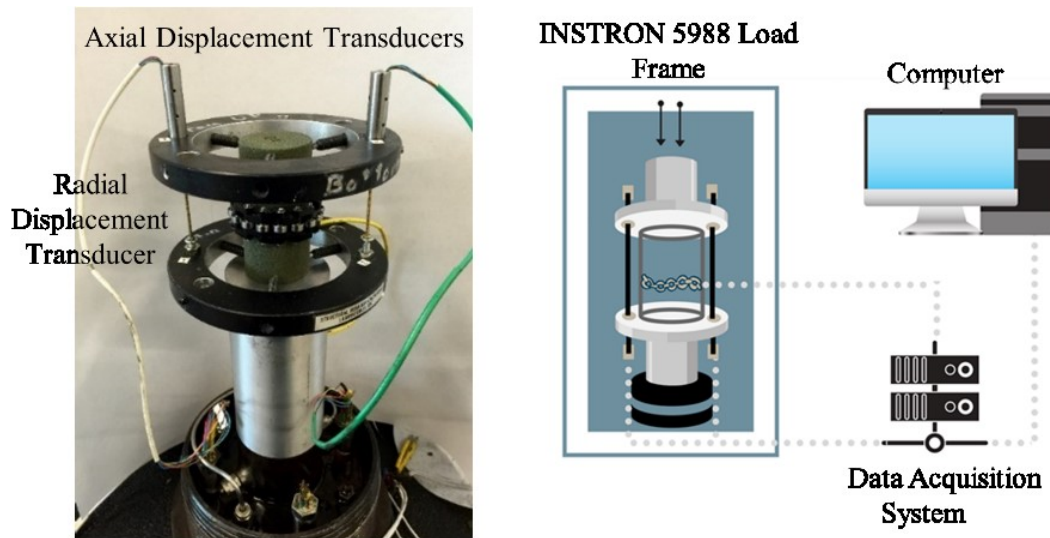


**Figure 3.5. Experimental Setup and Data Logging configuration for UCS Tests on 3DP Specimens**

The entire UCS testing campaign was conducted on 38.1 mm diameter by 76.2 mm length, non-thermally cured (green) specimens, built using the process heat emitter and before being tested the specimens were stored in a sealed container at atmospheric temperature. The variations in the printing parameters (i.e. binder saturation, layer orientation and layer thickness) were systematically performed, so the impact of each one of them on the mechanical behaviour of the analogues could be separately accounted.

The measured data was recorded automatically by the GeoREF data logger software, which was developed within the Research Group (RG<sup>2</sup>) and coded in LabVIEW. The loading procedure and the corresponding calculations of stress, strain and elastic properties were performed following the standards proposed by ASTM D7012-14. The strain rate was fixed at 0.25 mm/min.

### **3.6. Brazilian Test Procedure**

The Brazilian tensile strength is determined by an indirect method on which a continuous compressive force exerted by a loading device is converted by an arrangement of platens into a theoretical single-point load, that develops an even tensile stress along the entire central region of the specimen. This test is governed by ASTM D3967-08 (2008) standards and the stress at failure ( $\sigma_t$ ) is a function of the applied load (P), specimen diameter (D) and specimen thickness (t) and can be determined by Equation 3.2 (Perras & Diederichs, 2014). The ratio thickness-diameter (t/D) is suggested by the standards to be between 0.2 and 0.75. For the case of the 3DP Brazilian specimens used for these tests, this ratio is exactly 0.41.

$$\sigma_t = \frac{2P}{\pi t D} \quad \text{Equation 3.2.}$$

To analyze the tensile properties of the 3D printed rock analogues, 5 Brazilian Test specimens of a theoretical diameter of  $54 \pm 0.2$  mm and a thickness of  $22 \pm 0.18$  mm were

printed horizontally ( $0^\circ$  layer orientation), with a binder saturation of 10% and a layer thickness of  $250\mu\text{m}$ . These specimens were also built using the process hear emitter and were also stored in a sealed container at room temperature before starting the tests.



**Figure 3.6. Experimental Setup and Data Logging configuration for Brazilian Tests on 3DP Specimens**

The compressive force was transmitted by a 150kN INSTRON 3384 and converted into localized tension by a pair of GCTS curved loading jaws as it can be seen in Figure 3.6. The strain rate used on this testing campaign was 0.17 mm/min, to reach an average time to failure of 6.7 minutes (6 minutes and 42 seconds approximately); which is in accordance with the suggestions of the ASTM standards. The measured data was also recorded automatically by the GeoREF data logger software.

### **3.6. Direct Tension Tests Procedure**

Direct Tension (DT) testing is one of the most accepted methods for determining the true tensile strength of a material. The use of Dog-bone shaped samples benefits the stress concentration at the ends of the specimens, reducing the probability of occurrence of a not-valid failure far from the middle area of the specimen. The calculation of the peak tensile

strain of the sandstone analogues is obtained by dividing the peak axial force ( $F_a$ ) into their cross-sectional area (Perras & Diederichs, 2014), Equation 3.3.

$$\sigma_t = \frac{F_a}{A_c}$$

**Equation 3.3.**

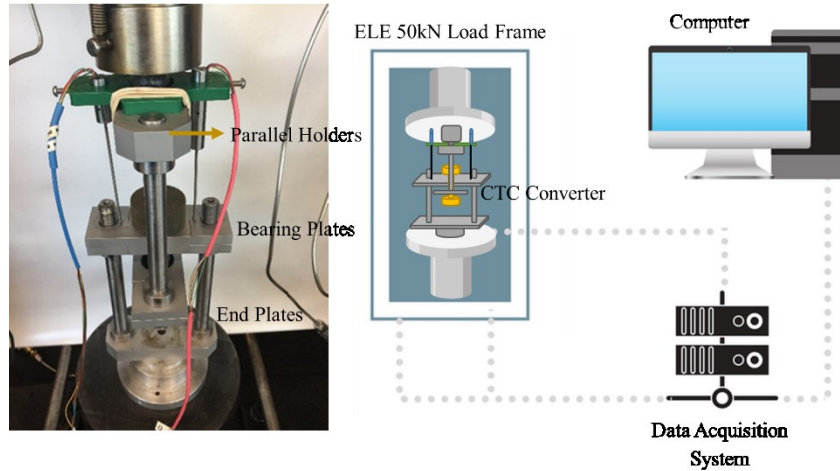


**Figure 3.7. Direct Tension Testing setup and Data Logging configuration for 3D Printed specimens**

To perform Direct Tension Test campaign, 15 Dog-Bone Shaped specimens (11 with 0°-oriented building planes and 4 with 90°-oriented building planes), with the dimensions previously specified on Figure 3.3, were printed using the same basic printing properties used for the Brazilian Test specimens. These specimens were not thermally-cured either and were also stored in a sealed container for a week, at room temperature, before starting the tests.

The compressive force was transmitted by an ELE 50 kN Digital Tritest load frame and the axial strain was measured by using two diametrically opposed axial LVDT's (Measurement Specialties 100MHR-3008), with a range of 6 mm and an accuracy of  $\pm 25.4\mu\text{m}$ , were mounted on a 3D printed plastic holder (i.e. green part). For the purpose of converting the compressive force exerted by the load frame into tensional force, a

compression-to-tension load converted (CTC), built by GeoREF staff based on the design proposed by Fuenkajorn & Klanphumeesri, 2010 was used. It is composed of two parallel holders, two end plates and two bearing plates, as shown in Figure 3.7.

### **3.7. Consolidated Drained Triaxial Tests Procedure**

The consolidated drained triaxial test (CD Test) is one of the most reliable techniques to fully characterize the mechanical properties of a rock. The scope of this testing campaign for the 3DP specimens is divided into two major elements: first, is to study the volumetric behavior (i.e. compressibility) of the sandstone analogues under various confining stresses up to 30 MPa effective stress, and find the influence of stress path on the peak strength and mode of failure of the material. Second, is to describe the failure mode of this material and relate the results with the Mohr-Coulomb and Hoek-Brown failure criterions.

The stress-strain relationship and the peak strength of the 3D printed sandstone analogues were determined using the axial force exerted by an ENERPAC L1608 Hydraulic Cylinder mounted on a steel frame. Pore pressure and Cell Pressure (i.e. Confining Stress) were applied by three TELEDYNE ISCO D-Series SFX 220 pumps. An Ametek Chandler QUIZIX QX Pump was used for accurately pumping the pore fluid through the body of the specimen, while the Pore ISCO pump was designed as a receiver. The exact configuration of both the Frame and the Pumps is shown in Figure 3.8.

For measuring axial and radial displacements during the drained triaxial tests, two types of linear variable displacement transducer (LVDT) systems were set up for each sample: two LVDTs (Measurement Specialties 250MHR-1502) for calculating axial displacement mounted on the top and bottom end caps of the specimen, these devices have a range of 12 mm and an accuracy of  $\pm 25.4 \mu\text{m}$  and one LVDT (Measurement Specialties 100MHR-3008) for calculating radial displacement with a range of 6 mm and an accuracy of  $\pm 25.4 \mu\text{m}$ . The exact configuration of the internal LVDT and the corresponding wiring is shown in Figure 3.9. Furthermore, as a confirmation reading, a Novo Technik TR 0100 external LVDT with a range of 100 mm and repeatability of  $\pm 2 \mu\text{m}$  was attached to the RAM and

mounted on top of the cell cap to estimate axial strain during compaction and shearing processes. Finally, an NMC 6500 triaxial pressure cell with a maximum operating pressure of 44.8 MPa (6500 psi), was used for these experiments.

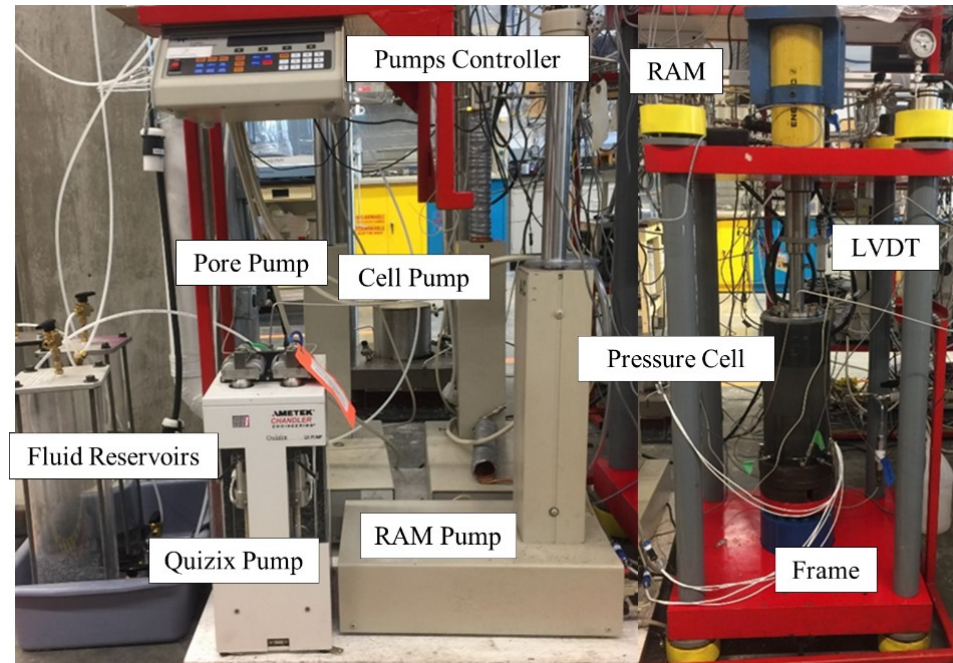


**Figure 3.8. Consolidated drained triaxial test equipment**

The measured data, which was composed by pore, cell and ram pump's volume and pressure, load cell data, differential pressure readings, ambient temperature, external LVDT measurements and axial and radial internal transducers data, was also recorded automatically by the GeoREF data logger software. The pressure and volume of the Quizix pump were recorded using Quizix PumpWorks™ software. To have a more comprehensive view of the overall setup used for the triaxial testing campaign, an explicit diagram is shown in Figure 3.10.

The analogues used in this testing campaign were indeed thermally cured in the oven (80°C) for 24 hours, right after the printing process was finished; furthermore, along the job, the heater system of the printer was turned on, so that the curing process of each layer

of binder deposited onto the printing job box was started at that very moment. The reason for choosing the stronger available version of the 3DP sandstone analogues was to test their mechanical behavior under high pressure conditions, like those encountered in natural oil/gas reservoirs. No specific confining stress or pore pressure conditions from any known reservoir were attempted to be replicated during this section of the project.

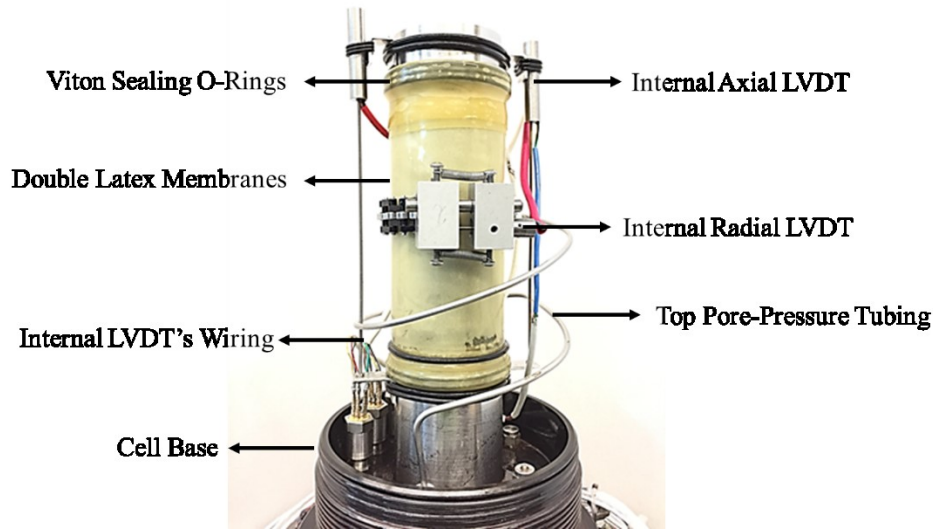


**Figure 3.9. Configuration of the Internal LVDT's for the Triaxial Testing Campaign**

To ensure a complete saturation of the specimens, they were submerged for a week in a sealed container full of silicone oil. Also, right before starting the triaxial test's set up, the analogues were placed into a vacuum chamber at an average pressure of -15 Psi (-0.1 MPa), so the high suction pressure created around the sample helped to drive the oil into the remaining empty pores and contributed to complete the imbibition process. Finally, after each specimen was placed inside the triaxial pressure cell, it was left for 24 hours under an effective confining stress of 1 MPa (resulting from a pore pressure of 2 MPa and a cell pressure of 3 MPa) for saturation purposes.

This process, together with the thermal curing previously mentioned, also ensures that the samples are isolated from surrounding atmosphere's humidity, so it could be assumed that

the pore media of each one of the specimens is free from any amount of water that could generate structural weakening or alterations in the volumetric measurements performed during the triaxial tests.

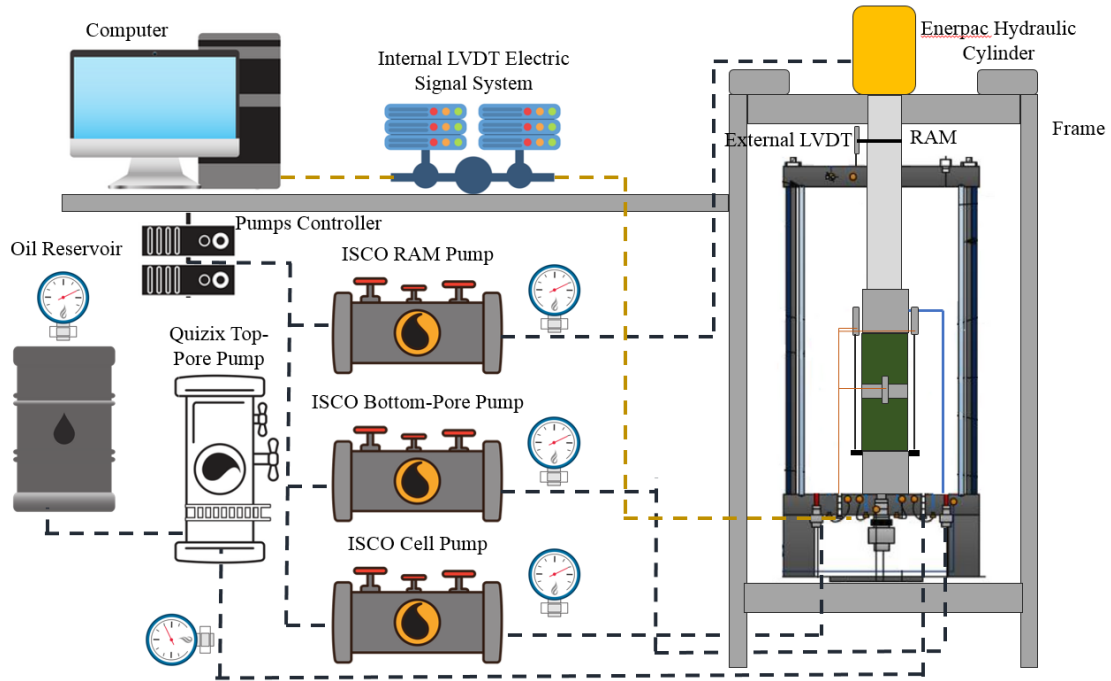


**Figure 3.10. Triaxial testing setup and data logging configuration for 3D printed specimens**

### *3.7.1. Consolidated Drained Triaxial Testing Campaign*

Compressibility Tests: 1 specimen of 63.5 mm in diameter by 127 mm in length (2.5” by 5”) were subjected to different cycles of loading and unloading to study the bulk volumetric behaviour of the 3D printed material. The cycles of loading-unloading were carried out as follows: after the initial saturation period, the confining stress was increased by steps of 1.5 MPa up to 8 MPa effective confining stress, then, it was increased to 12 MPa and finally was raised up constantly to 30 MPa by stages of 6 MPa. During the unloading cycle, the

specimen was taken back to its initial conditions by decreasing the confining stress in steps down to an effective confining pressure of 1 MPa.

Classic Consolidated Drained Triaxial tests: These were termed “classic” because the main goal was to study the influence of confining stress on the peak strength and mode of failure of the sandstone analogues. Also, from these results, the mechanical strength and failure behavior of the 3DP sandstone analogues were modelled using the linear the Mohr-Coulomb failure criterion. This process also allowed calculations of the drained strength parameters of this rock material. Three specimens of the same dimensions as the ones used for compressibility tests were tested under 10 MPa, 15 MPa and 25 MPa effective confining stresses.

## **4. Results from Uniaxial Compression Testing Program**

### **4.1. Introduction**

A uniaxial compression testing program was designed to study the influence of the printing parameters, and the manufacturing process itself, on the strength, elastic properties and failure mode of this material. Using a systematical variation of the three main building parameters: binder saturation, layer orientation and layer thickness, several groups of specimens with specific combinations of these three features were tested for failure under uniaxial conditions: variable binder saturation, constant layer orientation and thickness, variable layer orientation, constant binder saturation and layer thickness, variable layer thickness and constant binder saturation and layer thickness.

In general, binder saturation was proven to enhance the peak strength of the sandstone analogues, increasing this parameter from the base case (i.e. 10% Furan saturation) up to 20% saturation, results in an increase of 40% on the average peak UCS. Layer thickness, in contrast, was recognized to impact negatively the strength of the specimens, increasing the width of the building layers from base case (i.e. 250  $\mu\text{m}$ ) to 400  $\mu\text{m}$  decreased the average peak UC strength in 42.2%. Layer orientation demonstrated to induce heterogeneity on the peak strength and failure mode of the analogues.

### **4.2. Effect of Binder Saturation on the Mechanical Properties of the 3D printed sandstone analogues**

Three levels of binder saturation were studied for this part of the project, 10%, 15% and 20%. To verify the assumed influence of the layering process on the mechanical behavior of the sandstone analogues, every sample was printed horizontally (layers are aligned to the direction of the axial load during the UCS test) and tested after being left to cure at room conditions (i.e. temperature and humidity). To ensure there were enough data points to

analyze the repeatability of the results, five (5) samples of each saturation level were printed and tested under uniaxial conditions. The results are summarized in Table 4.4. One representative stress-strain curve and its corresponding predominant failure mode from each binder saturation level were included in Figure 4. to illustrate their behavior. The specimens built using a 10% saturation, layer orientation of 250  $\mu\text{m}$  and horizontally ubicated in the print-bed were chosen as the base case for comparison purposes.

As expected, there is a direct relationship between the binder saturation and peak strength of the samples, with 14.8 MPa being the average strength value of the base case (10% saturation) and 20.8 MPa being the average strength for the top binder saturation case (20% saturation), an increase of 10% in binder saturation implies an increment of 39.9% on the average peak strength of the analogues. These results are similar to the results found on plastic specimens within the study conducted by Vaezi & Chua (2011), who found that for a constant layer thickness, an increase in binder saturation level generated an enhanced material strength.

**Table 4.4. Summary of UCS Testing results for 3DP specimens built using various levels of Binder Saturations**

<b>Binder Saturation [%]</b>	<b>Layer Orientation (Thickness)</b>	<b>Average Peak UCS Stress [MPa]</b>	<b>Average Axial Strain at Peak [%]</b>	<b>Average Radial Strain at Peak [%]</b>	<b>Young's Modulus [GPa]</b>	<b>Poisson's Ratio</b>
<b>10%</b>	0° (250 $\mu\text{m}$ )	14.78	1.06	0.09	1.70	0.19
<b>15%</b>	0° (250 $\mu\text{m}$ )	18.02	1.20	0.12	1.78	0.20
<b>20%</b>	0° (250 $\mu\text{m}$ )	20.78	1.50	0.15	1.79	0.24

Starting from the valid assumption that every sample has the same packing ratio (i.e. the vibration frequency of the recoater for the sand deposition process was kept constant and there was no mechanical compaction applied to any batch of specimens), so the porosity is a sole function of the volume of binder used for building each specimen, this behavior is explained uniquely by the presence of a higher amount of crystallized Furan binder volume

in the grain contacts and pore space of the sample. This condition will certainly generate an increase in the bonding forces between grains, intensifying the ultimate shear strength of the sample.

Samples with 10% and 20% of binder saturation exhibited a clear brittle behavior after peak strength is reached, while the 15% specimens showed a softened decrease in strength with the further increase of strain after the peak, Figure 4. Even though a minor increase in the value of the Young's Modulus of the analogues is directly correlated with the increase of binder saturation, this parameter appears to remain almost unaffected by the presence of a higher volume of Furan in the pore space. The maximum variation encountered on this property is 5.2% between the extreme cases of the study.

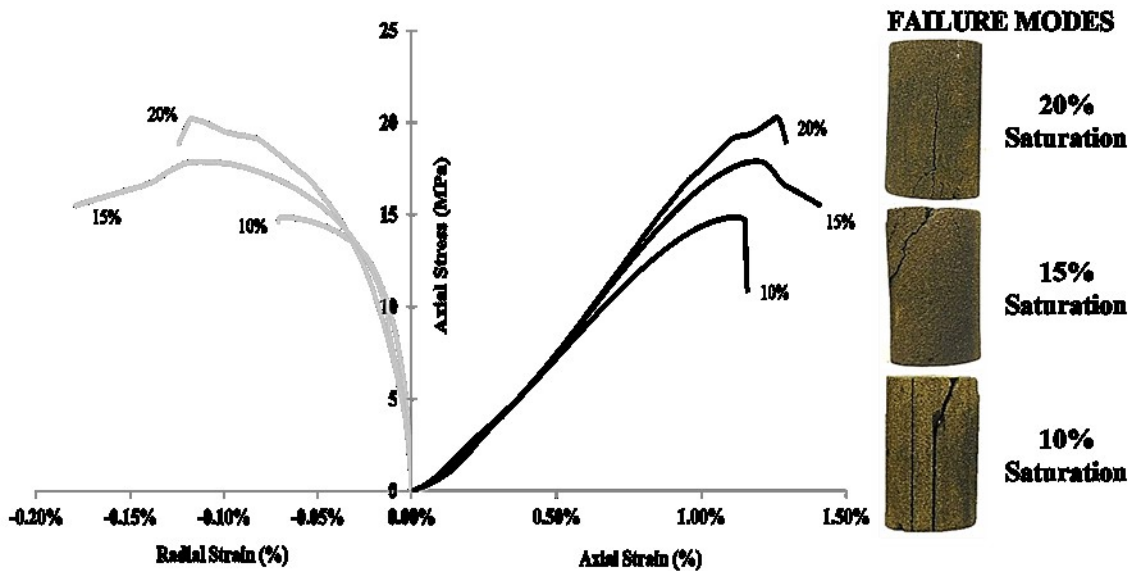


**Figure 4.1. Representative stress-strain relationship for the variation of binder saturation**

This behavior seems to correlate with the observation made by Bell et al. (1978), on the physical and mechanical properties of the Fell sandstones, where it's pointed out that there is no exact relationship between the higher presence of cementing material and the variation of the elastic properties of the specimens. Nonetheless, if the fact that an increase

in binder saturation generates a decrease in the porosity of the specimen is considered (porosity of 10% and 20% saturation specimens measured with Mercury Injection techniques was 47.6% and 35.7% respectively, Ardila et al. 2017), the slight increment in the Young's Modulus of the 3DP sandstones might be analogous to the behavior observed on Rotliegendes sandstone, on which the degree of cementation correlated directly with the value of the elastic moduli (Yale et al. 1995).

Regarding the mode of failure of the samples, Figure 4.1, for the group of 10% binder saturation specimens, the predominant mode of failure was a precise axial fracture (vertical splitting) coincident with the direction of the building layer's direction. This failure mode may suggest that the analogue was theoretically free of other microscopic discontinuities (Szwedzicki et al. 2007) and the cracking phenomenon was concentrated along the weakest zones of the specimen, in this case, the building planes. A complete summary of failure modes is included in Appendix A.

This phenomenon may suggest that the homogeneity of the 3D printed sandstone's pore structure is influenced by the manufacturing process. Similar to what it has been widely observed in slabbed or interbedded sedimentary rocks, the failure mode of the 3D printed sandstone analogues is influenced by the presence of planes of weakness, which in this case are coincident with the building surfaces. It is required that for further mechanical testing focused on the anisotropy of the mechanical properties of 3D printed materials induced by the printing methods, this point is taken into careful consideration (Roberson et al., 2015).

For the 15% binder saturation, three specimens had a well-defined failure plane at an average angle of  $60^\circ$  measured from the horizontal axis, which means that in terms of Mohr-Coulomb failure criterion, the material has an approximate friction angle of  $30^\circ$ . The rest of the samples exhibited a "neutral cone section" failure mode (V-shaped open fracture). This failure mode could suggest a highly-stressed shear area between the two macro-fracture zones, which were essentially formed by the interaction of micro-fractures which propagate and coalesce (Tang & Hudson, 2011). For 20% binder saturation, three of the samples failed at the V-shaped open fracture mode and the rest exhibited tensile axial fractures parallel to the load application direction.

The consistency of the results obtained for the peak UC strength of the 3D printed sandstone analogues is notable. For the case of 10%-saturation specimens, the range of data is 0.44 MPa with a CV of 0.32, for the 15%-saturation specimens', the mean UC strength spans within 1.23 MPa and has a CV of 0.60. Finally, for the case of 20%-saturation specimens, the range of the average UC Strength is 0.71 and it has a CV of 0.35. The variations on the values of the peak strength obtained from the UCS tests performed on the 3D printed sandstone analogues can be considered promising when comparing them with similar studies performed in some homogeneous natural sandstones: Pennsylvania sandstone has a reported UCS of 104-129 MPa, which results in a range of 25 MPa (Fakhimi & Hemami, 2015); uniform materials as Indiana and Berea Sandstones have CV related to its UC strength of 12 and 4.2 respectively, from studies conducted over 50 specimens (Ruffolo & Shakoor, 2009).

#### **4.3. Effect of Layer Orientation on the Mechanical Properties of the 3D printed sandstone analogues**

As it was previously explained in the previous chapter, to analyze the repercussion of this parameter in the peak strength and failure mode of the 3DP analogues, separate groups of 4 to 5 specimens were printed with 0°, 25°, 45°, 65° and 90° inclination measured with respect to the axial load application direction or Z Axis (Axial Load direction). The results are summarized in Table 4.5 and a representative stress-strain behavior for each one of the layer orientation configuration is presented in Figure 4.2.

The strongest layer configuration corresponds to that of 90° orientation. In this case, the axial load and the direction of the building planes are perpendiculars, therefore the forces are not directly applied along the building layers and the ultimate strength is increased to a value of 17.10 MPa. The average Young's Modulus for this group of samples is 1.68 GPa. The strength of the 90° specimens is 13.56% higher than the weakest case (0°-inclined samples), which have an average peak stress of 14.78 MPa.

**Table 4.5. Summary of UCS testing results for 3DP specimens built using various layer orientations**

Binder Saturation [%]	Layer Orientation (Thickness $\mu\text{m}$ )	Average Peak Stress [MPa]	Average Axial Strain at Peak [%]	Average Radial Strain at Peak [%]	Young's Modulus [GPa]	Poisson's Ratio
10%	0° (250)	14.78	1.06	0.09	1.70	0.19
10%	25° (250)	15.53	0.96	0.05	1.90	0.19
10%	45° (250)	15.37	1.05	0.06	1.93	0.19
10%	65° (250)	14.87	1.05	0.05	1.59	0.25
10%	90° (250)	17.10	1.19	0.18	1.68	0.25

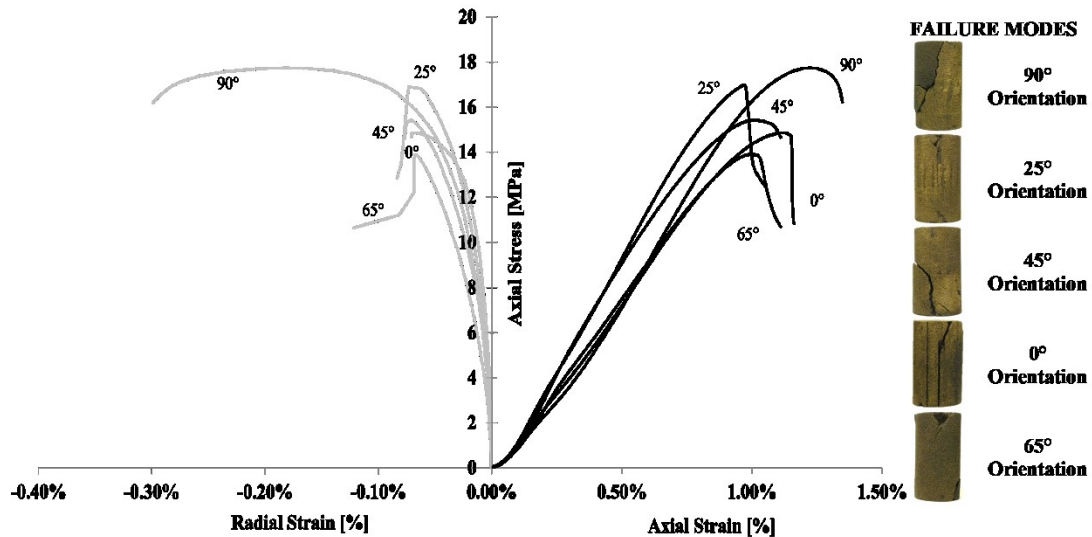


**Figure 4.2. Representative Stress-Strain Relationship for the variation of Layer Orientation**

From the stress-strain plots presented in Figure 4.2, it can be observed that the samples behave in a linear elastic manner until around 70% of the UCS peak strength. The tangent Young's Modulus ( $E$ , GPa) and Poisson's Ratio ( $\nu$ ) of the specimens were calculated from this assumed elastic zone at 50% of the peak UC stress, as indicated by the standards of the ASTM D7012-14, 2004. The 90°-orientation specimens sustained relatively higher axial and radial strains (around 1.18% and 0.2% respectively) compared with the rest of the groups (which tolerated an average of 1.04% axial strain and 0.1% radial strain). This

behavior was potentially generated by the fact that part of the axial stress sustained by the specimens was spent in the closure of the horizontal building planes. In general, the amount of radial strain at failure conditions was small, this probably due to the progressive particle rearrangement and movement of the grains into surrounding pores allowed by the high porosity of the material.

The anisotropic behavior of the peak strength of a rock with the variation on the orientation of the bedding planes is also observed in natural interbedded sandstones. As it was pointed out by Hu et al., (2017), the characteristics of the shear deformation of the bedding planes (building planes, in the case of the 3D printed analogues), directly impacts the strain behavior of the specimen and ultimately its peak strength. This can be evidenced by the fact that the cylinders built using oblique layer orientation angles, sustained a lower average axial strain before failure occurred. One aspect that is worth to highlight is that in contrast to the observations made by Hu et al., 2017 in natural interbedded sandstones, the compressive strength anisotropy ratio ( $k_1 = (\sigma_1 - \sigma_3)_0 / (\sigma_1 - \sigma_3)_{90}$ ) of the 3D printed sandstone analogues ( $k_1 = 0.86$ ), indicates an anisotropic behavior of the strength between the two principal structural axes. This behavior might be solely attributed to the influence of the building process on the strength and failure mode of the 0°-orientation set of specimens.

Regarding failure mode of the rest of the configurations, 45°-inclined samples failed to exhibit shear planes inclined within a range of 45° to 60°, which was also the preferential mode of a failure mode for 90°-inclined samples. 25° and 65° samples exhibited axial cracking and V-shaped fracture modes, not suitable for being modelled under the theory of Mohr-Coulomb failure criterion. The complete set of specimen's failure mode will be also included in Appendix A.

Variations in the inclination angles at which they are manufactured induce indeed differences in their mechanical properties and failure modes, Figure 4.2. As it was previously pointed out by Farzadi et al., (2014), the mechanical behavior of 3D printed analogues is highly reliant on the orientation of the powder spreading and the direction at which compressive load was applied (i.e. parallel, perpendicular or inclined with respect to the layering orientation). The previous results allow deducing that, for instance, in

further applications of AM Technology on geomechanical experimental campaigns, 0°-inclined samples should be treated judiciously, and their mechanical properties should be inspected at different layer orientation-load application combinations, so there's no possible impact of the printing process on the results.

The consistency of the peak UC stress results is shown in Figure 4.3-a. Each cluster of sandstone analogues were also evaluated using a descriptive statistical analysis. The set that exhibited the lower variability was the 0°-orientation specimens with a range of 0.44 MPa and a CV of 0.32. The rest of the clusters exhibited a considerably higher CV: 25°-orientation specimens had a CV of 1.29, 45°-orientation had a CV of 0.95 and both 65°-orientation and 90°-orientation specimens had a CV of 1.1.

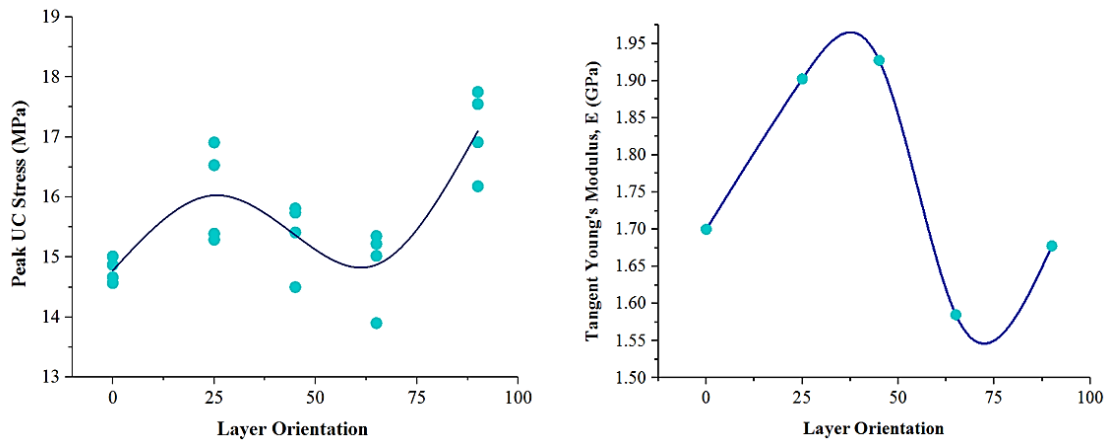


**Figure 4.3. The consistency of the UC Strength results of the 3D Printed Sandstone Analogues. (b). Variation of the Tangent Young's Modulus with the Building Layer Orientation**

The solid curved line included in Figure 4.3-a, which is theoretically defined as the anisotropy of the 3D printed sandstones, represents the average values of peak UC stress for each set of specimens. Disregarding the influence of the manufacturing process on the strength and failure mode of the 0°-orientation specimens, the anisotropy of this material can be catalogued as a U type. This is evidenced by the progressive decrease of the peak UC strength on the groups of analogues built using slanting planes. As the inclination angle

of the sand planes used to build the specimens departs from the  $0^\circ$ -orientation, failure mechanism starts to be dominated by the sliding along bedding planes (i.e. building planes for 3D printed analogues), in other words, shearing occurs along planes situated at an oblique angle to the direction of maximum compression (Axial load direction). When the orientation of the building planes approach to the  $90^\circ$ -orientation, the influence of the shear-dominated rupture mode starts to fade, and the specimen's failure is materialized in a singular axial splitting type of failure that occurs across the matrix of the rock.

With respect to anisotropy on the value of the tangent Young's Modulus ( $E$ ) of the 3D printed analogues, Figure 4.3-b, the maximum reported value corresponds to that exhibited by the  $45^\circ$ -orientation set of analogues. If the layer orientation angle ( $\beta$ ) is normalized by the angle of the fracture plane materialized during the sample failure ( $\alpha=45-\phi/2$ ; which for the case of the 3D printed analogues, whose  $\phi=30^\circ$ ; is equal to  $30^\circ$ ), the highest value of the Young's Modulus corresponds to those specimens whose lamination planes are closer to the direction of the maximum generated shear stress modified by the friction angle (Attewell & Sandford, 1974): the  $45^\circ$ -orientation specimens.

To fully understand the influence of the binder spreading direction on the failure mode of the 3DP sandstone analogues, two groups of 4 samples were printed both parallel and perpendicularly to the direction of binder dispersion. As observed in Figure 4.4, the specimens printed parallel to this orientation failed with an axial crack coincident with one of the building planes. This behavior can be explained by the fact that in these orientations, the binder necks (union between two contiguous grains) and the resulting porosity of the specimen are aligned with the compression direction. During the UCS test, the binder necks will directly withstand the applied load, but the bounding process in the perpendicular direction will not be as strong, generating failure along the surface of the planes.

In contrast with this outcome, the analogues manufactured perpendicularly to the binder spreading direction failed at different manners to that of a clearly printing process-influenced one. The differences in the tone of the specimens on this figure are only attributed to the color saturation of the camera during the time of the image taking.

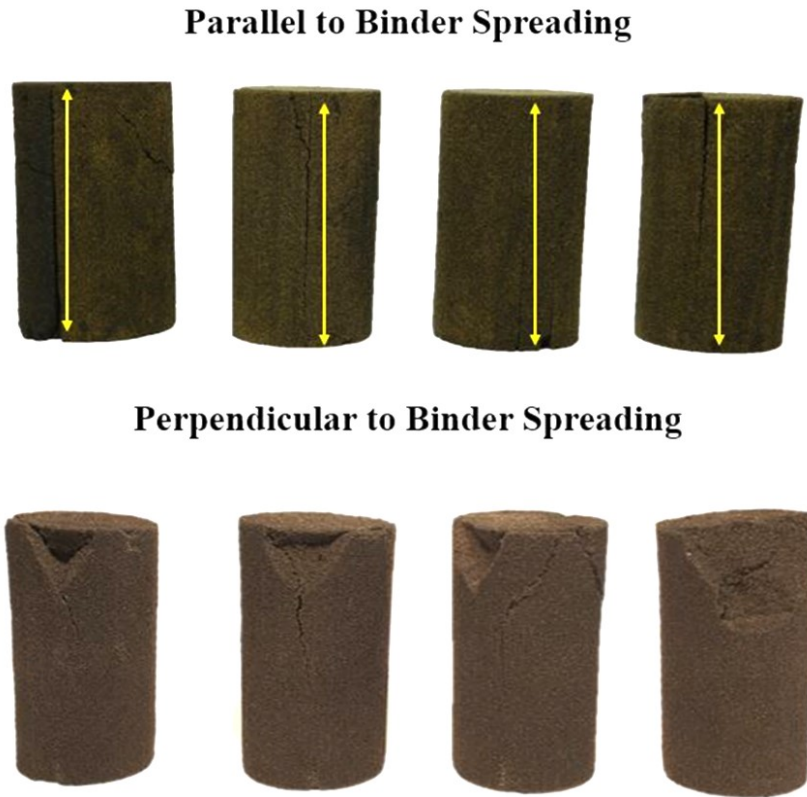


**Figure 4.4. Influence of Binder Spreading Direction on the Failure Mode of the 3D specimens**

#### **4.4. Effect of Layer Thickness on the Mechanical Properties of the 3D printed sandstone analogues**

To solely study the influence of the layer thickness on the strength and stiffness of the 3D printed analogues, there were two cases chosen: 250  $\mu\text{m}$  (Base case) and 400  $\mu\text{m}$ , while maintaining a constant saturation of 10% and a  $0^\circ$ -orientation for each specimen. This with the purpose of comparing the strength and failure mode with the base case. For the case of this section, a single sample of 38.1 mm in diameter by 76.2 mm in length (1.5" by 3") takes a total of 153 layers of 400  $\mu\text{m}$  to be completely built, which is translated into half of the time required to manufacture a specimen at a layer thickness of 250  $\mu\text{m}$ , due to the higher volume of sand deposited in each recoater pass.

A summary of the results obtained for this section is presented in Table 4.6. A representative stress-strain relationship for each one of the printing configurations is shown in Figure 4.5. There is an indirect relationship between the sand layer thickness of the specimens and their ultimate UC strength (i.e. as the thickness increases, the peak UCS value of the sample is reduced). This behavior could be generated by a bilateral relationship between the binder saturation and the width of each individual building plane (Farzadi et al. 2014). Under normal conditions (during a common printing job), it was observed that the vertical spreading of Furan binder would be less than that produced laterally. In such circumstances, in the case of an increased layer thickness is selected to be used in the manufacturing process of the sandstone analogues, the vertical penetration would not be positive throughout the entire layer, generating incomplete binder spreading, compromising the integrity of the lesser binder-saturated zones of the cylinder and reducing its overall peak strength (Vaezi & Chua, 2011).

**Table 4.6. Summary of UCS Testing results for 3DP specimens built using various Layer Thicknesses**

<b>Binder Saturation [%]</b>	<b>Layer Orientation (Thickness, <math>\mu\text{m}</math>)</b>	<b>Average Peak Stress [MPa]</b>	<b>Average Axial Strain at Peak [%]</b>	<b>Average Radial Strain at Peak [%]</b>	<b>Young's Modulus [GPa]</b>	<b>Poisson's Ratio</b>
10%	<b>0° (250)</b>	14.78	1.06	0.09	1.70	0.19
10%	<b>0° (400)</b>	8.55	0.94	0.07	1.23	0.23

Even though the binder drop volume is adjusted by the system to maintain a constant Furan saturation, the increase in the thickness of each building layer generates a non-uniform distribution of the resin across each plane, which could be possibly critical along the vertical direction. Establishing a direct comparison, a horizontal sample printed using a layer thickness of 250  $\mu\text{m}$  has an average strength of 14.8 MPa while an equivalent cylinder printed using a layer thickness of 400  $\mu\text{m}$  has an average peak UCS of 8.6 MPa which is 42.2% lower than the peak UC stress of the base case. Furthermore, the specimens printed

under the wider building plane case exhibited a reduction in the tangent Young's Modulus of about 28% when compared with the 250  $\mu\text{m}$  cluster.

Figure 4.5 shows the generalized stress-strain behavior of both sets of specimens. It can be observed that the group built using a thicker building layer exhibited a softened behavior at peak conditions in comparison to the ones built using a layer of 250  $\mu\text{m}$  at the same conditions. In addition, the generalized failure mode of the sandstone analogues was not as brittle as the base cases. In contrast, the specimens from the second cluster failed preferentially in a V-shaped, non-abrupt mode. The fact that this V-shaped failure mode was the predominant rupture process undergone by the 400  $\mu\text{m}$ 's set of specimens illustrates that even though there could be an ununiform binder distribution across the sample, the homogeneity of the material is not compromised and the possibility of considering any influence of building-process-features on the mechanical behavior of the analogues could be suppressed.

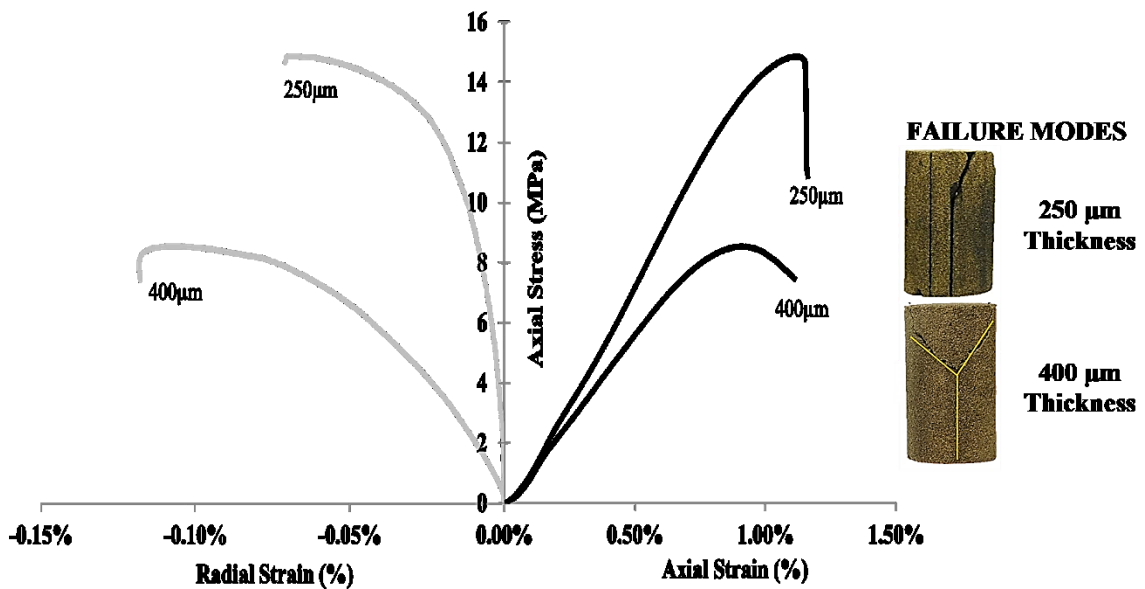


**Figure 4.5. Representative Stress-Strain Relationship for the variation of Layer Thicknesses**

#### **4.5. Effect of High-Temperature Curing Process on the Mechanical Properties of the 3D printed sandstone analogues**

UCS tests performed on samples heated to 80°C and printed with the same printing settings of those shown in this work (10% binder saturation, 250 µm and 90°-layer inclination angle), exhibited an average peak UCS strength of around 22 MPa, which represents an increase of 29.4%. This value is increased even more when the heating process is initiated during the printing job by turning on the heater device of the recoater assembly.

A similar thermal strengthening behavior to the one exhibited by the sandstone analogues was also pointed out by Zhou et al. (2014) during the experiments conducted using calcium scaffolds. The mechanical strength and stiffness of the calcium bone scaffolds analyzed in that study got benefitted from the application of a 200°C heat treatment, which essentially promoted the dehydration of the CaSO<sub>4</sub>, enlarging the plastic deformation region of the scaffolds under a compressive load and ultimately their compressive strength. Another key point made by the author was that increasing the treatment temperature from 200°C to 250°C generated negative effects on the strength of the scaffolds due to organic decomposition. Similarly, 3DP sandstone analogues treated at temperatures higher than 80°C exhibited a downward trend on the peak compressive strength, attributed to a degradation process of the Furan binder.

#### **4.6. Closing remarks about influence of Printing configurations on the mechanical properties of 3D printed sandstone analogues**

Throughout this study, it has been confirmed that the use of Furan Binder jetting with silica sand powder technique, improves by orders of magnitude various important mechanical and elastic properties (i.e. UCS Peak Strength, Young's Modulus and Poisson's Ratio), in comparison with previous efforts performed with other types of materials (i.e. plastic, metal powders and polymers). Nonetheless, some of these mechanical and constitutive properties were found to be lower than the values encountered for natural sandstones.

Different printing configurations and features were tested to verify their influence on the mechanical properties of the specimens. The first one is the layer inclination angle, for which 0°, 25°, 45°, 65° and 90° inclined printing layers measured from the axial applied load direction were used to build identical sandstone specimens. The highest average Peak UCS Strength (17.10 MPa) was obtained on 90° inclined samples, whereas the weakest group of samples was provided by the 0° inclined angles (14.78 MPa). Regarding the mode of failure of the samples, 0°, 25° and 65° exhibited a predominant axial splitting, while 45° and 90° failed in a well-defined inclined plane of about 60° of inclination. On the other hand, it was found that 0° inclined samples undergo a noticeable influence of the printing process on the mode of failure and presumably on their average peak strength.

The influence of Furan binder saturation on the mechanical properties of the 3D printed specimens was studied using three different saturation values (10%, 15% and 20%), keeping the same layer orientation and thickness, while the repercussion of printing layer thickness was studied using two thicknesses (250 µm and 400 µm), while maintaining a constant binder saturation and layer orientation. To summarize these sections, it can be concluded that the higher the binder saturation, the stronger the sandstone analogue, while the higher the layer thickness, the weaker the specimen. This behavior is directly related to the volume and distribution of Furan binder inside the pore space of the samples, respectively.

## **5. Results from Tension Testing Program**

### **5.1. Introduction**

The importance of determining the tensile capacity of a rock or a rock mass relies on the control that this property exerts on many failure processes. Many authors have pointed out previously that the fracture initiation process (i.e. Crack initiation) in brittle materials, such as most of the reservoir rocks in the oilfield, is a tensile phenomenon (Griffith, 1921 and Haimson & Cornet, 2003), therefore tensile strength is a fundamental property to study the resistance to failure of a rock material (Perras & Diederich, 2014).

Despite this, tensile strength experiments are rarely carried out in engineering practice due to the difficulties in preparing the specimens and obtaining reliable and valid results (Cai et al. 2010). Precisely, this is one of the fundamental issues that could be solved by fabricating rock analogues using 3D printing technology. The fact that this technology allows the reproduction of numerous equivalent specimens, the usage of rock analogues will let the user have the possibility of obtaining repeatable results and discard the data from those tests that were considered invalid (i.e. did not fail along the expected zones or had appreciable influence from the loading device). Furthermore, direct tension tests will not be problematic to run because it will only require an STL (Stereolithography) file with the desired 3D-shape and dimensions of the specimens and the printer will fabricate as many samples as required.

To determine the tensile strength of the 3DP sandstone analogues, two types of test were performed: Brazilian (indirect tension) test and direct tension test. The standard methods used as guidance for either fabricating the specimens and interpret the results were ASTM (2008b) D3967-08, 2008 for indirect tension and ASTM (208a) D2936-08, 2016 for direct tension. Direct tension test showed a lower tensile strength compared to the indirect tension tests. Also, it was observed that the building process influenced the mode of failure of the specimens (i.e. rupture through a building plane), similar to the UCS tests.

## 5.2. Brazilian Tension Test Results

To calculate the tensile strength of the 3DP sandstone analogues, 5 Brazilian Test specimens of a theoretical diameter of 54 mm and a thickness of 22 mm were printed horizontally (0°-layer orientation), at a binder saturation of 10% and a layer thickness of 250µm. There is no expected influence of the printing configurations on the failure mode of the specimens due to the single-point application of the compressive stress.

The analogues used for this testing campaign were also left in a sealed container at atmospheric conditions during one week before starting the test. During the tests, the analogues were loaded until failure using a strain rate of 0.17 mm/min, aiming a time to failure between 5-15 minutes, as suggested by ASTM (2008b) D3967-08.

A summary of the results obtained from this testing campaign is presented in Table 5.. The calculations of the splitting tensile strength were performed using the standard formulation suggested by the ASTM, Equation 5.1:

$$\sigma_t = \frac{2P}{\pi LD} \quad \text{Equation 5.1.}$$

where P is the maximum applied load, L is the thickness of the specimen and D its diameter. The average tensile strength obtained out of the 5 samples tested was 3.52 MPa, with a standard deviation of 0.39 and a CV (95%) of 0.49%.

Given the small inter-variability of the results represented by these statistics, it is possible to assure that the resulting tensile strength of this material is valid from the ASTM designations (suggested CV < 5%). With respect to the time to failure, there is a higher variability generated by the BT-2, which failed at almost twice the average value.

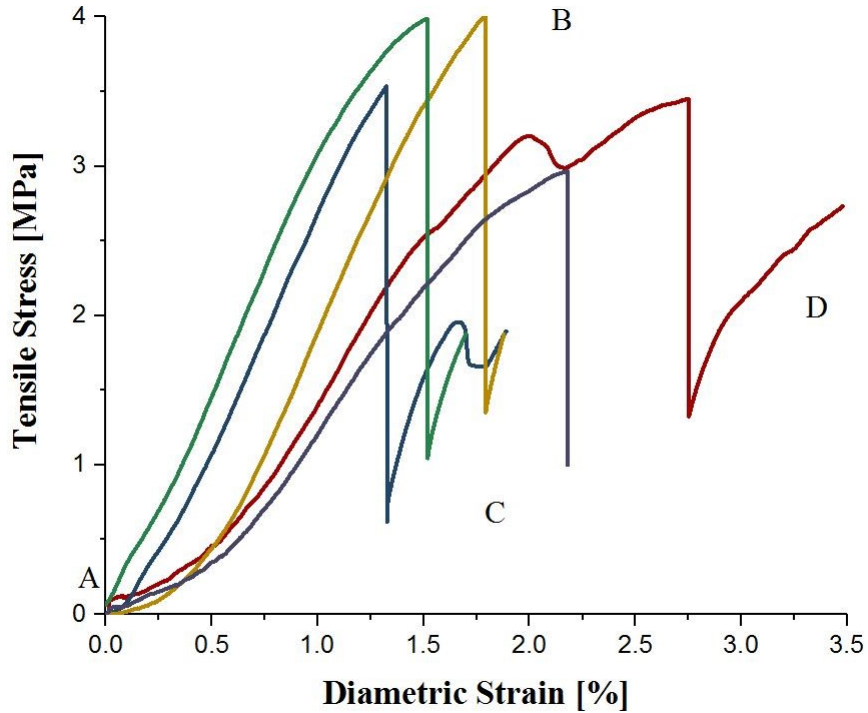


**Figure 5.1. Tensile stress vs. diametric strain for 3DP sandstone analogues**

The detailed relationship between tensile stress [MPa] and diametric strain [%] is presented in Figure 5.1. As it would be observed in this figure, 3/5 of the specimens failed at a similar diametric strain, around 1.5-2.0%, while specimen BT-2, as it took a longer period to break, failed at a diametric strain of 2.75%.

Analyzing closely the plots from the tests, there are three identifiable zones: segment A-B corresponds to the elastic behavior of the specimen as an intact material, this segment ends when the applied load is high enough to reach the crack initiation stress. Segment B-C corresponds to the unstable crack propagation, is characterized by a continuous decrease in the load until the crack propagation has become a stable process. In segment C-D, the load starts to increase again for the diametric crack to propagate further. With further increments of the load, the adjacent regions to the cracking zones start to crush and secondary fractures are developed. Generally, the tests are stopped until these three stages are identifiable (Guo et al. 1993).

A representative image of the previously described failure mode of the Brazilian specimens is shown in Figure 5.2. The main diametric crack is easily identifiable and there is no appreciable influence from the end-caps on the disks.

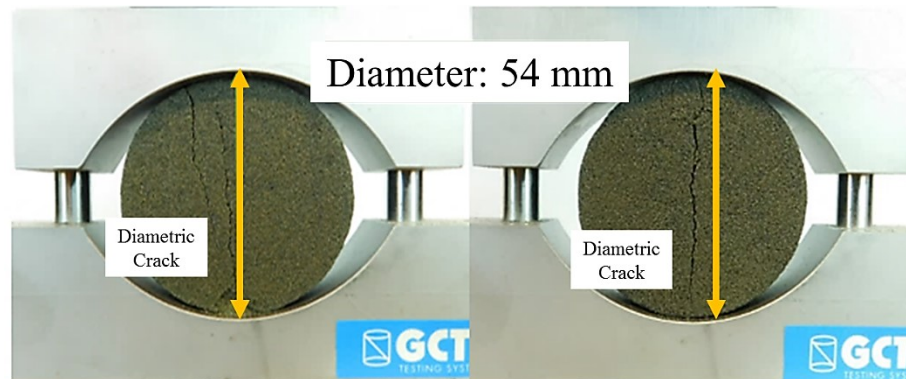


**Figure 5.2. Generalized Failure Mode for Brazilian Testing on 3D Printed specimens**

When comparing the results of this tests with natural rocks, Berea Sandstone's average tensile strength is 3.85 MPa, which is just 9.4% higher than the 3DP analogue. By comparing only this property, researchers might think that 3D printing technology is in a privileged stage in the race for reproducing the mechanical properties of real rocks (Table 5.1). Nonetheless, the average uniaxial compressive strength of Berea Sandstone is around 62 MPa, so the ratio between tensile and compressive strengths ( $\sigma_c / \sigma_t$ ) is around 15, for the case of the 3DP specimen, this ratio is around 5. Considering that for natural materials  $\sigma_c / \sigma_t$  is normally around 16-27 (Sheorey et al. 1989, Hoek. 2000 and Cai et al. 2010), the manufactured rock specimens have, in the best scenario, a 3 times higher tensile strength for a material with a uniaxial compressive strength of 14.8 MPa.

However, the calculation of the Strength Ratio ( $R = \sigma_t / \sigma_c = \sigma_{ci} / 8$ ) in porous rocks is highly influenced by different parameters such as grain size, discontinuities or pre-existing defects, material peak strength and mineral content. Based on Griffith's Theory, on which for a compressive stress field, the peak strength,  $\sigma_c$ , is equivalent to the crack initiation stress,  $\sigma_{ci}$ , R will have a value of 8. Nonetheless, it has been confirmed by experimental

data that this assumption does not hold true for natural materials, and the ratio  $\sigma_c / \sigma_{ci}$  ranges from 0.3-0.4 for coarse-grained materials (conglomerates and sandstones) and from 0.5-0.6 for fine-grained materials (shales, siltstones and mudstones).

**Table 5.1. Brazilian Test Results on 3D Printed Sandstone Analogues**

Sample ID	Peak Tensile Strength [MPa]	Time to Failure [min]
BT-1	2.95	5.5
BT-2	3.43	11
BT-3	3.45	5.8
BT-4	3.92	5.4
BT-5	3.87	5.6
<b>Average Results</b>	<b>3.52</b>	<b>6.7</b>

Analyzing a single pore on a weak/porous and fine-grained rock under tensile and compressive conditions (Figure 5.3), according to Kirsch's Solution, theoretically, for a material without defects, the maximum tensile stress at any point within the boundary of a circular pore is three times the applied load. Therefore, tensile fractures will be generated if the applied load is equal to 1/3 of the tensile strength ( $\sigma_t$ ). Under compressive conditions, the tensile fractures parallel to  $\sigma_1$  will be generated at an applied stress of  $-(\sigma_t)$ . Hence, the ratio of compressive stress to tensile stress at crack initiation is 3 and a Strength Ratio R could be defined as  $R=3 \sigma_c / \sigma_{ci}$ .

Considering the  $\sigma_c / \sigma_{ci}$  ratio exposed previously for this kind of highly porous rocks (0.3 to 0.6), R will range from 5 to 10, a lower value compared to the original range of 16-27 proposed by other researchers. This phenomenon, in highly porous rocks ( $\phi > 20\%$ ) as is the case of the 3D printed specimens (porosity of 46.7% for 10% binder saturation specimens or 35.7% for 20% binder saturation specimens), could be explained by the influence of pores as stress concentrators, they will play the role of pre-existing defects for the crack initiation and crack growth stages of the stress-strain behavior, generating a variation on the fracture mechanism from that of stronger rocks (Cai et al. 2010).

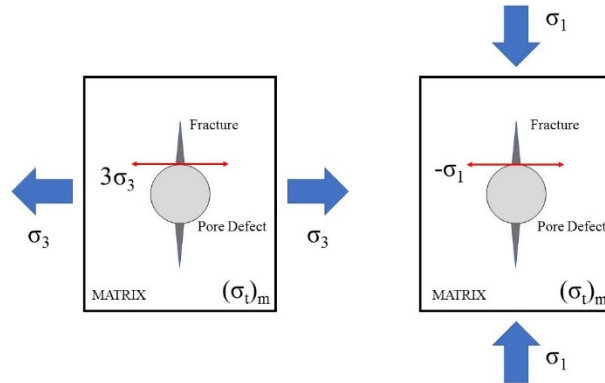


**Figure 5.3. Crack initiation from circular pore boundary in tension and compression (after Cai et al. 2010)**

### 5.3. Direct Tension Test Results

As discussed previously, to perform the direct tension tests, a compression-to-tension load converter (CTC) (Fuenkajorn & Klanphumeesri. 2011), is used to convert the applied compressive load from a conventional compression machine into pure tension along the body of the specimen. The load was transmitted by an ELE 50kN load frame at an axial displacement rate of 0.05 mm/min, aiming a time to failure of 5 to 15 minutes. The standard operation procedure used to conduct this testing campaign was ASTM D2936-08.

A comprehensive summary of the results obtained from this testing campaign is presented in Table 5.2. The calculations of the splitting tensile strength were performed using the standard formulation suggested by the ASTM, Equation 5.2:

$$\sigma_t = \frac{P}{A_t}$$

**Equation 5.2.**

In the previous expression,  $P$  is the maximum applied load at which tensile failure was induced and  $A_t$  is the transversal area of the body of the specimen along which most of the deformation, caused by the stress at which the sample is subjected, is generated. A total of 14 specimens were printed, 10 of them horizontally ( $0^\circ$ -layer orientation), from which at the same time, 7 of them were printed parallel to the direction of binder spreading and the other 3 perpendiculars to this direction; and 4 vertically ( $90^\circ$ -layer orientation), at a binder saturation of 10% and a layer thickness of  $250\mu\text{m}$  (Table 5.2). Analogues used for this testing campaign were also left in a sealed container at atmospheric conditions during one week before starting the test. The relationship between Axial Tensile Stress and Axial Strain for both groups of analogues are presented in Figure 5.4 and Figure 5.5.

**Table 5.2. Summary of Direct Tension Test Results on 3D Printed Sandstone Analogues**

<b>Sample ID</b>	<b>Number of Specimens</b>	<b>Peak Tensile Strength [MPa]</b>	<b>Time to Failure [min]</b>
<b>0-Deg Inclined (Parallel Binding)</b>	7	1.36	4.32
<b>0-Deg Inclined (Parallel Binding)</b>	3	1.25	11.6
<b>90-Deg Inclined</b>	4	0.64	9.03

An average tensile strength of 1.30 MPa for the  $0^\circ$ -oriented specimens and of 0.86 MPa for the  $90^\circ$ -oriented specimens, with coefficients of variation (CV) of 0.24 and 0.14 respectively, were obtained for the entire number of direct tension tests run on this section. As it would be expected, the stress-strain curves exhibit a continuous increase on the applied load while the specimen still behaves as an intact material, when the tensile stress reaches the critical point at which equalizes the tensile strength of the sandstone analogue, a sudden drop in the load indicates the specimen's failure.

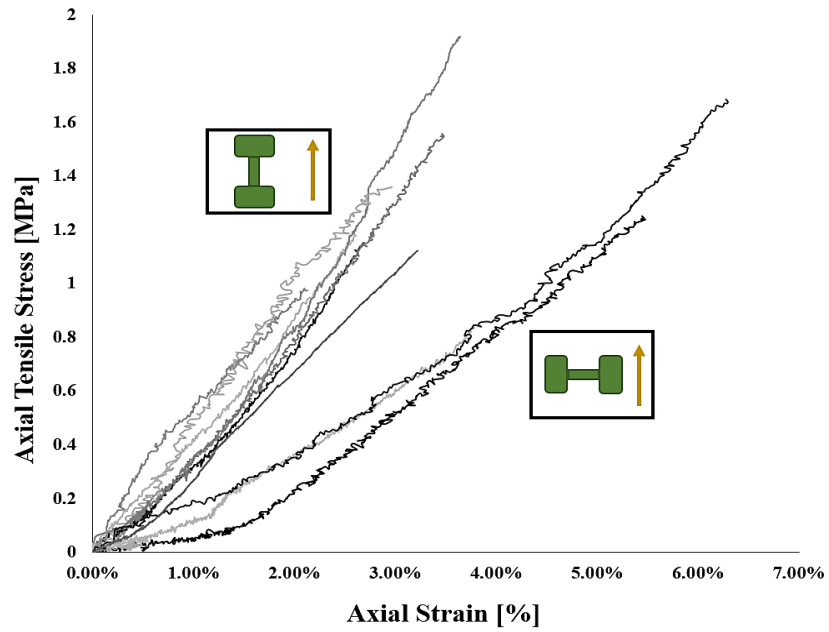


**Figure 5.4. Axial tensile stress vs. axial strain for 3DP specimens printed at 0°-layer orientation**

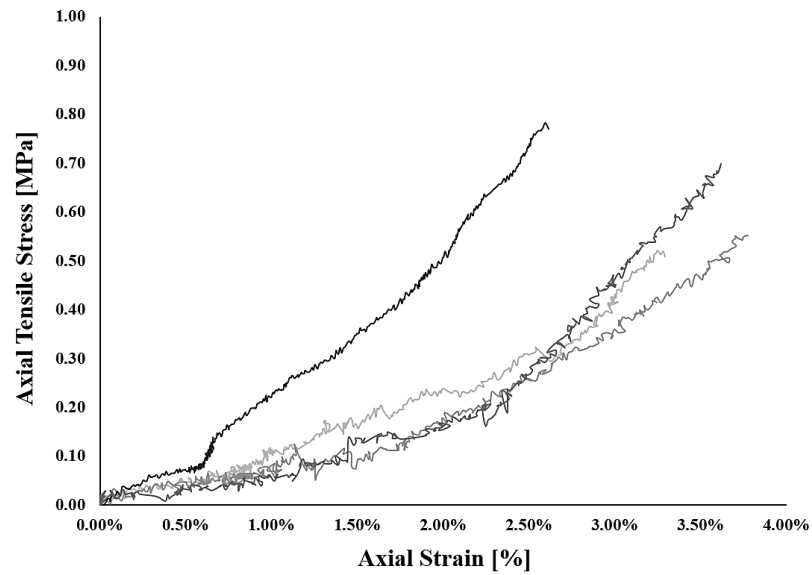


**Figure 5.5. Axial tensile stress vs. axial strain for 3DP specimens printed at 90°-layer orientation**

Comparing the tensile strength obtained for each population of specimens with the UCS for specimens built using the same printing features, there is an R ratio ( $R=\sigma_c/\sigma_t$ ) of 11.7 for the 0°-oriented analogues and 23.1 for the 90°-oriented ones. In addition, comparing these results with the statistical relationships developed by (Pul et al. 2008) which suggest that the ratio between direct and indirect (i.e. Brazilian) tensile strength has been found to be around 0.78, the 3D printing specimens exhibited a lower relationship of 0.18 for the 90°-oriented case and of 0.37 for the 0°-oriented case.

Regarding the stress-strain behavior exhibited by the direct tension specimens, there is a remarkable difference between the ones printed parallel to the binder's spreading direction and the ones printed perpendicular to it. The specimens printed along with this direction, even though they were also printed along the x-y plane (i.e. same binder spreading orientation), failed at a lower axial strain than the ones printed perpendicular to the binder spreading. This phenomenon could be attributed to the distribution of the binding material inside the pore structure of the specimens.

As pointed out by Farzadi et al. (2014), both powders spreading and binder jetting directions have an influence on the mechanical behavior of the specimens. As it was pointed out in the previous chapter, in both cases, the relative direction at which the binder is sprayed over the layer of silica sand will determine the preferential orientation of the binder necks and resulting pores. The axial strains at peak for the specimens printed parallel to the binder spreading lie within 2.2% -3.2%, while for the analogues printed perpendicularly to this direction, axial strain at peak was observed to be in the range of 5.5% -7%. Based on this, it can be concluded that the specimens printed perpendicularly to the binder spreading can withstand more strain before failing because they are oriented at 90° from the tensile strength action.

The 90°-oriented specimens (i.e. placed vertically on the printing job box) failed at a lower average tensile strength, around 49% of the 0°-oriented analogues. Nonetheless, according to the failure mode observed after the entire testing campaign performed on this groups of specimens, it seems to be that similar to the 0°-oriented UCS specimens, the printing process had an influence on their mechanical behavior. As shown in Figure 5.6, the dog-

bone specimens cracked along a perfect building plane, which could be acting as a plane of weakness and might have an impact on the final tensile strength.

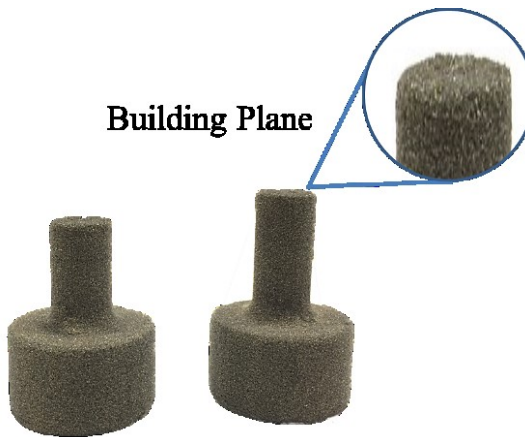


**Figure 5.6. Failure mode of 90°-oriented analogues under Direct Tension**

#### **5.4. Relationship between Brazilian Tensile Strength and Direct Tensile Strength**

The determination of the Brazilian tensile strength in rocks is highly reliant in the optimum load transfer to the rock specimen, such that the tensile stresses are mainly developed in the middle section of the disk and the stress concentration and crushing phenomena on the edges of the sample are minimized. Multiple methods have been developed to overcome these inconvenient, such as using flat loading platens, flat platens with cushions, loading platens with small-diameter rods and curved loading jaws (ISRM, 1978). This last one being the method used for this experimental campaign.

Nonetheless, the sensitivity of the developed tensile stresses to the angular width of the normalized applied stress is a parameter to take into consideration. The lower the angular width, the lower the calculated tensile strength. This reason and the tendency of the Brazilian specimens to be crushed at the ends could generate a considerably higher value of tensile strength than the one determined using the direct tension test.

Even though there is a large degree of scattering in the relationships between the direct tensile strength (DTS) and Brazilian (indirect) tensile strength (BTS), some authors (Perras & Diederichs, 2014) have determined that  $f_{DTS} = f_{BTS}$  is about 0.7 for sedimentary rocks. For the case of the 3D printed sandstone analogues, this relationship is equivalent to  $DTS = 0.37 BTS$ . Further research work on a denser specimen population is needed to analyze both modes of failure and calculate the average tensile strength of the 3D printed reservoir sandstones.

## **6. Results from Consolidated Drained Triaxial Testing Program**

### **6.1. Introduction**

Consolidated drained triaxial test (CD Triaxial test) is one of the most common geotechnical strength tests. To study the compressibility and volumetric behavior and to quantify the effects of confining stress on the peak strength and elastic properties of the 3D printed sandstone analogues, several CD Triaxial tests were conducted on 63.5 mm diameter by 127 mm length (2.5” by 5”) cylindrical specimens, built using 20% Furan binder saturation, 250  $\mu\text{m}$  layer thickness and printed on a 90° layering orientation.

For the reasons stated in previous sections, both pore and confining fluids using the CD Triaxial tests were silicone oil. Additionally, the complete set of tests was run at ambient temperature and the fluctuations in this measurement were recorded using a thermocouple attached to the system.

For all CD tests, graphs of deviator stress against axial strain were plotted to quantify and compare the peak and post-peak conditions, the value of the elastic properties and the influence of confining pressure on these properties. Moreover, a plot of deviator stress against volumetric strain is included to understand the volumetric behavior of the 3D printed analogues and extract useful information regarding the compressibility of this material under various levels of effective confining stress.

### **6.2. Compressibility and Volumetric Behavior Experiments**

The compressibility and volumetric behavior's during the triaxial test were performed in two stages: anisotropic specimen's consolidation and deviatoric loading to failure. The isotropic compression and the pore pressure were applied with a TELEDYNE ISCO D-Series SFX 220 pump, with a maximum pressure rate of 52 MPa; pore pressure was kept constant at 2 MPa throughout the entire experiment. During the deviatoric loading, the

hydraulic top RAM was moved at a pump's rate of 0.3 mL/min, which is equivalent to 0.042 mm/min when converted to displacement units. The volumetric strain was calculated assuming  $\varepsilon_v = \varepsilon_a + 2\varepsilon_r$ .

Figure 6. shows the typical relationship between volumetric strain and effective confining pressure for a 3D printed sandstone analogue printed with the specifications stated in the previous item. As shown in Figure 6.1, the maximum effective confining stress was 30 MPa and the total volumetric deformation achieved by the specimen after undergoing the illustrated stress path was 3.26%. One of the primary elements that become clear is that the primary loading curve does not follow the same path as the unloading one, indicating that certain amount of plastic compaction occurred during this first cycle of isotropic compression. This same observation applies to the reloading curve, in which some hysteresis can be noted when comparing it to the previous unloading process.

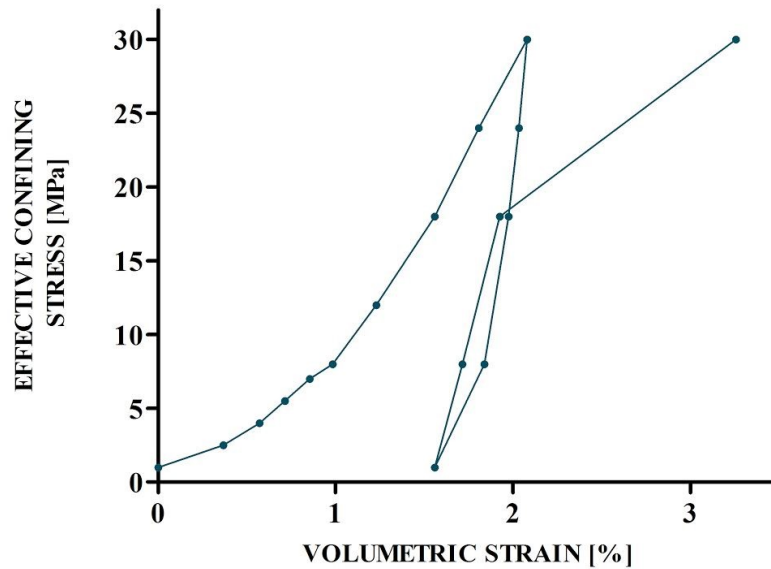


**Figure 6.1. Relationship of volumetric strain to effective confining pressure for 3DP sandstone analogues**

Analogous to the behavior observed by Sulem & Ouffroukh (2006), it can be observed that the initial portion of the stress-strain curve, up to 8 MPa effective confining stress, is

convex. This behavior can be attributed to the closing of pre-existing micro-cracks on natural reservoir rocks, in the case of the 3D printed specimens, this behavior might be generated by the compaction of poorly bound zones along the body of the analogue. There's a remarkably linear increment of the volumetric strain of the specimen with the increase in confining stress from 12 MPa. However, there is no evident variation nor decrease on the slope of the line, so it could be inferred that under this test conditions, the 3D sandstone analogue did not achieve the onset of pore collapse (Fabre & Gustkiewicz 1997).

Based on the results of volumetric strain obtained from this test, a graph of bulk compressibility against effective confining stress for the first loading cycle was plotted in Figure 6.2. The sandstone analogue's bulk compressibility ( $C_{bc}$ ) was calculated using the relationships proposed by Zimmerman (1992), Equation 6.1:

$$C_{bc} = \frac{1}{V_b^i} \left( \frac{\partial V_b}{\partial P_c} \right)_{P_p} \quad \text{Equation 6.1.}$$

where  $V_b^i$  corresponds to the initial bulk volume of the specimen, calculated basically by determining the volume of the cylindric analogue (i.e.  $V_b^i = \pi r_s^2 h_s$ ), and  $\partial V_b$  is the change in bulk volume generated by an increase/decrease in the confining stress ( $\partial P_c$ ) under a constant value of pore pressure,  $P_p$ .

The 3D printed sandstone analogues behave in the typical manner stated in the consolidation theory proposed by Terzaghi 1943, a gradual decrease on the bulk compressibility of the specimen is noticed with the continuous increase on the effective confining pressure during the loading portion of the curve. The non-linear behavior of the curve might be attributed to the continuous void space closures and the increase of grain-to-grain contact because of the surrounding stress.

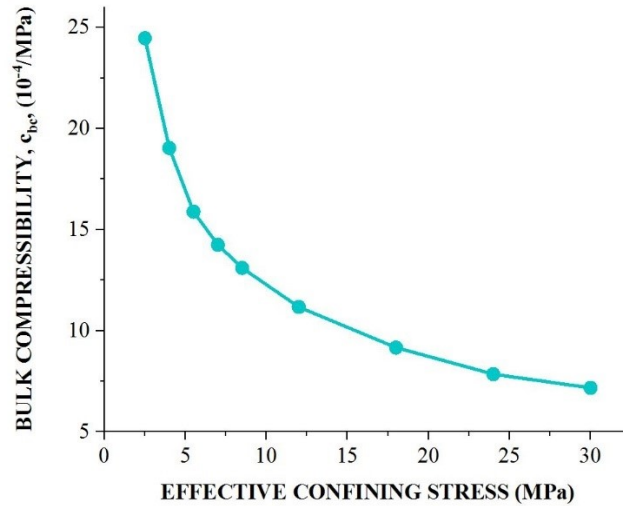


**Figure 6.2. Bulk compressibility vs. effective confining stress' relationship for 3DP sandstone analogues**

Experimental data gathered by Zimmerman (1992), allow comparing the bulk compressibility of the 3DP sandstone with results obtained from deeply-studied natural materials. In Figure 6.3, the compressibility curves from Berea and Bandera sandstones, built under a similar range of confining stresses as the ones used on these experiments, are compared with the graph obtained for the reservoir sandstone analogues. A positive aspect that can be extracted from this comparison is that the values of this property for the manufactured rocks lie within the same order of magnitude,  $10^{-4}/\text{MPa}$ , which permits researchers to be optimistic about extrapolating the volumetric behavior of this manufactured material to the actual mechanical response of a natural reservoir rock.

Clearly, the 3DP sandstones are far more compressible than both Berea and Bandera sandstones, so there is a necessity to study additional methods to produce properties of the manufactured analogues closer to those of natural sandstones. Table 6.. provides a summary of bulk compressibility data versus confining stress compilation for different natural sandstones across the United States (Fatt et al. 1958).

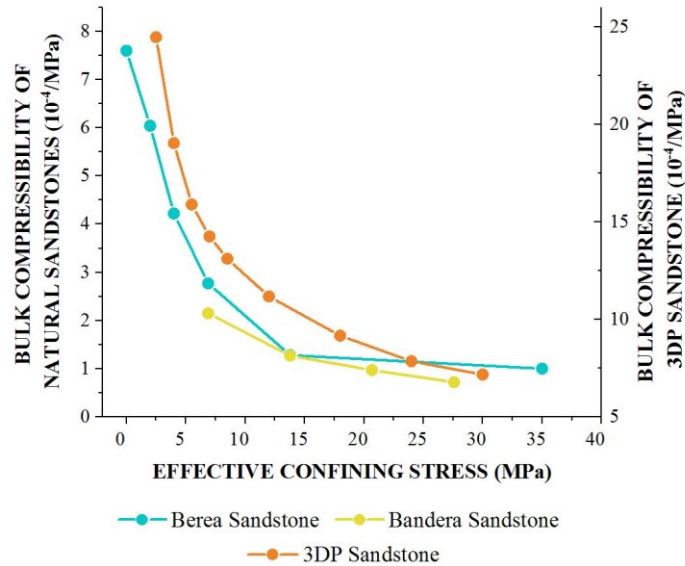


**Figure 6.3. Bulk Compressibility curves from Natural Sandstones and 3DP Sandstone analogues**

The data included in Table 6.1 that corresponds to the 3DP analogues, was obtained from effective confining stresses equal to 3.4 MPa and 27.6 MPa, which are equivalent to 500 psi and 4000 psi respectively. Referring to the data itself, it can be concluded that the bulk compressibility of the sandstone analogues has not as low magnitude as that of an unconsolidated sand and although it lies within the same range of magnitude of natural materials, it still needs to be improved to fully resemble the behavior of a consolidated rock. It was calculated that the bulk compressibility of 3DP specimens is around 6 to 7 times lower than the compressibility of a uniform natural material as Berea Sandstone. This point can be directly related to the fact that the 3DP analogues have a porosity that is nearly equivalent to that of an unconsolidated sand, while typical reservoir rocks have porosities that range between 9% and 24%. Therefore, these results strengthen the recommendations provided in previous sections, where it was pointed out that the reduction of the analogue's porosity by any mechanical or chemical medium is extremely important to enhance the similarities of the manufactured rocks to their natural pairs.

**Table 6.1. Bulk Compressibility Data for Different Natural Sandstones (After Fatt, 1958 and Zimmerman, 1992).**

Sample Number (Fatt, 1958)	Sample Source	Porosity (%)	Bulk Compressibility 10 <sup>-4</sup> /MPa	
			At 3.4 MPa (500 psi)	At 27.6 MPa (4000 psi)
-	3DP Sandstone	35.7	21	5
1	Brea Canyon	18.7	5.81	2.53
2	Huntington Beach	24.0	5.72	2.18
3	West Montalvo, CA	9.9	3.54	1.47
5	Oxnard	9.0	4.95	2.44
9	San Joaquin Valley	17.6	3.11	0.87
15	Sherman, Tx.	12.6	1.88	0.78
18	Colorado	21.1	2.06	0.81
26	Unconsolidated Sand	36.0	130.5	-
-	Berea Sandstone	19.0-26.0	4.50	1.42
-	Bandera Sandstone	15.0-21.0	2.50	0.96

For a drained hydrostatic compression test as the one studied in this section, it is possible to determine the jacketed drained bulk (i.e. secant compression) modulus,  $K$ , which can be calculated by applying the following relationship, Equation 6.2:

$$K = V \left. \frac{\Delta\sigma}{\Delta V} \right|_{jacketed} \quad \text{Equation 6.2.}$$

The calculations of the jacketed bulk modulus and their relationship with the corresponding effective confining stress of each compression stage were plotted in Figure 6.4. As it would be observed, there are two remarkable changes in the slope of the plot: first, at around 5 MPa confining stress, there is an inflection point at which the slope decreases and maintains an almost linear trend up to 24 MPa. The second variation starts exactly at this stress level,

in this case, the slope changes its trend and starts decreasing with the further increase in the confining pressure.

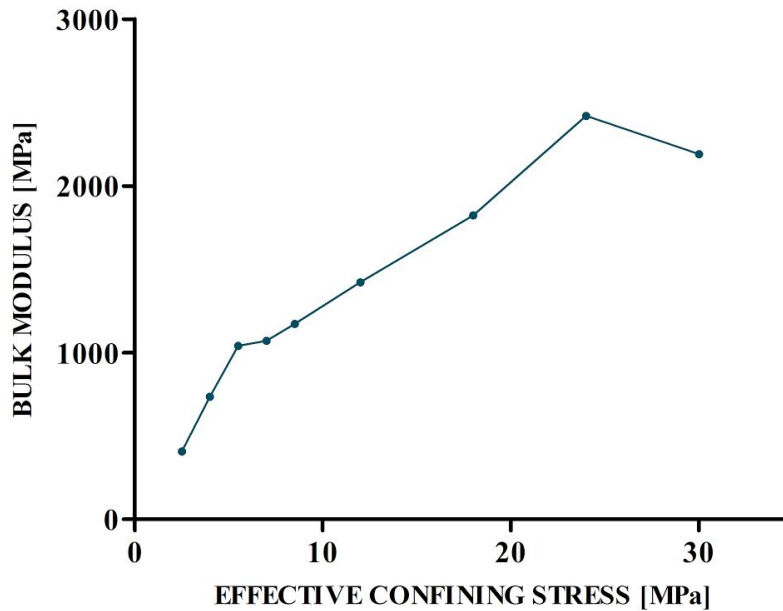


**Figure 6.4. Bulk Modulus (K) vs. Effective Confining Stress relationship for 3DP Sandstone Analogues**

The first inflection point correlates with the observations made by Ardila et al. 2017, which used the same type of material, on which 3DP analogues built using the same materials (i.e. silica sand and furan binder), experienced a plastic irreversible matrix deformation under stress levels higher than 5 MPa, evidenced by a high hysteresis on the permeability vs. confining stress plots during a loading-unloading cycle. This phenomenon seems to be correlated with the stress-dependency of the compression modulus, attributed mainly to the closing of existing micro-cracks in natural materials, or poorly bonded zones on the 3DP analogues.

With respect to the second inflection point, analogous behavior to the one observed in this experiments was also noticed in triaxial tests performed by Zimmerman (1992), Sulem et

al., (1999) and Sulem & Ouffroukh (2006). At high confining stresses, above 24 MPa for the 3DP sandstones, the bulk modulus (K) reaches a maximum value and starts a decreasing trend which can be related to the onset of grain crushing and pore collapse, which is defined as the stress level at which, triggered by extensive cracking initiated at grain-to-grain contacts and stress concentration, the grains start intruding on one another and a continuous micro-fracturing process is initiated (Menendez et al. 1996).

From experimental results gathered by Fabre & Gustkiewicz (1997), it was stated that the common range of bulk modulus for natural sandstones is 15-45 GPa, which are considerable higher values than the ones obtained for the 3DP analogues, which are located between 0.4-2.5 GPa. The values for bulk moduli for several materials also seem to correlate with mineralogical composition and rock porosity, the higher the porosity of the specimen, the lower its bulk modulus.

Finally, after completing the loading-unloading cycles previously analyzed in this section, the 3DP sandstone analogue was sheared at 30 MPa effective confining stress. The resultant stress-strain relationship is plotted in Figure 6.5. This specimen failed at a peak stress of 49.3 MPa at an axial strain of 2.48%; Young's Modulus calculated at 50% of the peak stress is 2.6 GPa and Poisson's ratio is 0.24.

At initial low stresses, there is not much contribution of lateral strain to the volumetric deformation of the specimen, axial strain generated by compression dominates the specimen's response. The progressive increase of the deviatoric stress induces lateral expansion and a distributed inelastic deformation leads to the onset of crack initiation at around 35 MPa. After failure, the specimen continues deforming rapidly, no noticeable weakening was observed and the peak strength was maintained almost constant before a slight strain hardening up to 51.3 MPa led to perfect plasticity (Zhang, Shao, Xu, Zhao, & Wang, 2015). The absence of a weakening process can be attributed to the rapid mobilization of the frictional component of the strength (Hajiabdolmajid et al., 2003), which could have been triggered by the extensive volumetric deformation inflicted on the specimen before failure process.

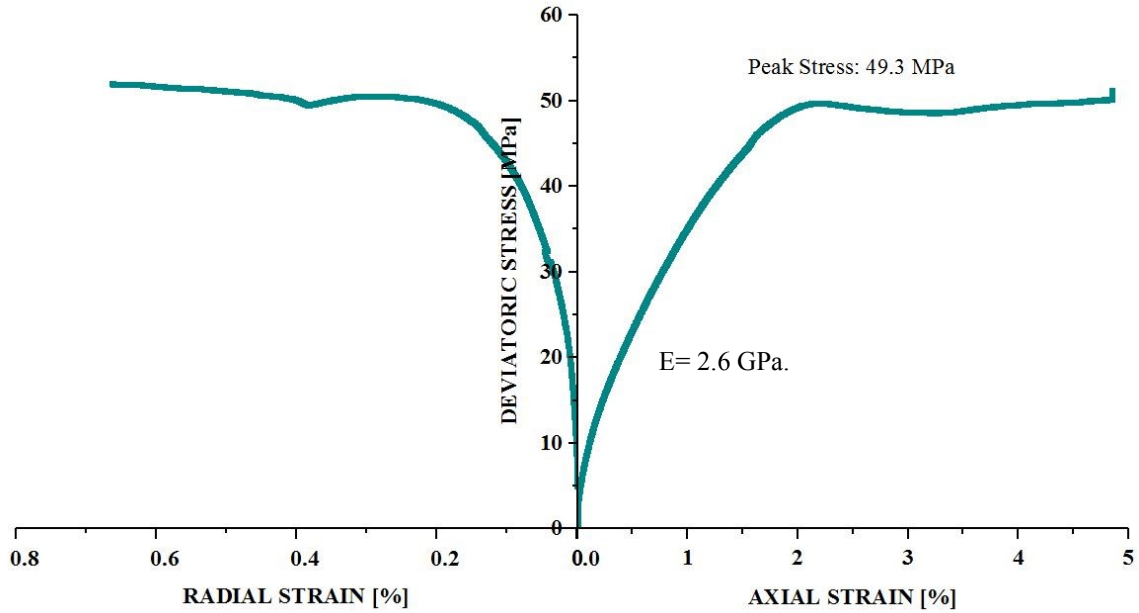


**Figure 6.5. Deviator Stress vs. Axial Strain Relationship for 3DP Analogues**

### **6.3. Effect of Confining Pressure on 3D Printed Sandstone’s Mechanical behavior**

To study the influence of confining stress on the mechanical behavior of the 3DP sandstone analogues, three consolidated drained (CD) triaxial tests were run at three levels of effective confining pressure: 10 MPa, 18 MPa and 25 MPa. To be consistent with the previous experiments, effective stresses were calculated using similarly a constant pore pressure of 2 MPa.

From each test, information regarding peak strength, elastic parameters, failure mode and volumetric behavior was extracted and compared. Additionally, assuming a linear increase in peak strength with increasing confining stress and an isotropic mechanical behavior of the 3DP material, the shear strength and failure mechanics of the specimens were modelled using Mohr-Coulomb theory, consequently, results regarding cohesion and friction angles of 3DP sandstone analogues were obtained.

**Table 6.2. Summary of results from CD Triaxial Testing on 3DP Sandstone Analogues**

<b>Effective Confining Stress (MPa)</b>	<b>Peak Deviator Stress (MPa)</b>	<b>Axial Strain at Failure (%)</b>	<b>Radial Strain at Failure (%)</b>	<b>Young's Modulus (GPa)</b>	<b>Poisson's Ratio</b>
<b>10</b>	34.3	1.57	0.61	2.74	0.19
<b>18</b>	41.1	2.28	0.38	2.86	0.16
<b>25</b>	47.0	2.69	0.54	2.99	0.10

*6.3.1. Peak Strength*

The deviator stress (q) against axial strain relationship for each CD triaxial tests are plotted in Figure 6.6.

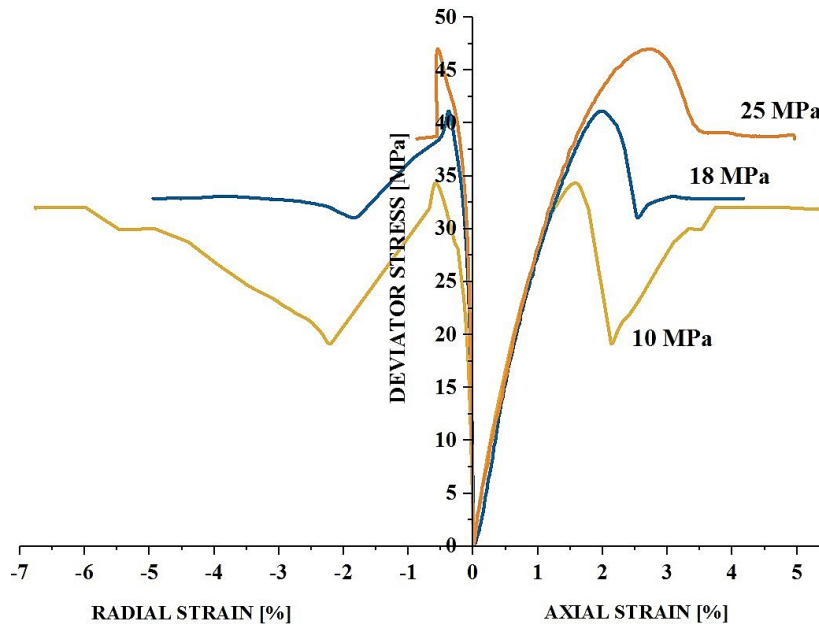


**Figure 6.6. Deviator Stress vs. Strain Relationship for 3D Printed Specimens under different confining pressures**

Additionally, Table 6.2. contains a comprehensive summary of the measured mechanical properties of each specimen depending on the degree of confining stress at which one of them was sheared at. As it would be expected before this testing procedure, there is a direct relationship between the increase in confining stress and the peak deviator stress. The specimen subjected to 10 MPa effective confining stress failed at 34.3 MPa, while the one subjected to 18 MPa effective confining stress failed at 41.1 MPa, which implies an increase of 19.8%; the specimen subjected to 25 MPa effective confining stress failed at 47 MPa, which implies an increase of 37% with respect to the lower case.

### *6.3.2. Axial Strain at Failure and Post-Peak Behavior:*

The axial strain at peak conditions for each one of the CD Triaxial tests ranged between 1.5-2.7%. As the effective confining stress at failure conditions increases so did the axial strain. The behavior of the specimens on the post-peak region seems to correlate with the observations made by Martin et al., 1997, Diederichs et al., 2003, Hajiabdolmajid et al., 2003 and Cai et al., 2009, among many others, on which at high levels of confining stress (above 5 MPa), the failure mode of strong rocks is dominated by the frictional component of the strength. As the continuum Cohesion Weakening Frictional Strengthening (CWFS) model states, the progressive damage inflicted to the rock specimen during a destructive compression test is first sustained by the cohesive forces coming from the bonding between the grains. Failure starts from the grain boundaries and the loss of the mobilized cohesive component is appreciated at the first decreasing slope after the peak is reached. Nonetheless, when significant further damage is imposed to the specimen along the failure plane, the frictional component of the strength is activated. As its name might indicate, the movement of the particles, the generated frictional forces from the readjustment of the disintegrated blocks and the grain interlocking phenomena contributes to the recovery of part of the strength of the material. These concepts are evidenced in Figure 6.6, specially for the specimens failed at 10 MPa and 18 MPa, on which there is a clear increase on the strength after the initial weakening, with a tendency towards the residual strength. In the plot of the specimen failed at 25 MPa, there is no such marked frictional strengthening and

the stress is maintained by the frictional forces until starts a decreasing pattern towards residual strength.

Also note that there is no initial softened slope attributed to any crack closure phenomenon, this is probably because of the previous consolidation stages, during which the specimens were compacted, and the pore structure started deforming and closing any pre-existing void or poorly cemented zones.

### *6.3.3. Strength Parameters and Mohr-Coulomb Failure Criterion*

Young's Modulus of the 3D printed analogues seem to remain unaffected throughout the set of experiments conducted at different confining stresses, the stress-strain plot starts to deviate from its initial linear elastic behavior at about 40% of the peak stress. Poisson's ratio exhibits an apparent decrease on its value, this result can be attributed to the increase on the confining pressure that hinders the lateral expansion of the specimen, which mathematically is observed on the increase of the slope of the deviator stress vs. lateral strain slope.

Figure 6.7 shows the Mohr Circles for the 3-consolidated drained triaxial tests conducted on the sandstone analogues. As expected, there is an appreciable increase in the shear stress with the corresponding increase in the effective confining stress conditions at failure. The color code of this plots follows the same conventions defined previously in Figure 6.6. Assuming a linear failure envelope, as it is shown in the figure, an effective cohesion of 9.1 MPa and a friction angle of  $29.7^\circ$  describes the mechanical behavior of this material under triaxial failure conditions.

To contextualize these results, observations performed in some natural reservoir materials have shown: Red Sandstone (China):  $c'=28.4$  MPa and  $\phi'=35.7^\circ$  (Wang et al., 2012), Berea Sandstone:  $c'=26.1$  MPa and  $\phi'=24^\circ$ , Weber Sandstone:  $c'=70$  MPa and  $\phi'=31^\circ$  and Tennessee Sandstone:  $c'=50$  MPa and  $\phi'=40^\circ$  (Schellart et al., 2000)

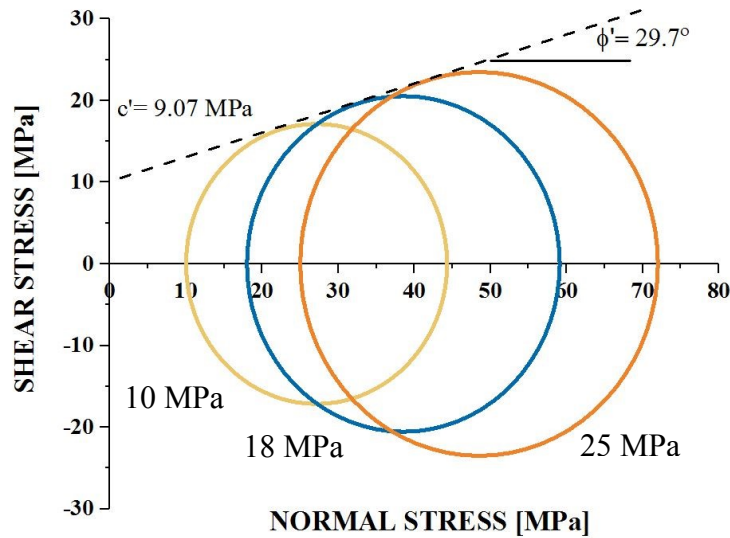


**Figure 6.7. Mohr Circles for the drained triaxial tests conducted on 3DP analogues**

#### 6.3.4. Volumetric Strain

The specimens sheared at 10 MPa and 18 MPa effective confining stress exhibited a behavior comparable to that of medium to dense sands, at the beginning of the test, the analogue undergoes compression (i.e. decrease in volume) and after reaching 1.8% and 2.4% axial strain respectively, it undergoes remarkable dilation of around 5-6% volumetric strain. The specimen sheared at 25 MPa exhibit a behavior that corresponds to that of a loose sand, from the beginning of the test, the specimen just displays a compactive behavior. Unlike natural sandstones, there is no final dilatant behavior after failure (Figure 6.8).

It should be noted that at the initial moments of the shearing process, there's no initial compaction showed by any specimen, this phenomenon is probably generated by the effects of the confining stress on the sandstone analogues. As it was previously discussed, the approximate stress level at which any poorly bounded zones of the cylinder are closed by the action of the surrounding fluid pressure is 5 MPa.

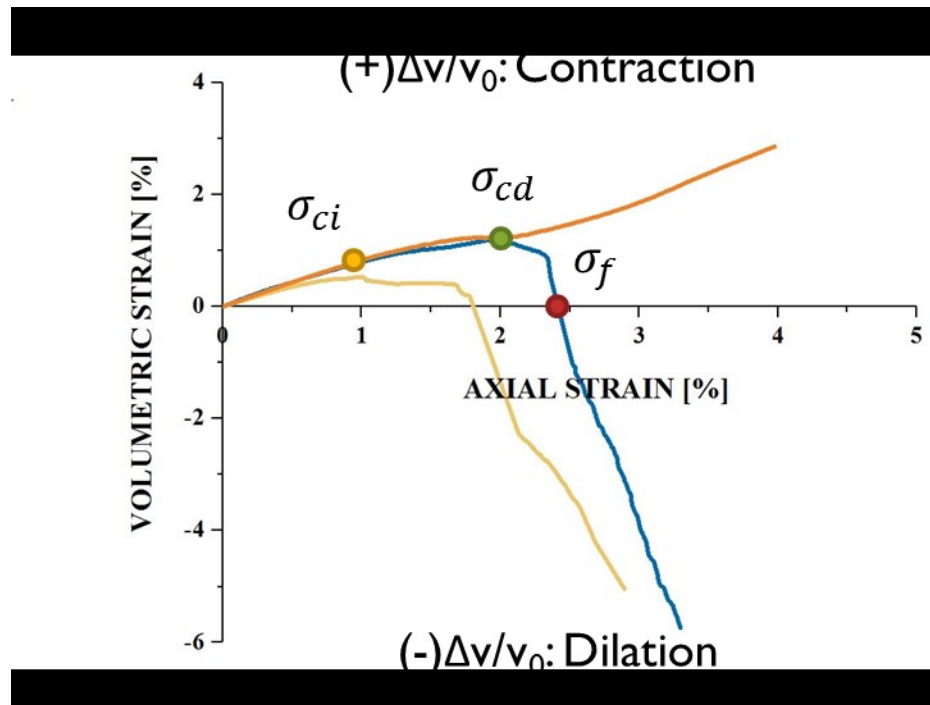


**Figure 6.8. Volumetric behavior of 3D printed analogues under triaxial conditions**

### 6.3.5. Failure Mode of the Specimens

The triaxial cylinders failed at some well-defined inclined shear planes at the angles exhibited by Figure 6.9 (between  $55^\circ$  and  $60^\circ$ ). When applying the Mohr-Coulomb theory, the inclination angle of the failure plane,  $\beta$ , which equivaless to  $45+\varphi/2$ , obtained from the three triaxial tests result in an average friction angle,  $\varphi$ , of  $29^\circ$ . These results are in accordance with the theoretical equation obtained from the Mohr envelopes plotted in Figure 6.7.

The specimen sheared at 10 MPa effective confining stress also developed failure planes perpendicular to the main shear surface. Some little pieces of poorly bounded sand come out of the cylinder's surface after removing the silicone membrane.

The difference in color exhibited by Figure 6.9 is due just to the adjustments of the color saturation and brightness of the camera while taking the pictures.

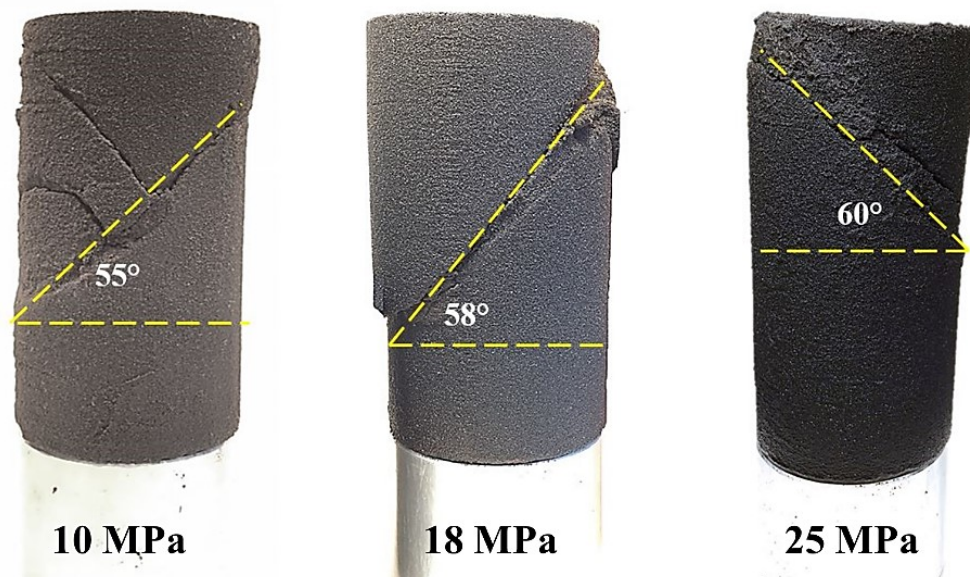


**Figure 6.9. Failure Modes of 3D Printed Specimens under Triaxial Conditions**

#### **6.4. Hoek & Brown Failure Criterion for 3D Printed Sandstones**

Using the results gathered along this mechanical experimental campaign: UCS tests, Direct Tension tests and CD Triaxial tests, it was possible to calculate the Hoek and Brown Failure criterion for the 3D printed sandstone analogues, Equation 6.3, with help of the Rocscience software, RocLab.

$$\sigma_1 = \sigma_3 + \sigma_{ci} \left( m_i \frac{\sigma_3}{\sigma_{ci}} + s \right)^a \quad \text{Equation 6.3}$$

To fulfill the requirements of the calculation software, the Geological Strength Index (GSI) for the sandstones was established as 100 (intact material without discontinuities or fractures). The calculated intact uniaxial strength was 24.7 MPa and the  $m_i$  obtained was 2.63, which is slightly lower than the results obtained for natural sandstones. These results

are shown in Figure 6.10. The blue line shows the corresponding Mohr-Coulomb failure criterion for this material, while the red line is the Hoek-Brown failure criterion.

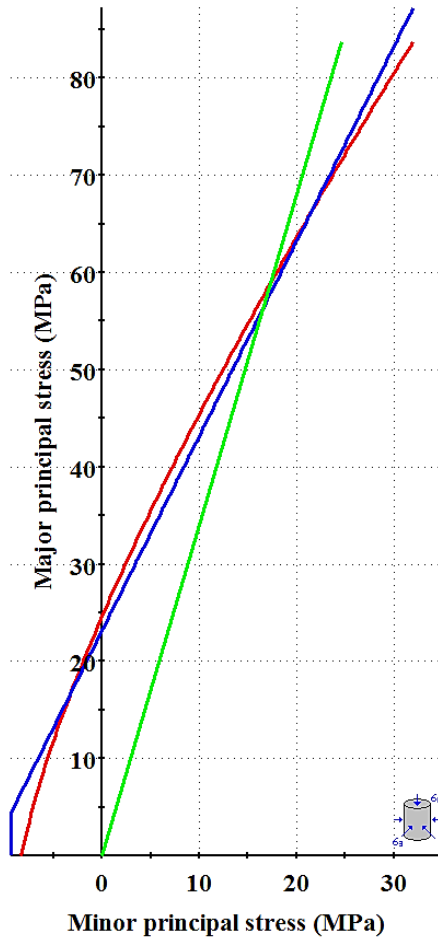


**Figure 6.10. Hoek & Brown Failure Criterion for 3D Printed Reservoir Sandstones**

The green line corresponds to the Mogi's line, defined by Mogi in 1966. This line indicates the limit at which the failure mechanism of the rock material changes from brittle dominated (to the left) to ductile dominated (to the right). For 3DP Sandstone analogues, this phenomenon occurs around a  $\sigma_3=17.5$  MPa. These results are in good agreement to what it was observed in the CD triaxial tests, on which at 18 MPa confining stress, the effects of the frictional strengthening process seem to be reduced until reaching a plastic post-peak residual behavior at 25 MPa.

Physically, the fracture behavior does not correspond to one of a ductile material. Even at 25 MPa, the failure mode of the specimens was materialized into an inclined fracture plane, which is typical of a brittle behavior. Nonetheless, the results from the Bulk Modulus behavior (change in slope) and the volumetric behavior (persistent compaction) indicate that the material is deforming under a ductile regime. It was concluded that at that level of stress, the 3D printed analogues fail to exhibit a mixed-failure behavior. More tests are required to confirm these observations.

### 6.5. Parallel between the properties of 3D Printed Sandstones with natural reservoir sandstones

A direct comparison of 3DP specimens with Berea Sandstone is shown in Figure 6.11.

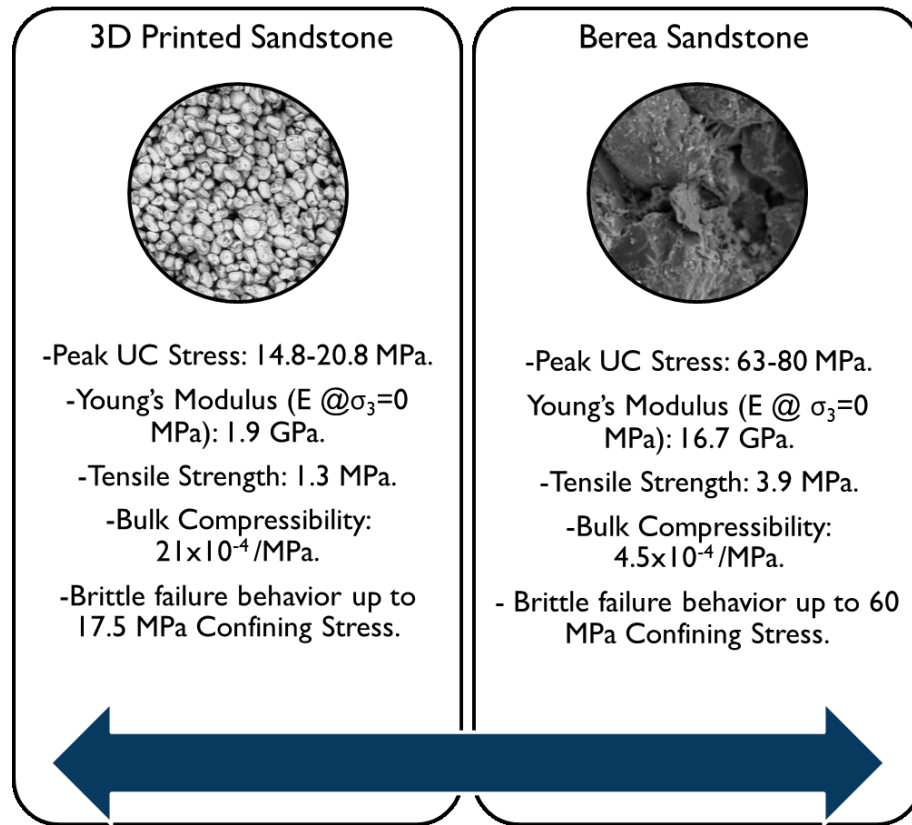


**Figure 6.11. Comparison between the properties of 3D Printed analogues and Berea Sandstone**

The peak UC strength of the 3D printed sandstones can be increased up to 40 MPa, which would be half of the strength of the designed natural sandstone. Young's Modulus is considerably low compared with the one of Berea Sandstone (around 1/6 of the value). The bulk compressibility of the rock analogues was identified to be around 1/5 of the value of Berea Sandstone; this phenomenon can be explained by the high porosity (35.7%) of the 3D printed specimens.

## **6.6. Future Research Work**

The CD triaxial tests performed during the experimental campaign of this research work were performed within the section of an elevated level of confining stresses. It has been well defined by previous authors that the failure behavior of rocks subjected to high confining pressures is completely dominated by the frictional component of strength and the strain limit at which it is activated.

Further research efforts should be focused on performing CD triaxial tests at lower levels of confining stress (1 MPa to 5 MPa) to investigate the strain limit of both the cohesion loss and the component of frictional strengthening. This information would be useful to establish the brittle-ductile behavior of the failure process of this type of material.

## 7. Conclusions and Recommendations

### 7.1. Mechanical Properties Summary Table

A complete summary table of the mechanical properties of the 3D printed sandstone analogues is included in. The row highlighted in yellow corresponds to the values obtained for the base case designed for comparison results.

**Table 7.1. Summary Table of Mechanical Properties of 3DP Sandstone Analogues**

Laboratory Test	Binder Saturation	Printing Layer Orientation	Printing Layer Thickness
UCS	10%: $\sigma_c = 14.8$ MPa	0°: $\sigma_c = 14.8$ MPa	
		25°: $\sigma_c = 15.5$ MPa	250 $\mu\text{m}$ : $\sigma_c = 14.8$ MPa
	15%: $\sigma_c = 18.0$ MPa	45°: $\sigma_c = 15.4$ MPa	
		65°: $\sigma_c = 14.9$ MPa	400 $\mu\text{m}$ : $\sigma_c = 8.6$ MPa
	20%: $\sigma_c = 20.8$ MPa	90°: $\sigma_c = 17.1$ MPa	
	Brazilian Test	$\sigma_t = 3.5$ MPa with a time to failure of 6.7 minutes	
Direct Tension Test	10%	0°: $\sigma_t = 1.3$ MPa	250 $\mu\text{m}$
		90°: $\sigma_t = 0.6$ MPa	
CD Triaxial Test	BS: 20% - LO: 90° - LT: 250 $\mu\text{m}$		
	Compressibility (@ $\approx 500$ psi): $21 \times 10^{-4}$ /MPa		
Thermal Curing Process	UC Strength is increased to 40 MPa for specimens built with BS: 20% - LO: 90° - LT: 250 $\mu\text{m}$		

## 7.2. Summary

Advances in additive manufacturing (AM) technology have enabled the use of sand as a 3D printing material. This has allowed 3D printed sandstone analogues to be produced such that there is an apparent reduced specimen-to-specimen heterogeneity and conversely, provides exacting control over the explicit inclusion of heterogeneity, such as fractures, within a specimen.

By knowing and controlling inter-sample variability in terms of porosity, fracture networks, grain size distribution, and density distribution, 3D printing of geomaterials provides a valuable tool to validate numerical models, develop scaling laws and constitutive relationships, quantify the degree of influence of pore geometry, fracture network characteristics, and structural heterogeneity on macroscopic properties.

Throughout this study, it has been confirmed that the use of Furan Binder jetting with silica sand powder technique, improves the range of values of some important mechanical and elastic properties (i.e. UCS Peak Strength, Young's Modulus and Poisson's Ratio), in comparison with previous efforts performed with other types of materials (i.e. plastic, metal powders and gypsum).

Different printing configurations and features were tested to verify their influence on the mechanical properties of the specimens. The first one is the layer inclination angle, for which  $0^\circ$ ,  $25^\circ$ ,  $45^\circ$ ,  $65^\circ$  and  $90^\circ$  inclined printing layers measured from the axial applied load direction, were used to build identical sandstone specimens. The highest average Peak UCS Strength (17.1 MPa) was obtained on  $90^\circ$  inclined samples, whereas the weakest group of samples was provided by the  $0^\circ$  inclined angles (14.8 MPa). Regarding the mode of failure of the samples,  $0^\circ$ ,  $25^\circ$  and  $65^\circ$  exhibited a predominant axial splitting, while  $45^\circ$  and  $90^\circ$  failed in a well-defined inclined plane of about  $60^\circ$  of inclination. On the other hand, it was found that  $0^\circ$  inclined samples undergo a noticeable influence of the printing process on the mode of failure and presumably on their average peak strength. This configuration should be avoided to bypass any non-homogeneity for further experimental research.

The influence of Furan binder saturation on the mechanical properties of the 3D printed specimens was studied using three different saturation values (10%, 15% and 20%), keeping the same layer orientation and thickness, while the repercussion of printing layer thickness was studied using two thicknesses (250  $\mu\text{m}$  and 400  $\mu\text{m}$ ), while maintaining a constant binder saturation and layer orientation. To summarize these sections, it can be concluded that the higher the binder saturation, the stronger the sandstone analogue, while the higher the layer thickness, the weaker the specimen. This behavior is directly related to the volume and distribution of Furan binder inside the pore space of the samples, respectively.

Brazilian (i.e. indirect) tensile strength of the 3D printed sandstone analogues resulted to be around 1/5 of the uniaxial compressive strength, while direct tensile strength was measured to be 1/12 of this same property. This is a considerably fair value if considering that in natural materials with high porosity ( $>20\%$ ), this relationship is around 1/5 to 1/10. During the tension testing campaign, there was also appreciated an influence of the building process on the failure mode of the  $90^\circ$ -oriented direct tension specimens, which failed at a perfectly horizontal surface, coincident with one of the building plane. DTS resulted to be 37% of the BTS on average. This value is considerably low when compared to the relationship established for natural sandstones (70%). The appreciable difference between the values of the BT strength and the DT strength are also attributed to the experimental set up differences between each test. It is possible that due to the higher contact area of the applied load during the Brazilian tests, there was a stress concentration at the end of the disk specimens, generating a higher indirect tensile strength.

The compressibility of the 3D printed sandstone analogues has the same order of magnitude of a natural reservoir rock. Nevertheless, due to the high porosity that this type of material possesses (around 36%), their volumetric deformation is around 6 times the one observed in Berea Sandstone. Additionally, during the isotropic compression stages at which the specimens were subjected, both the onset of crack closure (5 MPa) and the onset of pore collapse (24 MPa) were appreciated. Additional research is required to confirm these phenomena. When comparing the onset of pore collapse with the value obtained for well-

documented natural rocks, as Fontainebleau sandstone, on which it was measured to be around 40 MPa, the value is also lower.

Consolidated drained (CD) triaxial tests conducted on the 3D printed sandstone analogues revealed that, as natural reservoir rocks, the peak shear stress of the sandstone analogues have a direct relationship with the effective confining stress conditions at failure, this is to say, the higher the  $\sigma_3$  at failure, the higher the strength of the specimen. Additionally, the Mohr's Failure envelope of this material is described by a cohesion of 9.1 MPa and a friction angle of 29.7°. Finally, the specimens sheared at 10 MPa and 18 MPa confining stresses exhibited a volumetric behavior comparable to a medium to dense sand, while the one sheared at 25 MPa showed a volumetric behavior analogous to a dense sand. The failure behavior of the 3DP sandstone analogues seems to follow the CWFS theory.

Certainly, 3D printing technology with sand stands as a feasible solution to replicate consistent and repeatable rock specimens, which are suitable for performing any kind of laboratory experiments. Furthermore, the results obtained up to this point, lead to consider that this technology might be suitable to provide an answer to many engineering problems in Reservoir Geomechanics field, specifically related to the repeatability of the results, homogeneity sample-to-sample, scale-up issues and pore-structure variability. However, it is necessary to establish a comprehensive protocol to define the standards on the mechanical testing of this type of materials, defining the sensitivity of the analogues to each printing feature, with the final scope of avoiding anisotropy on the results due to these parameters.

### **7.3. Recommendations**

Mechanical and elastic properties of 3D Printed sandstone analogues were found to be lower than the values encountered for natural reservoir sandstones. This point leads to the fact that further investigation is needed to encounter different alternatives that benefit to enhance these values to more realistic ones. Some early efforts are directed to reduce the porosity of the specimens (found to be close to 36% when using a binder saturation of 20%)

by using mechanical and vibratory powder compaction techniques (i.e. change powder packing ratio) or epoxy infiltration, which ultimately benefits the increment of the mechanical strength of the sandstone analogues.

Another important aspect to assess is the clear influences of the building process on the strength and mode of failure of the specimens observed on the testing campaign developed in this project. This phenomenon could be a consequence of the Furan-Silica sand surface interaction. Recent studies are directed to explore the improvement of the adhesion of the Furan binder (organic component) to the surface of the silica sands grains (inorganic material), which will potentially reduce the development of failure surfaces through planes of weakness materialized along the building planes.

Reducing the packing ratio at which the powdered material is deposited onto the building box and therefore the resulting porosity of the 3D printed analogues, will highly benefit the adjustment of fundamental mechanical properties such as compressive strength, tensile strength and volumetric behavior (i.e. compressibility), to turn them into more natural rock-like results.

To conclude this study, the stronger and most competent sandstone analogues that can be obtained with the technological and research advances achieved up to this point are the cylindrical specimens built using a minimum binder saturation of 20%, using a layer orientation of  $90^\circ$  (i.e. layering perpendicular to the compression load direction) and a maximum layer thickness of 250  $\mu\text{m}$ .

## References

- Ardila, N. (2017). Hydraulic Properties Characterization of 3D Printed Reservoir Sandstone Analogues. *4th Internal Research Symposium of the Reservoir Geomechanics Research Group*, University of Alberta.
- ASTM D2938-08. (2016). Standard Test Method for Direct Tensile Strength of Intact Rock Core Specimens. *ASTM International, West Conshohocken, PA.*, 15–17. <https://doi.org/10.1520/D2936-08.2>
- ASTM D3967-08 (2008b). (2008). Standard Test Method for Splitting Tensile Strength of Intact Rock Core Specimens. *ASTM International, West Conshohocken, PA.*, 1–5. <https://doi.org/10.1520/D3967-08.2>
- ASTM D7012-14. (2004). Compressive Strength and Elastic Moduli of Intact Rock Core Specimens under Varying States of Stress and Temperatures 1. *Stress: The International Journal on the Biology of Stress*, (February), 4–11. <https://doi.org/10.1520/D7012-14.1.5.1.1>
- Attewell, P. B., & Sandford, M. R. (1974). Intrinsic shear strength of a brittle, anisotropic rock-I. Experimental and mechanical interpretation. *International Journal of Rock Mechanics and Mining Sciences and*, 11(11), 423–430. [https://doi.org/10.1016/0148-9062\(74\)90453-7](https://doi.org/10.1016/0148-9062(74)90453-7)
- Bell, F. G. (1978). The physical and mechanical properties of the Fell Sandstones, Northumberland, England. *Engineering Geology*, 12, 1–29.
- Bellini, A., & Güçeri, S. (2003). Mechanical characterization of parts fabricated using fused deposition modeling. *Rapid Prototyping Journal*, 9(4), 252–264. <https://doi.org/10.1108/13552540310489631>
- Cai, M. (2009). Practical Estimates of Tensile Strength and Hoek – Brown Strength Parameter  $m_i$  of Brittle Rocks. *Rock Mechanics and Rock Engineering*. <https://doi.org/10.1007/s00603-009-0053-1>

- Cai, M. (2010). Practical Estimates of Tensile Strength and Hoek – Brown Strength Parameter  $m_i$  of Brittle Rocks. *Rock Mechanics and Rock Engineering*, 43, 167–184. <https://doi.org/10.1007/s00603-009-0053-1>
- Carroll, R., & Long, M. (2017). Sample Disturbance Effects in Silt. *Journal of Geotechnical and Geoenvironmental Engineering*, 143(9), 1–11. [https://doi.org/10.1061/\(ASCE\)GT.1943-5606.0001749](https://doi.org/10.1061/(ASCE)GT.1943-5606.0001749).
- Chapwanya, M., & Stockie, J. M. (2010). Numerical simulations of gravity-driven fingering in Unsaturated porous media using a Non-equilibrium Model. *American Geophysical Journal: Water Resources Research*, 46(9). <https://doi.org/10.1029/2009WR008583>
- Cueto-Felgueroso, L., & Juanes, R. (2009). A phase field model of unsaturated flow. *Water Resources Research*, 45(10), 1–23. <https://doi.org/10.1029/2009WR007945>
- Diederichs, M. S. (2003). Manuel Rocha Medal Recipient: Rock Fracture and Collapse Under Low Confinement Conditions. *Rock Mechanics and Rock Engineering*, 36(5), 339–381. <https://doi.org/10.1007/s00603-003-0015-y>
- Es-Said, O. S., Foyos, J., Noorani, R., Mendelson, M., Marloth, R., Pregger, B. A. (2000). Effect of Layer Orientation on Mechanical Properties of Rapid Prototyped Samples. *Materials and Manufacturing Processes*, 15(1), 107–122. <https://doi.org/10.1080/10426910008912976>
- Ex-ONE. (2014). Ex-ONE M-Flex™ User Manual version 1.02.07.
- Fabre, D., & Gustkiewicz, J. (1997). Poroelastic Properties of Limestones and Sandstones under hydrostatic conditions. *International Journal of Rock Mechanics and Mining Sciences & Geomechanics Abstracts*, 34(1), 127–134. [https://doi.org/10.1016/S0148-9062\(96\)00037-X](https://doi.org/10.1016/S0148-9062(96)00037-X)
- Fakhimi, A., & Hemami, B. (2015). Axial splitting of rocks under Uniaxial Compression. *International Journal of Rock Mechanics and Mining Sciences*, 79, 124–134.
- Farzadi, A., Waran, V., Solati-Hashjin, M., Rahman, Z., Asadi, M., & Osman, N. (2015).

- Effect of Layer Printing delay on mechanical properties and dimensional accuracy of 3D Printed porous prototypes in Bone Tissue Engineering. *Ceramics International*, 41(7), 8320–8330. <https://doi.org/10.1016/j.ceramint.2015.03.004>
- Farzadi, A., Solati-Hashjin, M., Asadi-Eydivand, M., & Osman, N. A. A. (2014). Effect of layer thickness and printing orientation on mechanical properties and dimensional accuracy of 3D printed porous samples for bone tissue engineering. *PLoS ONE*, 9(9), 1–14. <https://doi.org/10.1371/journal.pone.0108252>
- Fatt, I. (1958). Compressibility of Sandstones at Low to Moderate Pressures. *AAPG Bulletin*, 42(8), 1924–1957. <https://doi.org/10.1306/0BDA5B8E-16BD-11D7-8645000102C1865D>
- Fereshtenejad, S., Song, J. J. (2016). Fundamental Study on Applicability of Powder-Based 3D Printer for Physical Modeling in Rock Mechanics. *Rock Mechanics and Rock Engineering*, 49(6), 2065–2074. <https://doi.org/10.1007/s00603-015-0904-x>
- Frketic, J., Dickens, T., & Ramakrishnan, S. (2017). Automated manufacturing and processing of fiber-reinforced polymer ( FRP ) composites : An additive review of contemporary and modern techniques for advanced materials manufacturing. *Additive Manufacturing*, 14, 69–86. <https://doi.org/10.1016/j.addma.2017.01.003>
- Fuenkajorn, K., & Klanphumeesri, S. (2010). Determination of direct tensile strength and stiffness of intact rocks. *Rock Mechanics in Civil and Environmental Engineering*, 79–82.
- Fuenkajorn, K., & Klanphumeesri, S. (2011). Laboratory determination of Direct Tensile Strength and Deformability of Intact Rocks. *Geotechnical Testing Journal*, 34(1), 97–102. <https://doi.org/10.1520/GTJ103134>
- Gaefke, C. B., Botelho, E. C., Ferreira, N. G., Rezende, M. C. (2007). Effect of Furfuryl Alcohol Addition on the Cure of Furfuryl Alcohol Resin Used in the Glassy Carbon Manufacture. *Journal of Applied Polymer Science*, 106, 2274–2281. <https://doi.org/10.1002/app>

- Gao, W., Zhang, Y., Ramanujan, D., Ramani, K., Chen, Y., Williams, C. B., ... Zavattieri, P. D. (2015). The status, challenges and future of additive manufacturing in engineering. *Computer-Aided Design*, *69*, 65–89.
- Gibson, I., & Rosen, David, Stucker, B. (2015). *Additive Manufacturing Technologies* (Second Edi). Springer New York. <https://doi.org/10.1007/978-1-4939-2113-3>
- Gomez, J. S., Ardila, N., Chalaturnyk, R. J., & Zambrano-Narvaez, G. (2017). Reservoir Geomechanical Properties Characterization of 3D Printed Sandstone. In *Proceedings of the VI Biot's Conference in Poromechanics* (pp. 952–960). Paris: ASCE.
- Griffith, A. A. (1921). The Phenomena of Rupture and Flow in Solids. *Philosophical Transactions of the Royal Society of London.*, *221*, 163–198.
- Guo, H., & Aziz, N.I., Schmidt, L. C. (1993). Rock fracture toughness determination by the Brazilian test. *Engineering Geology*, *33*(3), 177–181.
- Haimson, B. C., & Cornet, F. H. (2003). ISRM suggested methods for rock stress estimation-part 3: Hydraulic fracturing (HF) and/or hydraulic testing of pre-existing fractures (HTPF). *International Journal of Rock Mechanics and Mining Sciences*, *40*(7–8), 1011–1020. <https://doi.org/10.1016/j.ijrmms.2003.08.002>
- Hajiabdolmajid, V., Kaiser, P., and Martin, C. D. (2003). Mobilised strength components in brittle failure of rock. *Geotechnique*, (53–3), 327–336.
- Hajiabdolmajid, V., & Kaiser, P. (2003). Brittleness of rock and stability assessment in hard rock tunneling. *Tunnelling and Underground Space Technology*, *18*, 35–48.
- Hanaor, D. A. H., Gan, Y., Revay M., Airey, D. W., E. I. (2016). 3D printable geomaterials. *Geotechnique*, *66*(4), 323–332.
- Head, D., & Vanorio, T. (2016). Effects of changes in rock microstructures on permeability: 3-D printing investigation. *Geophysical Research Letters*, 7494–7502. <https://doi.org/10.1002/2016GL069334>.Received
- Hoek, E. (2006). *Practical Rock Engineering*. North Vancouver, British Columbia.

- Hu, S-c., Tan, Y-l., Zhou, H., Guo, W-y., Hu, D-w., Meng, F-z., Liu, Z. (2017). Impact of Bedding Planes on Mechanical Properties of Sandstone. *Rock Mechanics and Rock Engineering*, 50(8), 2243–2251. <https://doi.org/10.1007/s00603-017-1239-6>
- International Society for Rock Mechanics Commission on Standardization of Laboratory and Field Tests. (1978). Suggested Methods for Determining Tensile Strength of Rock Materials. *International Journal of Rock Mechanics and Mining Sciences*, 15, 99–103.
- Jiang, C., & Zhao, G.-F. (2015). A Preliminary Study of 3D Printing on Rock Mechanics. *Rock Mechanics and Rock Engineering*, 48, 1041–1050. <https://doi.org/10.1007/s00603-014-0612-y>
- Jiang, Q., Feng, X., Song, L., Gong, Y., Zheng, H., & Cui, J. (2016). Modeling rock specimens through 3D printing: Tentative experiments and prospects. *Acta Mechanica Sinica*, 32(1), 101–111. <https://doi.org/10.1007/s10409-015-0524-4>
- Khaing, M. W., Fuh, J. Y. H., & Lu, L. (2001). Direct metal laser sintering for rapid tooling: Processing and characterisation of EOS parts. *Journal of Materials Processing Technology*, 113(1–3), 269–272. [https://doi.org/10.1016/S0924-0136\(01\)00584-2](https://doi.org/10.1016/S0924-0136(01)00584-2)
- Lee, C. S., Kim, S. G., Kim, H. J., & Ahn, S. H. (2007). Measurement of anisotropic compressive strength of rapid prototyping parts. *Materials Processing Technology*, 187–188, 627–630. <https://doi.org/10.1016/j.jmatprotec.2006.11.095>
- Martin, C. D. (1997). Seventeenth Canadian Geotechnical Colloquium: The effect of cohesion loss and stress path on brittle rock strength. *Canadian Geotechnical Journal*, 34, 698–725.
- McKillip, W. J. (1989). Chemistry of Furan Polymers. *Adhesives from Renewable Resources*, 408–423. <https://doi.org/10.1021/bk-1989-0385.ch029>
- Menendez, B., Zhu, W., & Wong, T. (1996). Micromechanics of brittle faulting and cataclastic flow in Berea sandstone. *Journal of Structural Geology*, 18(1), 1 to 16. [https://doi.org/10.1016/0191-8141\(95\)00076-P](https://doi.org/10.1016/0191-8141(95)00076-P)

- Nguyen, S., Chemenda, A. I., & Ambre, J. (2011). Influence of the loading conditions on the mechanical response of granular materials as constrained from experimental tests on synthetic rock analogue material. *International Journal of Rock Mechanics and Mining Sciences*, 48(1), 103–115. <https://doi.org/10.1016/j.ijrmms.2010.09.010>
- Osinga, S., Zambrano-Narvaez, G., Chalaturnyk, R. J. (2015). Study of geomechanical properties of 3D printed sandstone analogue. In *Conference Proceedings of the American Rock Mechanics Association, 2015*. San Francisco, CA.
- Perras, M. A., & Diederichs, M. S. (2014). A Review of the Tensile Strength of Rock: Concepts and Testing. *Geotechnical and Geological Engineering*, 32(2), 525–546. <https://doi.org/10.1007/s10706-014-9732-0>
- Primkulov, B., Chalaturnyk, J., Chalaturnyk, R., & Zambano-Narvaez, G.. (2017). 3D Printed Sandstone Strength : Curing of Furfuryl Alcohol Resin-Based Sandstones. *3D Printing and Additive Manufacturing*, 4–3, 149–155. <https://doi.org/10.1089/3dp.2017.0032>
- Pul, S. (2008). Experimental investigation of tensile behaviour of high strength concrete. *Indian Journal of Engineering and Material Sciences*, 15, 467–472.
- Rankin, T. M., Giovinco, N. A., Cucher, D. J., Watts, G., Hurwitz, B., & Armstrong, D. G. (2014). Three-dimensional printing surgical instruments: Are we there yet? *Journal of Surgical Research*, 189(2), 193–197. <https://doi.org/10.1016/j.jss.2014.02.020>
- Roberson, D. A., Torrado, A. R., Shemelya, C. M., Rivera, A., Macdonald, E., & Wicker, R. B. (2015). Comparison of stress concentrator fabrication for 3D printed polymeric izod impact test specimens. *Additive Manufacturing*, 7, 1–11. <https://doi.org/10.1016/j.addma.2015.05.002>
- Ruffolo, R. M., & Shakoor, A. (2009). Variability of unconfined compressive strength in relation to number of test samples. *Engineering Geology*, 108, 16–23. <https://doi.org/10.1016/j.enggeo.2009.05.011>
- Rybicki, F. J. (2015). 3D Printing in Medicine : an introductory message from the Editor-

in-Chief. *3D Printing in Medicine*. 3D Printing in Medicine.  
<https://doi.org/10.1186/s41205-015-0001-5>

- Sachs, E., Haggerty, S., Michael, J., & Williams, P. A. (1993). *Three-Dimensional Printing Techniques*. United States.
- Schellart, W. P. (2000). Shear test results for cohesion and friction coefficients for different granular materials: Scaling implications for their usage in analogue modelling. *Tectonophysics*, *324*, 1–16.
- Schumacher, M., Deisinger, U., Ziegler, G., & Detsch, R. (2010). Indirect rapid prototyping of biphasic calcium phosphate scaffolds as bone substitutes: Influence of phase composition, macroporosity and pore geometry on mechanical properties. *Journal of Materials Science: Materials in Medicine*, *21*(12), 3119–3127.  
<https://doi.org/10.1007/s10856-010-4166-6>
- Sheorey, P. R., Biswas, A. K., & Choubey, V. D. (1989). An empirical failure criterion for rocks and jointed rock masses. *Engineering Geology*, *26*(2), 141–159.  
[https://doi.org/10.1016/0013-7952\(89\)90003-3](https://doi.org/10.1016/0013-7952(89)90003-3)
- Sulem, J., & Ouffroukh, H. (2006). Hydromechanical behaviour of Fontainebleau sandstone. *Rock Mechanics and Rock Engineering*, *39*(3), 185–213.  
<https://doi.org/10.1007/s00603-005-0065-4>
- Sulem, J., Vardoulakis, I., Papamichos, E., Oulahna, A., & Tronvoll, J. (1999). Elasto-plastic modelling of Red Wildmoor sandstone. *Mechanics of Cohesive-Frictional Materials*, *4*(3), 215–245. [https://doi.org/10.1002/\(SICI\)1099-1484\(199905\)4:3<215::AID-CFM61>3.0.CO;2-8](https://doi.org/10.1002/(SICI)1099-1484(199905)4:3<215::AID-CFM61>3.0.CO;2-8)
- Suzuki, A., & Horne, R. N. (2017). Potential Utilizations of 3D Printed Fracture Network Model. In *Proceedings of the 42nd Workshop on Geothermal Reservoir Engineering* (pp. 1–7). Stanford, CA.
- Szwedzicki, T. (2007). Technical Note: A Hypothesis on Modes of Failure of Rock Samples Tested in Uniaxial Compression. *Rock Mechanics and Rock Engineering*,

40(1), 97–104. <https://doi.org/10.1007/s00603-006-0096-5>

Tang, C., & Hudson, J. A. (2011). *Rock Failure Mechanisms Explained and Illustrated* (First Edit). Boca Raton, FL: CRC Press.

Terzaghi, K. (1964). Theoretical Soil Mechanics. *Géotechnique*, 14(1), 1–13. <https://doi.org/10.1680/geot.1964.14.1.1>

Tymrak, B. M., Kreiger, M., & Pearce, J. M. (2014). Mechanical properties of components fabricated with open-source 3-D printers under realistic environmental conditions. *Materials and Design*, 58, 242–246. <https://doi.org/10.1016/j.matdes.2014.02.038>

Vaezi, M., & Chua, C. K. (2011). Effects of layer thickness and binder saturation level parameters on 3D printing process. *International Journal of Advanced Manufacturing Technology*, 53(1–4), 275–284. <https://doi.org/10.1007/s00170-010-2821-1>

Vlasea, M., Pilliar, R., & Toyserkani, E. (2015). Control of structural and mechanical properties in bioceramic bone substitutes via additive manufacturing layer stacking orientation. *Additive Manufacturing*, 6, 30–38. <https://doi.org/http://dx.doi.org/10.1016/j.addma.2015.03.001>

Wang, Z., Jury, W. a, Tuli, A., & Kim, D.-J. (2004). Unstable Flow during Redistribution: Controlling Factors and Practical Implications. *Vadose Zone Journal*, 3(2), 549–559. <https://doi.org/10.2113/3.2.549>

Yale, D. P., Nieto, J. A., & Austin, S. P. (1995). The effect of Cementation on the static and dynamic mechanical properties of the Rotliegendes sandstone. In *Proceedings of the 35th Symposium on Rock Mechanics (USRMS), Reno, Nevada* (pp. 169–175). Reno, Nevada: ARMA 95-0169.

Yan, P., He, Q., Lu, W., He, Y., Zhou, W., & Chen, M. (2017). Coring Damage Extent of Rock Cores Retrieved from High In-situ Stress Condition : A Case Study. *KSCE Journal of Civil Engineering*, 0(0), 1–12. <https://doi.org/10.1007/s12205-017-1660-0>

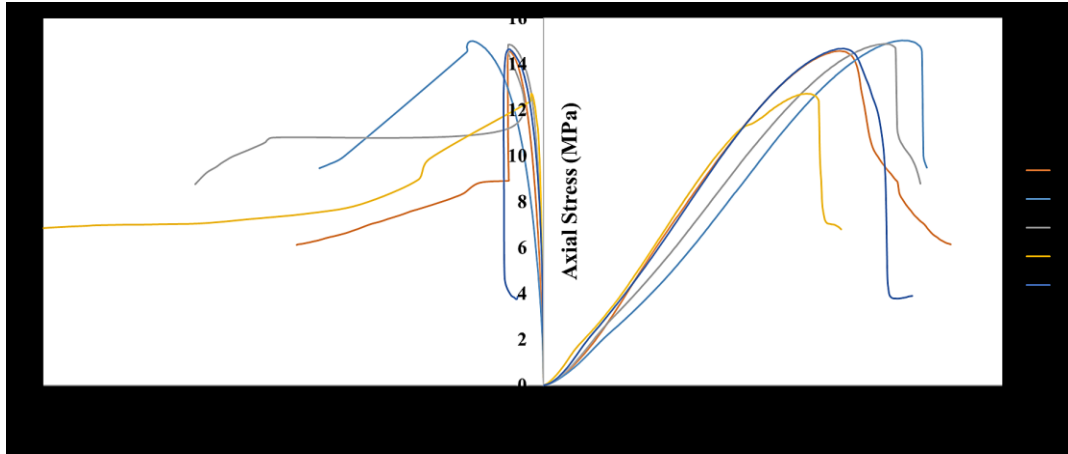
Yang, S. Q., Jing, H. W., Wang, S. Y. (2012). Experimental Investigation on the Strength, Deformability, Failure Behavior and Acoustic Emission Locations of Red Sandstone

- Under Triaxial Compression. *Rock Mechanics and Rock Engineering*, 45, 583–606.  
<https://doi.org/10.1007/s00603-011-0208-8>
- Zhang, Y., Shao, J. F., Xu, W. Y., Zhao, H. B., & Wang, W. (2015). Experimental and Numerical Investigations on Strength and Deformation Behavior of Cataclastic Sandstone. *Rock Mechanics and Rock Engineering*, 48(3), 1083–1096.  
<https://doi.org/10.1007/s00603-014-0623-8>
- Zhou, Y., Tang, Y., Hoff, T., Garon, M., & Zhao, F. Y. (2015). The Verification of the Mechanical Properties of Binder Jetting Manufactured Parts by Instrumented Indentation Testing. *Procedia Manufacturing*, 1, 327–342.  
<https://doi.org/10.1016/j.promfg.2015.09.038>
- Zhou, Z., Buchanan, F., Mitchell, C., & Dunne, N. (2014). Effects of heat treatment on the mechanical and degradation properties of 3D-printed calcium-sulphate-based scaffolds. *Materials Science and Engineering: C*, 38(0), 1–10.  
<https://doi.org/http://dx.doi.org/10.1016/j.msec.2014.01.027>
- Zimmerman, R. W. (1992). *Compressibility of sandstones*. (G. V. Chilingarian, Ed.), *Developments in Petroleum Science*, 29. [https://doi.org/10.1016/0920-4105\(92\)90053-4](https://doi.org/10.1016/0920-4105(92)90053-4)

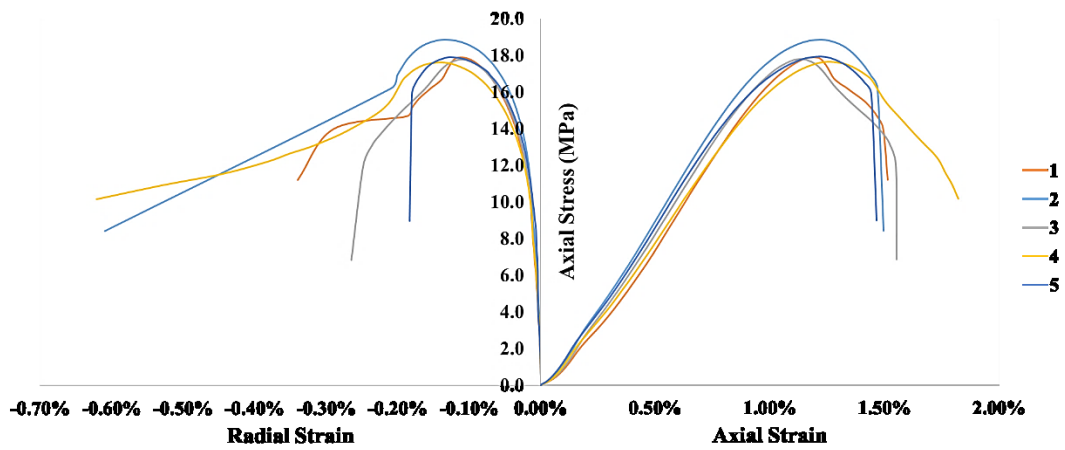
# Appendix A: Uniaxial Compression Tests Data

## Summary of stress-strain behavior and failure modes for Each Cluster of Specimens

### 10%-Binder Saturation- 0° Layer Orientation- 250 μm Layer Thickness

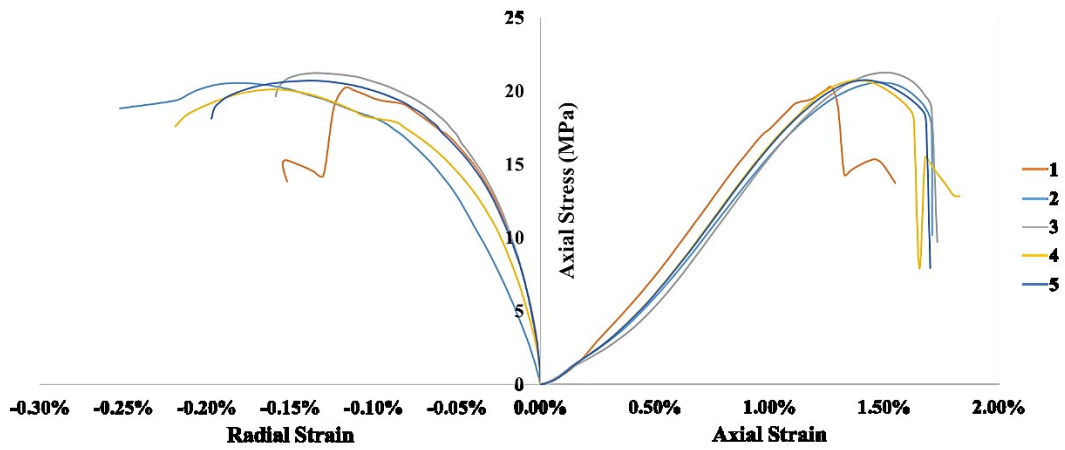


### 15%-Binder Saturation- 0° Layer Orientation- 250 μm Layer Thickness

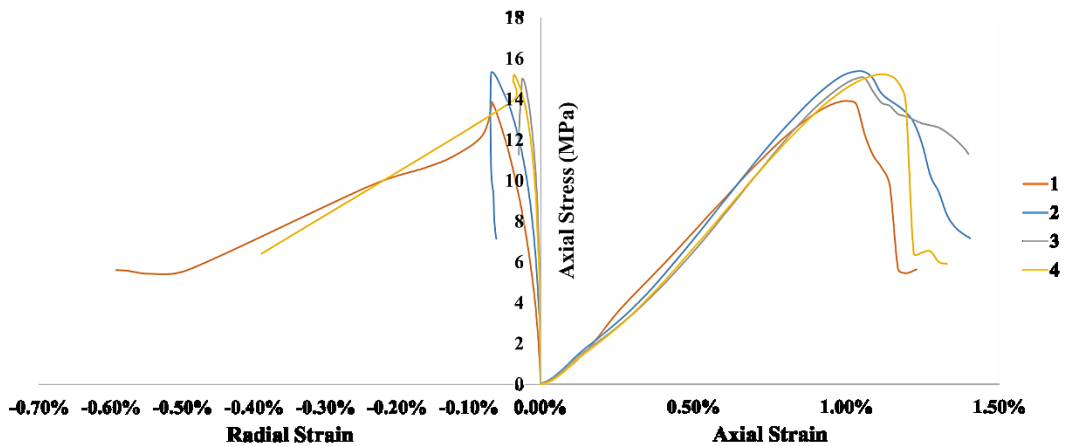




20%-Binder Saturation- 0° Layer Orientation- 250 μm Layer Thickness

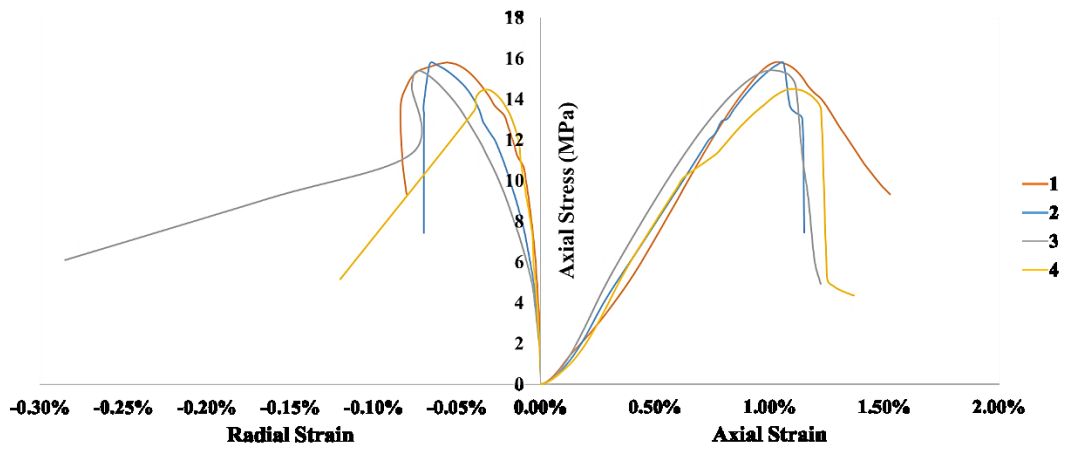


10%-Binder Saturation- 25° Layer Orientation- 250 μm Layer Thickness

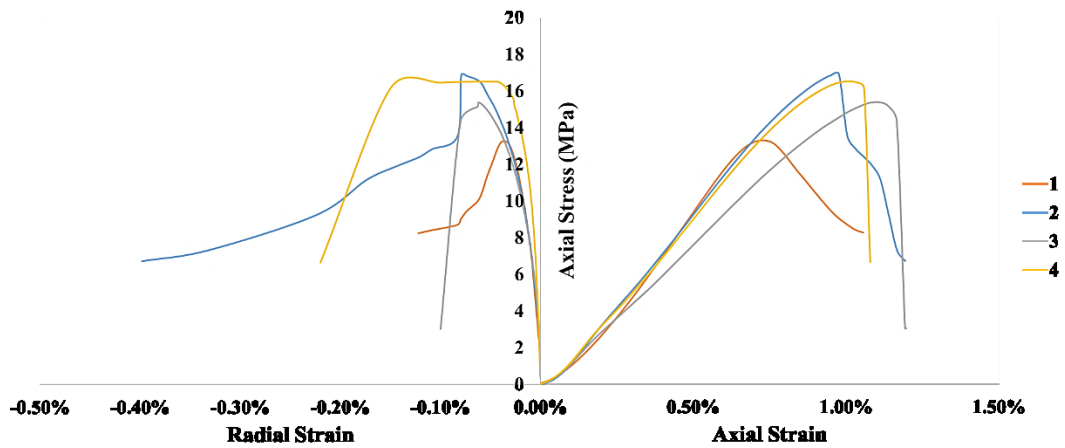




10%-Binder Saturation- 45° Layer Orientation- 250 μm Layer Thickness

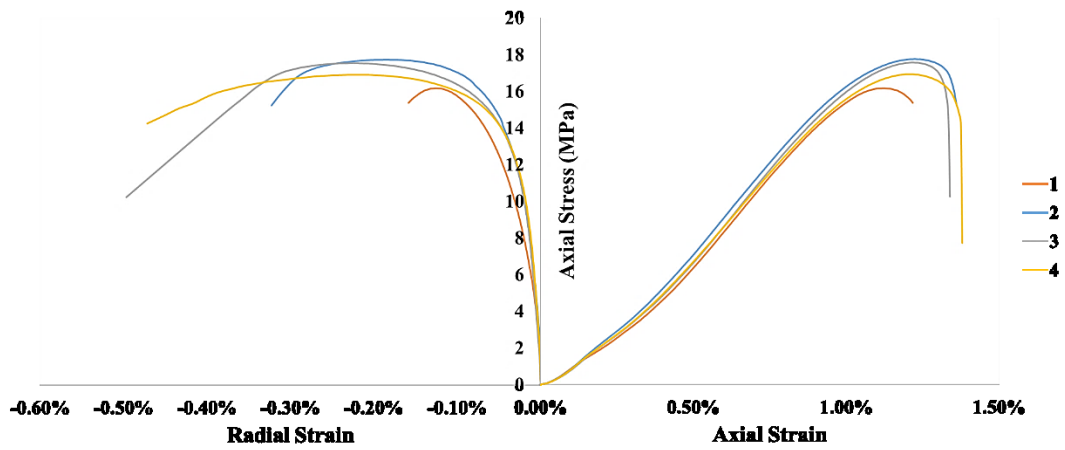


10%-Binder Saturation- 65° Layer Orientation- 250 μm Layer Thickness

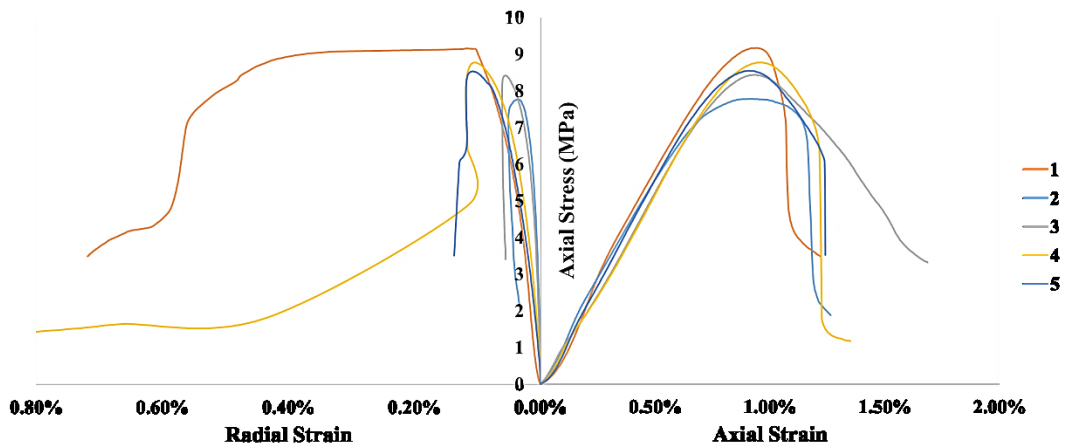




10%-Binder Saturation- 90° Layer Orientation- 250 μm Layer Thickness



10%-Binder Saturation- 0° Layer Orientation- 400 μm Layer Thickness





## Summary Table of Mechanical Properties for each cluster of 3D Printed Sandstone Analogues

Sample ID	Mean Diameter [mm]	Mean Length [mm]	Mean Diameter [mm]	Mean Length [mm]	Orientation Angle [Degrees]	Layer Thickness [µm]	Shear Rate [mm/min]	Peak Strength [MPa]	Axial Deformation at Peak [%]	Radial Deformation at Peak [%]	Peak Young's Modulus [GPa]	Poisson's Ratio	Average Peak Strength [MPa]	Average Axial Deformation at Peak [%]	Average Radial Deformation at Peak [%]	Average Peak Young's Modulus [GPa]	Average Poisson's Ratio
0Degrees 10% 1	38.64	76.69	38.50	76.70	0.00	250.00	0.25	14.57	0.97%	0.07%	2.100	0.04	14.78	1.06%	0.09%	1.700	0.19
0Degrees 10% 2	38.48	76.75			0.00	250.00	0.25	15.01	1.19%	0.15%	1.430	0.05					
0Degrees 10% 3	38.54	76.69			0.00	250.00	0.25	14.87	1.11%	0.07%	1.500	0.01					
0Degrees 10% 4	38.35	76.65			0.00	250.00	0.25	14.67	0.98%	0.07%	1.770	0.02					
65Degrees 10% 1	38.30	76.71	38.29	76.76	65.00	250.00	0.25	13.90	1.00%	0.07%	1.620	0.05	14.873	1.050%	0.048%	1.585	0.22
65Degrees 10% 2	38.12	76.89			65.00	250.00	0.25	15.35	1.03%	0.06%	1.600	0.02					
65Degrees 10% 3	38.42	76.71			65.00	250.00	0.25	15.02	1.06%	0.02%	1.500	0.02					
65Degrees 10% 4	38.30	76.71			65.00	250.00	0.25	15.22	1.11%	0.04%	1.620	0.05					
45Degrees 10% 1	38.34	76.82	38.30	76.73	45.00	250.00	0.25	15.81	1.03%	0.06%	1.650	0.01	15.365	1.045%	0.055%	1.928	0.17
45Degrees 10% 2	38.34	76.70			45.00	250.00	0.25	15.74	1.06%	0.06%	1.770	0.03					
45Degrees 10% 3	38.30	76.71			45.00	250.00	0.25	15.41	1.00%	0.07%	2.140	0.05					
45Degrees 10% 4	38.23	76.70			45.00	250.00	0.25	14.50	1.09%	0.03%	2.150	0.02					
25Degrees 10% 1	38.62	76.93	38.55	76.86	25.00	250.00	0.25	15.29	0.73%	0.03%	2.060	0.02	16.030	0.955%	0.053%	1.903	0.16
25Degrees 10% 2	38.60	76.90			25.00	250.00	0.25	16.91	0.98%	0.07%	2.020	0.04					
25Degrees 10% 3	38.34	76.82			25.00	250.00	0.25	15.39	1.11%	0.07%	1.550	0.02					
25Degrees 10% 4	38.64	76.79			25.00	250.00	0.25	16.53	1.00%	0.04%	1.980	0.02					
90Degrees 10% 1	38.87	76.98	38.78	76.93	90.00	250.00	0.25	16.18	1.12%	0.12%	1.610	0.05	17.098	1.188%	0.180%	1.678	0.24
90Degrees 10% 2	38.79	76.91			90.00	250.00	0.25	17.75	1.22%	0.18%	1.760	0.04					
90Degrees 10% 3	38.67	76.86			90.00	250.00	0.25	17.55	1.21%	0.22%	1.670	0.03					
90Degrees 10% 4	38.80	76.95			90.00	250.00	0.25	16.91	1.20%	0.20%	1.670	0.03					
0Degrees 15% 1	38.43	76.68	38.52	76.69	0.00	250.00	0.25	17.90	1.19%	0.11%	1.720	0.03	18.022	1.204%	0.116%	1.784	0.16
0Degrees 15% 2	38.43	76.68			0.00	250.00	0.25	18.87	1.22%	0.12%	1.901	0.02					
0Degrees 15% 3	38.53	76.74			0.00	250.00	0.25	17.79	1.14%	0.10%	1.810	0.03					
0Degrees 15% 4	38.50	76.56			0.00	250.00	0.25	17.64	1.25%	0.13%	1.690	0.03					
0Degrees 15% 5	38.70	76.80			0.00	250.00	0.25	17.91	1.22%	0.12%	1.800	0.02					
0Degrees 20% 1	38.60	77.24	38.63	77.14	0.00	250.00	0.25	20.76	1.27%	0.12%	1.840	0.04	20.780	1.498%	0.146%	1.724	0.25
0Degrees 20% 2	38.84	77.01			0.00	250.00	0.25	20.59	1.49%	0.18%	1.720	0.06					
0Degrees 20% 3	38.22	76.90			0.00	250.00	0.25	21.25	1.52%	0.13%	1.840	0.03					
0Degrees 20% 4	38.75	77.27			0.00	250.00	0.25	20.54	1.81%	0.20%	1.420	0.04					
0Degrees 20% 5	38.75	77.27			0.00	250.00	0.25	20.76	1.40%	0.10%	1.800	0.03					
0Degrees 10% 1	38.49	76.80	38.49	76.57	0.00	400.00	0.25	9.18	0.94%	0.04%	1.480	0.02	8.546	0.937%	0.072%	1.232	0.25
0Degrees 10% 2	38.48	76.50			0.00	400.00	0.25	7.78	0.92%	0.04%	1.500	0.02					
0Degrees 10% 3	38.50	76.51			0.00	400.00	0.25	8.44	0.94%	0.06%	1.030	0.02					
0Degrees 10% 4	38.51	76.53			0.00	400.00	0.25	8.78	0.97%	0.11%	1.011	0.06					
0Degrees 10% 5	38.46	76.51			0.00	400.00	0.25	8.55	0.91%	0.11%	1.140	0.08					
MEAN VALUES	38.51	76.80	Range of Calculated values for Strength, Elastic Properties and Strains at Failure Conditions				MAXIMUM	21.250	1.81%	0.22%	2.150	0.080	20.780	1.50%	0.18%	1.928	0.251
DEVIATION FROM THEORETICAL VALUE	1.08%	1.56%					MINIMUM	7.779	0.73%	0.02%	1.011	0.010	8.546	0.94%	0.05%	1.232	0.157